



HAL
open science

Numérique simulation of mesoscale processes in the Ligurian Sea

Elisa Casella

► **To cite this version:**

Elisa Casella. Numérique simulation of mesoscale processes in the Ligurian Sea. Ocean, Atmosphere. Université du Sud Toulon Var, 2009. English. NNT: . tel-00533713

HAL Id: tel-00533713

<https://theses.hal.science/tel-00533713>

Submitted on 8 Nov 2010

HAL is a multi-disciplinary open access archive for the deposit and dissemination of scientific research documents, whether they are published or not. The documents may come from teaching and research institutions in France or abroad, or from public or private research centers.

L'archive ouverte pluridisciplinaire **HAL**, est destinée au dépôt et à la diffusion de documents scientifiques de niveau recherche, publiés ou non, émanant des établissements d'enseignement et de recherche français ou étrangers, des laboratoires publics ou privés.



Thesis in co-direction

UNIVERSITA' DEGLI STUDI DELLA BASILICATA

Dottorato in Metodi e Tecnologie per il Monitoraggio Ambientale

UNIVERSITE du SUD TOULON-VAR

Doctorat in Sciences de l'Univers

....."23B4H22; "

Numerical simulation of mesoscale processes in the Ligurian Sea.

By Elisa Casella

Committee:

Luca Ferraris	director
Anne Molcard	director
Antonello Provenzale	director
Sabrina Speich	reviewer
Bruno Zakardjian	
Enrico Zambianchi	reviewer
Marco Zavatarelli	

TABLE OF CONTENTS

Résumé en français	IV
Sintesi in italiano	VI
Abstract	VIII
1. INTRODUCTION	1
2. SCIENTIFIC BACKGROUND AND OBJECTIVES	3
2.1 The study area	3
2.2 Description of the Mediterranean Sea	5
2.2.1 <i>Structure of the water masses</i>	6
2.2.2 <i>Driving forces of the circulation</i>	7
2.2.3 <i>Horizontal circulation of water masses</i>	8
2.2.4 <i>Deep and intermediate water formation</i>	11
2.2.5 <i>Thermohaline axes</i>	12
2.3 Hydrodynamical features of the Ligurian Sea	14
2.4 Main feature of seasonal dynamic of primary production in the Ligurian Sea	17
3. NUMERICAL MODELS	21
3.1 Ocean models	21
3.1.1 <i>Types, advantages and limitations of ocean models</i>	21
3.2 ROMS, Regional Ocean Modeling System	24
3.2.1 <i>Model description</i>	25
3.2.2 <i>Model formulation</i>	28
3.2.2.1 <i>Equations of motion</i>	28
3.2.2.2 <i>Vertical Terrain-Following Coordinates</i>	31
3.2.2.3 <i>Horizontal Curvilinear Coordinates</i>	33
3.2.3 <i>Parameterization of sub-grid processes</i>	35
3.2.3.1 <i>Non-local K profile</i>	

<i>parameterization (KPP)</i>	35
3.2.4 <i>Numerical solution technique</i>	37
3.2.4.1 <i>Horizontal discretization</i>	37
3.2.4.2 <i>Vertical discretization</i>	38
3.2.4.3 <i>Time stepping scheme</i>	39
3.3 <i>Biogeochemical Model</i>	40
3.3.1 <i>State of the art of plankton models</i>	40
3.3.1.1 <i>NPZD model</i>	42
3.3.2 <i>Biological dynamics in NPZD model</i>	44
3.3.2.1 <i>Phytoplankton growth rate</i>	44
3.3.2.2 <i>Grazing, zooplankton growth and excretion</i>	45
3.3.2.3 <i>Regeneration and the nutrient and detritus equations</i>	46
3.3.2.4 <i>Sedimentation of phytoplankton and detritus</i>	47
3.3.2.5 <i>Phytoplankton, zooplankton, nutrient and detritus full equations</i>	47
3.4 <i>Improvement of the biogeochemistry and the regional biogeochemistry of the model</i>	48
3.5 <i>NPZD model coupled with ROMS model</i>	53
4. RESULTS	54
4.1 <i>Description of the main simulations</i>	54
4.2 <i>Model configuration</i>	55
4.3 <i>Initial and boundary conditions</i>	57
4.4 <i>Comparison between climatological and interannual simulations</i>	60
4.5 <i>Wind effect on mesoscale eddies structures</i>	68
4.6 <i>Downscaling from 3 km to 300 m</i>	76
4.7 <i>Biological production</i>	85
4.8 <i>Primary production and impact of</i>	

mesoscale structures on biological production	94
4.9 Model evaluation	106
5. CONCLUSION AND PERSPECTIVES	119
Bibliography	123
ANNEX 1	135
ANNEX 2	139
Acknowledgments	143
<i>Curriculum vitae</i>	144

Résumé en français

Le but de ce travail est l'étude de processus à mésoéchelle de la mer Ligure. L'étude concerne les tourbillons et leur effet sur les variables biogéochimiques liées au plancton.

Le modèle implémenté pour les simulations est ROMS, Regional Ocean Modeling System (Shchepetkin and McWilliams, 2005). La simulation à haute résolution du courant Ligure-Provençal-Catalan dans la Mer Ligure a révélé la présence d'instabilités qui induit la formation de structures tourbillonnaires. Ces tourbillons sont particulièrement intenses lorsque le forçage du vent provient d'un modèle météorologique à haute résolution spatiale et temporelle. Au contraire, l'utilisation de vents climatologiques à basse résolution comme forçage, induit des structures à mésoéchelle moins intenses et moins nombreuses. Les simulations forcées avec des vents réels permettent la formation d'intenses tourbillons anticycloniques entre la courant Ligure-Provençal et la côte. Ces tourbillons se déplacent lentement avec le courant. L'augmentation de la résolution permet de faire apparaître de petits structures tourbillonnaires autour du vortex principal. Les tourbillons observés sont associés à des structures de vitesse verticale complexes. La simulation montre d'importantes vitesses verticales positives (upwelling) près de la côte qui peuvent induire la remontée de masses d'eaux riches en nutriments, et des vitesses verticales négatives au centre du tourbillon. Les vitesses verticales augmentent avec la résolution de la simulation et peuvent atteindre des valeurs de l'ordre de la dizaine de mètres par jour. L'augmentation de la résolution permet de résoudre plus en détail la distribution du champ de vitesse et on observe ainsi des structures complexes de vitesses positives et négatives que s'alternent en correspondance d'un tourbillon. Pour ce qui concerne les vitesses horizontales, la résolution n'a pas un effet significatif sur leur intensité et distribution. Cela signifie que le processus est suffisamment bien résolu dans la simulation à plus basse résolution. Les vitesses verticales associées

au tourbillon peuvent avoir un rôle significatif pour la dynamique de l'écosystème marin de la Mer Ligure. Ces structures peuvent apporter en surface des masses d'eaux riches en nutriments qui peuvent mettre en route la chaîne trophique liée à la production primaire. Tous les vivants sont liés directement ou indirectement à cette production. Pour étudier l'impact des structures à mésoéchelle sur les variables biologiques nous avons appliqué un module biogéochimique couplé au modèle hydrodynamique. Les résultats mettent en évidence la complexité du comportement des variables biogéochimiques en présence des structures dynamiques, ainsi que leur variabilité en fonction du type de tourbillons (cyclonique ou anticyclonique). Les tourbillons cycloniques représentent essentiellement des zones de croissance de biomasse. Les tourbillons anticycloniques représentent aussi des zones d'accumulation de biomasse mais aussi des zones de croissance de biomasse due à la remontée d'eaux riches en nutriment au bord du tourbillon.

Les résultats du travail de thèse et décrits dans ce document, montrent l'importance des processus à la mésoéchelle, l'impact de tourbillons sur la production biologique et la nécessité d'adopter une résolution spatio-temporelle suffisamment haute pour le modèle océanique et pour les forçages atmosphériques.

Sintesi in italiano

L'obiettivo di questo lavoro è uno studio dei processi alla mesoscala del Mar Ligure con particolare attenzione alle strutture dei vortici e al loro impatto su variabili biogeochimiche legate al plankton. Il modello utilizzato per le simulazioni è ROMS, Regional Ocean Modeling System (Shchepetkin and McWilliams, 2005). La simulazione ad alta risoluzione della corrente Ligure-Provenzale-Catalana nel Mar Ligure, presentata in questo lavoro, ha rivelato la presenza di instabilità che induce la formazione di vortici alla mesoscala. I vortici risultano particolarmente intensi quando vengono utilizzati, come forzanti, dei venti "realistici", provenienti da modelli meteorologici con alta risoluzione spaziale e temporale. Al contrario, l'uso di venti climatologici a bassa risoluzione come forzanti, inducono delle strutture alla mesoscala meno intense e meno numerose. Le simulazioni forzate con venti "realistici" inducono la formazione di intensi vortici anticiclonici tra la corrente Ligure-Provenzale e la costa. Questi vortici si muovono lentamente insieme alla corrente. L'aumento della risoluzione permette di vedere piccoli vortici intorno al vortice principale appena accennati nella simulazione a più bassa risoluzione. I vortici analizzati risultano essere associati a complessi pattern di velocità verticale. La simulazione mostra intense velocità verticali positive (upwelling) presso la costa che possono indurre la risalita di masse d'acqua ricche di nutrienti e la presenza di velocità verticali negative al centro del vortice. Le velocità verticali positive possono raggiungere alti valori dell'ordine delle decine di metri al giorno. Aumentando la risoluzione della simulazione, queste velocità verticali aumentano. L'aumento della risoluzione permette di risolvere più in dettaglio la distribuzione dei campi di velocità che, a loro volta, permettono di osservare dei pattern complessi di velocità positive e negative che si alternano in corrispondenza del vortice. Per quanto riguarda le velocità orizzontali, l'aumento della risoluzione non ha un effetto

significativo sulla loro intensità e distribuzione. Questo significa che il processo è sufficientemente risolto già dal modello a più bassa risoluzione.

Le velocità verticali associate al vortice possono avere un ruolo significativo per la dinamica dell'ecosistema marino nel Mar Ligure. Queste strutture possono apportare in superficie masse d'acqua ricche di nutrienti che danno l'avvio alla catena trofica legata alla produttività primaria. Tutti gli esseri viventi sono legati direttamente o indirettamente a tale produttività. Per studiare l'impatto delle strutture alla mesoscala sulle variabili biologiche è stato utilizzato un modello biogeochimico accoppiato al modello idrodinamico. I risultati forniti dal modello biogeochimico evidenziano che il comportamento delle variabili biogeochimiche in presenza delle strutture, è complesso e dipende dal particolare tipo di struttura. Entrambe le tipologie di vortici, ciclonici e anticiclonici, hanno un impatto sul comportamento delle variabili biogeochimiche. I vortici ciclonici sono risultati essenzialmente delle zone di crescita di biomassa. I vortici anticiclonici sono risultati principalmente aree di accumulo di biomassa ma anche zone di crescita di biomassa probabilmente dovuta alla risalita di acqua ricca di nutrienti ai bordi del vortice stesso.

I risultati riportati in questo lavoro indicano l'importanza dei processi alla mesoscala, l'impatto di questi sulla produzione biologica e la necessità di adottare risoluzioni spaziali e temporali alte sia per le simulazioni sia per i forzanti.

Abstract

In this work we study numerically the currents dynamics of the Ligurian Sea (NW Mediterranean Sea) with a particular attention on mesoscale structures. To this end, we use the Regional Ocean Modeling System (ROMS) for a domain covering the whole Ligurian Sea, with embedded child grids covering the northwestern part of Ligurian Sea at resolution firstly 1 km, successively 300 m. The model is forced with climatological and output of operative model dataset, depending on the simulation. The simulations forced with the output of operative model show the formation of intense anticyclonic eddy structures in the coastal area, generated by the variable winds and by the interaction of transient currents with bottom and coastal topography (in the NW part of the Ligurian Sea). The eddies are characterized by a complex pattern of intense vertical velocities and induce strong, long-lasting coastal upwelling events. For this reason, anticyclonic vortices in the coastal area can generate bursts of nutrient input in the euphotic layer and contribute to the fertilization of the Ligurian Sea, with potentially important effects on the dynamics of phyto- and zooplankton. To detect the impact of mesoscale structures on biological production, a biogeochemical model coupled with the physical circulation model has been used. The results provided by the biogeochemical model evidence that the behaviour of biogeochemical variables in presence of structures is complex and it depends on the particular type of structure. Both cyclonic and anticyclonic eddies have an impact on the behaviour of biogeochemical variables.

1 Introduction

Ocean science is, by its nature, science of systems that integrates dynamics in various disciplines: physics, chemistry, biology and geology. Numerical modelling represents an essential and efficient tool to provide an insight into the interactions between different disciplines and integrate dynamics at a system level (Tian, 2006).

The work of the thesis take place in this context and try to provide a study, with numerical models, of the interaction between physics, chemistry and biology. The main aims of the thesis are a study of the Ligurian Sea hydrodynamic and mesoscale processes and the evolution of biogeochemical variables linked to the low trophic levels with a particular attention to the primary production term. Focus is given especially to the link between physical processes and biological one. To achieve this aims a numerical model has been applied for a regional simulation of the Ligurian Sea coupled with a simple biogeochemical model. The numerical model system helps in understanding, at a low trophic level, the ecosystem functioning and evolution and the influence of environmental physical processes on intensity and distribution of biological production. Trophic dynamics are key energy links from primary production to high trophic levels. Primary production is the production of organic compounds from atmospheric or aquatic carbon dioxide, principally through the process of photosynthesis.

All life on earth (and in water) is directly or indirectly reliant on primary production. The organisms responsible for primary production are known as primary producers or autotrophs, and form the base of the trophic chain. A study on the influence of physical processes on biological dynamic can help in understanding the base of the complex system of the trophic chains. However, the intrinsic complexity in trophic dynamics and diversity in ecosystem function limit the ability of ecological and biological models.

CHAPTER 1: INTRODUCTION

Numerical models have limitation in simulating the marine ecosystems and its environment due to the complexity of the system and the availability and quality of dataset used to constrain the model.

Due to the interdisciplinary character of this work, which range from oceanography, biology at low trophic level to numerical model, I carried out various activities during my thesis. Besides the results presented in this document, many other tasks and technical developments have been necessary to the achievement of this thesis, but not included in the present document. For example, the pre-processing phase of model input data, which come from different dataset on different form, is fundamental and need a lot of time but it is not described in the thesis due to its technical nature. Also the collect and the analysis of different dataset inappropriate, are omitted.

This thesis is collocated in the framework of “co-tutelle de these” between the University of Basilicata and the University of Toulon which allowed me to develop part of the thesis in France, to work in different research centre and to learn from different work environment.

The thesis is organized as follow:

In the first chapter the state of the art of hydrodynamical and biogeochemical knowledge and process-studies with numerical models applied to the study region have been described. The second chapter summarize the main characteristics of the models used while the following chapter describes the results achieved applying the model on the study region. The chapter shows the results of several simulations with different configurations and a comparison between the output of the simulation and measured data. The conclusions and perspectives are summarized in the last chapter.

2 Scientific background and objectives

2.1 The study area

The Ligurian Sea is an interesting area as it has been recognized as crucial in comprehending the seas dynamics, since there are a numbers of oceanic processes which develop in this particular area. It is one of the most dynamically active and productive area of the Mediterranean Sea. A permanent cyclonic circulation, with a marked interannual variability, dominates the area. During winter, processes of dense water formation can occur (section 2.2). The productivity of the Ligurian Sea allow the presence of a number of great pelagic like cetaceans which are present in the area. The Ligurian Sea is located into the International Sanctuary for the Preservation of Mediterranean Marine Mammals. For this main reasons we decided to do a process-oriented study in the Ligurian Sea region. To study the physical and biological processes, a numerical model has been applied for a regional simulation of the Ligurian Sea coupled with a simple biogeochemical model.

In the last years, the Ligurian Sea as part of the Mediterranean Sea has been subject to several numerical modeling works focused mainly on the study of the circulation of the Mediterranean Sea and mechanisms that generate it at different temporal and spatial scales (Beckers, 1991; Tziperman and Malanotte-Rizzoli, 1991; Pinardi and Navarra, 1993; Haines and Wu, 1995; Roussenov et al., 1995; Zavatarelli and Mellor, 1995; Herbaut et al., 1996, 1997; Brankart and Brasseur, 1998; Pinardi and Masetti, 2000; Beckers et al., 2002; Demirov and Pinardi, 2002; Molcard et al., 2002; Echevin et al., 2003; Pinardi et al., 2003; Barth et al., 2005; Fernández et al., 2005; Ahumada and Cruzado, 2007; and others). The spatial resolution of oceanographic models plays an important role in representing and simulating ocean processes (Barth et al., 2005). Nevertheless, the variety of

models, configurations, parameterizations, resolutions, forcing, etc., suggest that no single model is going to be the best one for all applications. In this work of thesis, a numerical modeling system based on ROMS model (section 3.2) has been implemented in the Ligurian Sea in order to investigate physical and biological processes of the study area. ROMS has been applied, with good results, for the regional simulation of variety of different regions of the world oceans, in some cases coupled with a biogeochemical model (Gruber et al., 2006; Koné et al., 2005; Penven et al. 2005; Di Lorenzo et al., 2003; Marchesiello et al., 2003; Blanke et al., 2002; MacCready et al., 2002; Penven et al., 2001; Haidvogel et al., 2000 and others). As the Ligurian Sea has an important biological productivity which maintains also a rich marine mammals system, we decided to test a simple biogeochemical model (section 3.3) coupled with the physical one (section 3.4) in order to investigate biological processes with particular attention to the primary production of the study area.

The coupling between physical and biogeochemical three-dimensional model has experienced a relatively recent development (section 3.3.1). The pioneers on coupling three-dimensional physical-biogeochemical models are Fasham et al. (1993) and Sarmiento et al. (1993). They coupled a nitrogen based, single phytoplankton functional group, single zooplankton, bacteria, and detritus model developed by Fasham et al. (1990) to a 3-D ocean general circulation model (OGCM) of the North Atlantic. Afterwards, several study have been applied in different regions of the world oceans (Di Lorenzo et al., 2003; Koné et al., 2005; Le Fouest et al., 2005; Gruber et al., 2006; and others). In Mediterranean Sea, studies using different one-dimensional complex biogeochemical model (Zakardjian and Prieur, 1998; Levy et al., 1998; Allen et al., 2002; Vichi et al., 2003; Raick et al., 2005; and other), have been done in Adriatic Sea, Cretan Sea and Ligurian Sea.

In this work of thesis a three-dimensional simple biogeochemical model (section 3.3) coupled to the physical model has been applied to the Ligurian

Sea to study physical and biological processes. To this end the ROMS model have been implemented in the study region with different configurations (section 4.1). After the analysis of the output of the simulations (sections 4.4 and 4.5), a study on the impact of variable wind on eddies structure have been done (section 4.6) which remark the influence of wind stress on mesoscale structures. In the last part of the thesis a simple biogeochemical model have been applied to study the influence of mesoscale structures on biological production (section 4.8) with remark on the seasonal evolution of the simulated biogeochemical variables and the primary production of the study area (section 4.7).

In this chapter we focus the attention on the circulation of the study area and on the main features of seasonal dynamic of primary production in the Ligurian Sea. The Ligurian Sea is located in the North West part of the Mediterranean Sea. Its circulation is linked to the general circulation of the Mediterranean Sea.

2.2 Description of the Mediterranean Sea

The circulation of the atmosphere, drove by the different heating on the planet, drives the ocean circulation. Energy is transferred from winds to the upper layer of the ocean through frictional coupling between the ocean and the atmosphere at the sea-surface. The sun also drives directly ocean circulation by causing variations in the temperature and salinity of seawater which in turn control its density. These are the main processes which force the motion in all the ocean of the planet.

The Mediterranean Sea is a semi-closed sea of more than 2.5 millions of km² (0.7% of the world ocean) located on the mean latitude in the north hemisphere (Béthoux et al., 1999). The main inputs of fresh water are rainfalls and the three major rivers, the Rhone in the northwestern Mediterranean Sea, the Nile in the southern Mediterranean and the Po' into

the Adriatic Sea. The Mediterranean Sea communicates with the Atlantic Ocean through the shallow Gibraltar Strait, with the Black Sea through the Dardanelles and the Bosphorus and with the Red Sea through the artificial Suez Canal. All of these communications have an influence, more or less important, on the basin. Its deepest point is at a depth of about 5000 m, inside the Ionian Sea. The Mediterranean Sea is composed of two wide basins, the occidental one and the oriental one, communicating through the shallow Sicilian Strait. Themselves are divided in more restricted sub-basins: the Adriatic Sea (1), the Aegean Sea (2), the Levantine Sea (3), the Ionian Sea (4), the Tyrrhenian Sea (5), the Ligurian Sea (6), the Balearic Sea (7) and the Alboran Sea (8) with numerous large and small islands spread all over (figure 2.1). The mean depth of the Mediterranean Sea is 1500 m, with a narrow continental shelf, a steep continental slope and extensive deep plains below 3000 m.

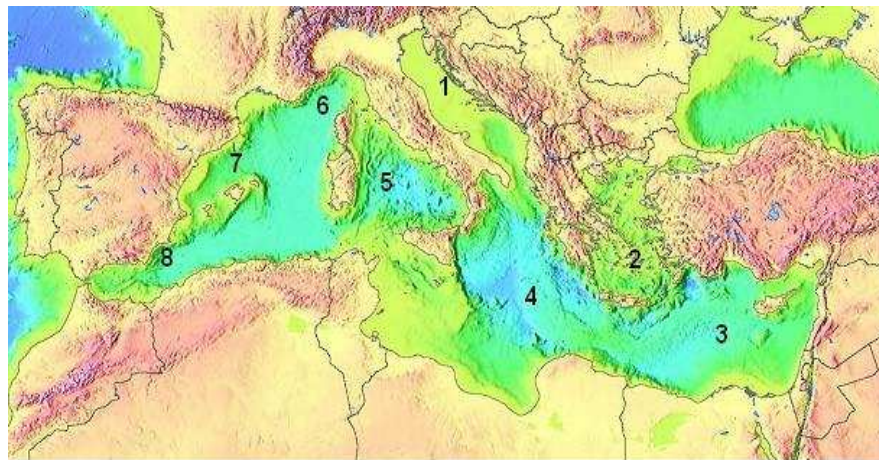


Fig. 2.1 The Mediterranean basin. Adriatic Sea (1), Aegean Sea (2), Levantine Sea (3), Ionian Sea (4), Tyrrhenian Sea (5), Ligurian Sea (6), Balearic Sea (7) and Alboran Sea (8).

2.2.1 Structure of the water masses

Water masses are identified according to their temperature, salinity and pressure properties; those three parameters then define their density. The characteristics of water masses are created by surface thermodynamic

processes in specific location. This process generates different density gradient in the water masses which drives the thermohaline circulation. The Mediterranean Sea is constituted by three main layers: the superficial waters named Modified Atlantic Waters (MAW), the Levantine Intermediate Waters (LIW) and the Deep Waters (DW) (Millot, 1999). The MAW is Atlantic water flowing into the Mediterranean Sea through Gibraltar Strait and travelling in both of the two basins. During this travelling, they are progressively transformed through the interaction with the atmosphere and the mixing up with Mediterranean waters. Under this superficial stratum, the LIW flows also into the entire basin. Its name is a reference to its origin in the Levantine sub-basin; it is characterized by a major salinity (more than 38 psu). Two masses of DW are on the bottom of both occidental and oriental basins, the Western Deep Water (WDW) and the Eastern Deep Water (EWD). They don't mix with each other because they are confined by the shallow Sicilian Sill. They are characterized by dense waters with high salinity and low temperature. The Mediterranean Sea also has other local water masses. They are formed under different conditions and also play an important role on the Mediterranean superficial and deep circulations.

2.2.2 Driving forces of the circulation

Multiple forces impose the circulation of water masses and the anti-estuarine circulation (dense water flows out near the bottom and less dense water circulates inward at the surface) towards both the Gibraltar and the Sicilian Straits (Béthoux et al., 1999). First, wind stress causes superficial mesoscale structures in both basins (oriental and occidental) and their variability can influence the total basin circulation. Second, water input at Gibraltar Strait balances the Mediterranean negative water budget. Indeed, there is a unevenness between evaporation and input by rivers and

precipitations; deficit that would decrease the sea level by 0.5 to 1 m per year (Béthoux et al., 1999). Thirdly, caloric loss at the atmosphere-ocean interface impose the water input at Gibraltar Strait to reintroduce heat. These heat losses are linked to the important exchanges of the atmosphere-ocean interface during the DW formation, the high variability of the system and the effects of Sahara particles in limiting solar radiations. The most recent estimate of the average heat transport through the Strait of Gibraltar of $5.2 \pm 1.3 \text{ W} \cdot \text{m}^{-2}$ into the Mediterranean Sea, (Krahmann et al., 2000) balance the heat loss.

2.2.3 Horizontal circulation of water masses

The horizontal circulation is composed of large-scale, sub-basin scale, mesoscale and small scale structures such as confined or free currents, jets, vortices, cyclonic and anticyclonic gyres and mesoscale eddies. All these structures interacting with each others have different time longevity and variable spatial scale (Wüst, 1961). The first stratum is constituted by MAW with low density running along the northern African coast, crossing the southern Balearic sea, and forming the Algerian current (Figure 2.2). This current is quite instable and produces local eddies that may form vortex of hundreds of kilometres diameters propagating at a few km per day.

The Algerian current reaching the Tunisian coast splits into two water masses, one running along the Sicilian coast, the other passing into the oriental basin. The occidental branch forms successively two cyclonic structures, one in the Tyrrhenian sea, the other in the Gulf of Lion. The oriental branch forms the Atlantic-Ionian stream which crosses the Ionian sea in its middle and composes three structures: the cyclonic Ionian gyre in the northeast, some mesoscale eddies in the central part and the Tunisian vein running on the shelf edges and near the South shore (Millot and Taupier-Letage, 2005). The Tunisian vein evolves in Libyan vein, quite

unstable forming some eddies and eventually an anticyclonic structure in the Gulf of Syrte. Along the Egyptian coast, it generates the Libyo-Egyptian Current, with similar characteristics to the Algerian one with eddies generated by the Libyan coast up to the Nile delta. Sometimes, a larger vortex is also formed here with a hundreds of kilometres diameter propagating at 3 km per day. On the Turkish coast, the Asia Minor current generates meanders and anticyclonic eddies belonging to the Rhodes gyre.

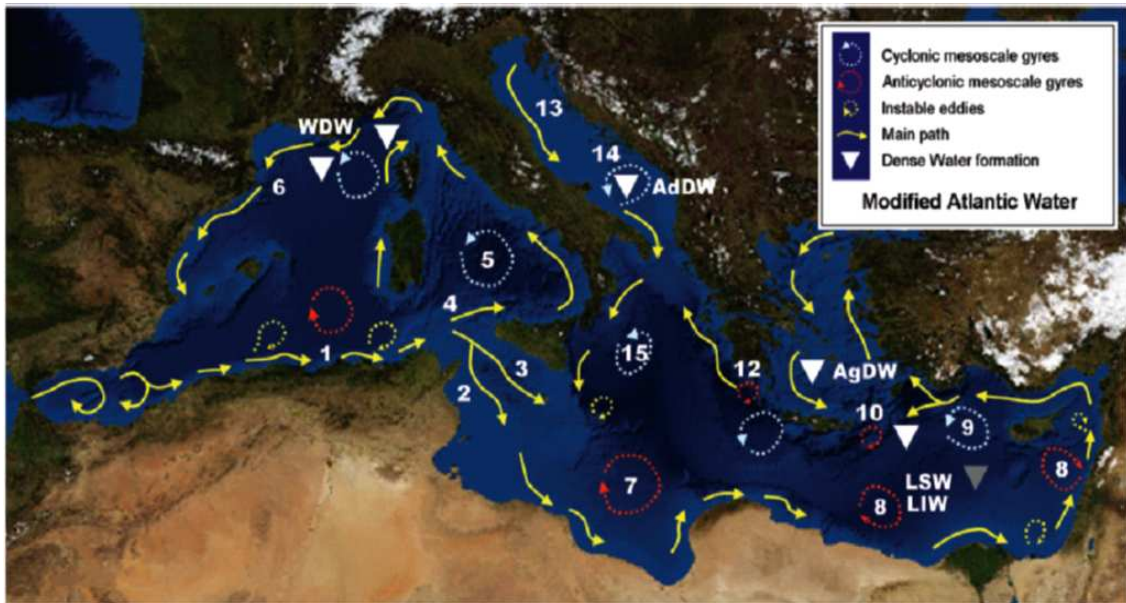


Fig. 2.2 Circulation of the Modified Atlantic Water in the Mediterranean Sea. 1: Algerian current, 2: Tunisian vein of Algerian current, 3: Mid Ionian vein of Algerian current, 4: Tyrrhenian vein of Algerian current, 5: Tyrrhenian cyclonic gyre, 6: Liguro-Provenco-Catalan current, 7: Anticyclonic gyre of the Gulf of Syrte; 8: Shikmona and Mersa-Matruh gyre, 9: Rhode gyre, 10: Ierapetra gyre, 11: Cretan gyre 12: Pelops gyre, 13: Western Adriatic current, 14: Southern Adriatic gyre, 15: Ionian gyre. *Adapted from: (Lascazatos et al., 1999; Millot and Taupier-Letage, 2005; Pinardi and Masetti, 2000).*

The Rhodes Island divides the MAW into different veins, (1) one going northwest ward (2) another going southwest ward, and sometimes gets connects with the Pelops gyre (mainly during the winter). The northwestern vein (1) can join the Black sea, most of the year. The southwest vein (2) can continue along the southern coast of Crete feeding the western Cretan gyre and thereafter the Ierapetra gyre, mainly during summer. The MAW follows

the northward direction to feed two veins, one penetrating into the Adriatic and the other closing the circuit on the Eastern coast of the Sicily with the western Ionian gyre. Knowledge on water circulation decreases with depth. Notwithstanding this, the general circulation pattern of the second stratum is accepted to be as follow: LIW flows in a quite similar way than the superficial waters, but the flow in the Sicilian Strait is going westward (figure 2.3).

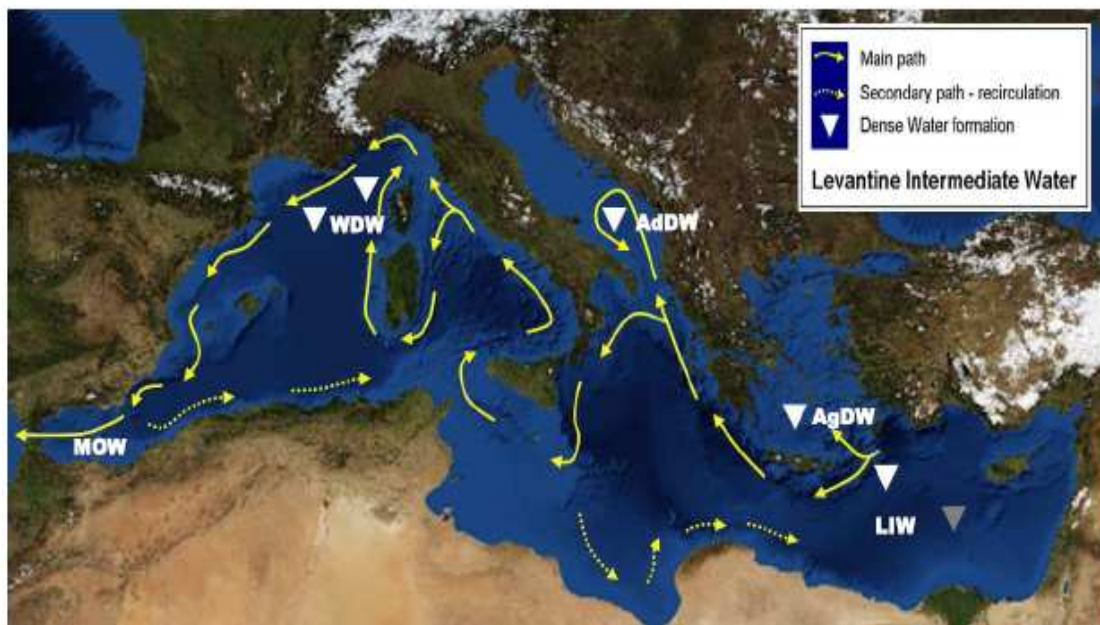


Fig. 2.3 Representation of the Levantine Intermediate Water circulation. *Adapted from: Pinardi and Masetti (2000); Millot and Taupier-Letage (2005).*

After its formation, the LIW divides into two branches, one going to the north and the other crossing the Ionian Sea to reach the Sicilian Strait. In the Occidental Basin, the LIW runs inside the Tyrrhenian and exists around the south of the Sardinian coast. Going northward, it participates in the Ligurian current and to the Lion Gyre. Then the LIW gets out into the Atlantic Ocean. The knowledge on deep water is limited: some chemical radioactive marks have been used to follow the MAW penetrating in the Mediterranean Sea, and they are nowadays assimilated in the DW masses.

These marks enable to describe the DW circulation (Béthoux et al., 1999). DW is divided into the Western Mediterranean Deep Water (WMDW) and the Eastern Mediterranean Deep Water (EMDW). The sill of the Strait of Sicily prevent a direct communication between the EMDW and the WMDW but coupling is achieved via the LIW layer. Most of DW have three origins: the Aegean sub basin, the Adriatic sub-basin and the Northwestern sub-basin (Wüst, 1961; Millot and Taupier-Letage, 2005; Lascaratos et al., 1999). The Adriatic DW are denser than Aegean DW, both accumulate in the southern part of their respective sub-basins and out-flow into the Levantine basin. The WMDW is formed in the North West part of the Mediterranean Sea, in the Gulf of Lion. WMDW forms a mid-basin cyclonic gyre, trapped in this basin by the deepest depth. Afterwards, some less dense waters continue along the Spanish coasts, to close the circuit along the African Coasts.

2.2.4 Deep and intermediate water formation

The dense water mass formation occurs in selected and restricted areas characterized by the presence of 3 particularities (Lascaratos et al., 1999):

- 1- cold and dry atmospheric masses;
- 2- cyclonic circulation where the centre does not allow strong stratification;
- 3- an increase of salinity by ice formation and/or by the rising up of the deeper water stratum richer in salts.

Those three factors are all present together in few areas of the Mediterranean Sea, and in very few places all over the planet (such as Weddel Sea, Labrador Sea). This phenomenon produces dense water sinking vertically from the superficial stratum to the deepest stratum of the ocean in few days, allowing exchanges of physical and biochemical proprieties; and it is strongly linked to meteorological fluctuations (Nittis and Lascaratos, 1999). Maintaining their identity, dense water indicates the climatic

conditions that led to their formation. Therefore, they are used to study climatic variations on a long time scale (Lascaratos et al., 1999). On the spatial scale, their formation maintains the global thermohaline circulation. In the Mediterranean Sea, two cells of DW are formed and are separated by the Sicilian sill. In February and March, the quite homogeneous vertical density distribution favours vertical convection provoked by strong winds (as Mistral or Bora) and forms the DW. The mean formation rate of the WMDW and the Adriatic DW cells is estimated to be of 0.3-1 Sv (Lascaratos, 1993; Nittis and Lascaratos, 1999). Other processes form other DW on local scales. In the case of the Aegean DW, its formation process leads to a water rich in oxygen, linked to an important grow of plankton in the euphotic stratum, usually poor in the oriental basin (Millot and Taupier-Letage, 2005). The LIW is produced with similar conditions, but only sinks at 200-500 m deep. This water mass is known to be formed in the permanent Rhodes cyclonic gyre in the NW part of the Levantine Basin (Ovchinnikov, 1984; Malanotte-Rizzoli & Hecht, 1988; Lascaratos et al., 1993). During summer, the surface layers of the Levantine Sea are occupied by a warm and salty water mass, the Levantine Surface Water (LSW). During winter, the LSW density increases and it sinks and mixes with underlying water inside the Rhodes cyclone.

2.2.5 Thermohaline axes

The Mediterranean circulation can be schematized in two cells interacting together as drawn on figure 2.4. One leading transport brings MAW to progressively change density by evaporation during its movement eastward; then, with LIW formation process, it returns westward. The second main transport is in the north-south direction with dense water formations. These two cells are totally linked together considering the partial transformation of LIW into dense water. Millot (1999) estimates that the Mediterranean

transit of a particle flowing from Gibraltar Strait might take a hundred years. In the Atlantic Ocean, the Mediterranean water can then be identified by its abnormal salinity (10% more salt content) and constitutes a stratum in the 1000-1500 m depth in the Atlantic Ocean (Turley, 1999). Its high density is fundamental for DW formation process on a global scale. And this highlights the key impact of Mediterranean Waters on global circulation (Béthoux et al., 1999).

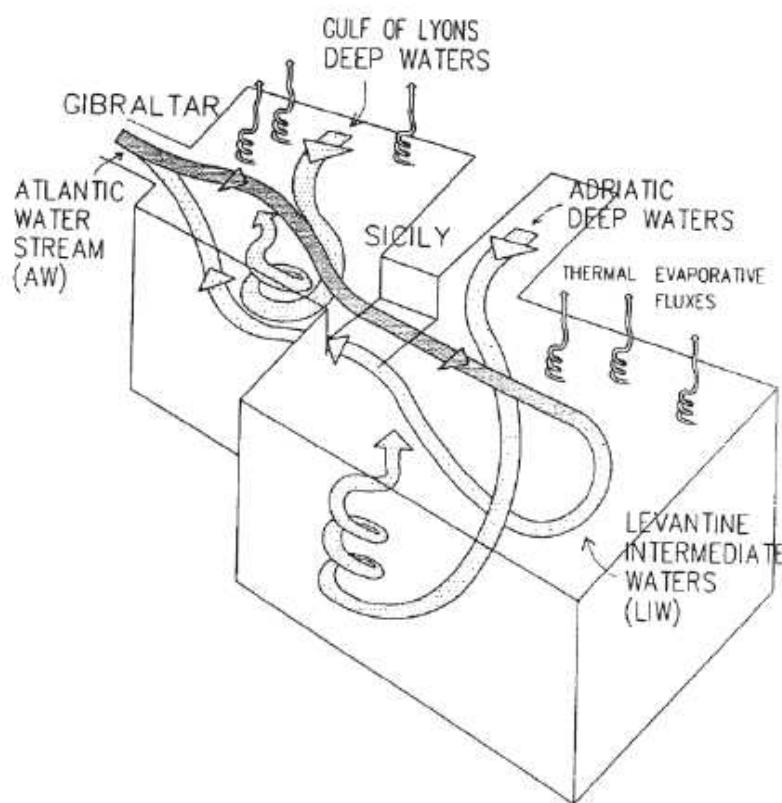


Fig. 2.4 Main features of the Mediterranean circulation: the East-West and the North-South thermohaline axes. *From: Lascaratos et al. (1999).*

2.3 Hydrodynamical features of the Ligurian Sea

The Ligurian Sea is an area with a wide extended bathyal plain of about 2500 m deep (its deepest point at 2746 m) associated with a quite inexistent continental shelf in the western part and a more extended shelf in the East (around 1100 m).

The major large scale hydrodynamical feature is a well-defined cyclonic circulation involving both the layers of the MAW and of the LIW (Astraldi et al., 1994). Two main currents, which are part of the general cyclonic circulation of the western Mediterranean Sea, enter into the Ligurian Sea: the Western Corsican Current (WCC) and the Eastern Corsican Current (ECC). Both advect MAW and the ECC includes also LIW. These two currents join in the North of Corsica and form the Ligurian-Provencal-Catalan current also called the Northern Current (NC). The NC flows along seafloor slope between 25 and 46 km offshore (Béthoux et al., 1988). Millot (1991) has shown that the major surface currents flowing along the coastal slope are affected by instability processes that generate mesoscale eddies, capable of inducing relatively intense currents and producing significant dynamical heterogeneity of the hydrological characteristics in this area.

The Ligurian Sea region is affected by severe weather condition in winter, which are mostly caused by the periodic intrusion of energetic, cold and dry continental wind, the Tramontana. Blowing over a warmer sea, the wind induce relevant air-sea interaction processes that subtract heat and water to the involved regions. Molcard et al. (2002) have suggested that the main features of the general circulation are induced by the structure of the wind stress curl, pointing out that the magnitude and spatial variability of the wind is essential in determining characteristics of the local circulations.

The Ligurian-Provencal-Catalan current has a maximum flux (1.5-2 Sv) during a relatively long winter season (roughly from December to May), and its structure markedly changes seasonally (Millot, 1999). This seasonal variation is mainly due to the variation of the ECC and the WCC which

form the Ligurian-Provencal-Catalan current. The variability of these currents is investigated by, e.g., Astraldi and Gasparini (1992) and Sammari et al. (1995) and shows a seasonal cycle and dependence on local atmospheric forcing. A peculiar feature of the connection between the Tyrrhenian and the Ligurian basins is that, in early winter, the ECC at all depths undergoes a sudden increase that maintains, with some oscillations, for the whole colder season. From late spring, the increase progressively vanishes (Astraldi et al., 1994). The WCC displays a seasonal variability too, though less pronounced than that on the ECC. With the lowest values in late summer and autumn, the WCC progressively increases in velocity to a maximum in early summer (May-June and early July) (Astraldi et al., 1994).

The Ligurian-Provencal-Catalan current generates frontal zones characterized by thermal, saline or density gradient. The front separates the current (dynamic zone) from the central water, characterized by a weaker stratification and by characteristics similar to those of LIW. The front exhibits numerous instable meanders and eddies driving vertical movements, discontinuous in time and space (Boucher et al., 1987). These mesoscale features are prevailing during winter and can also cause small-scale turbulences.

A pivotal physical process for the circulation in the seas is the deep water formation. It is generally thought that convective processes could occur in the central part of the Ligurian Sea where surface dense water (with characteristics between LIW and WMDW), weak vertical stability and vertical movement (5 to 7 cm s^{-1}) related to sinking water were observed during winter (Sparnocchia et al., 1995). Surface cooling and mixing can transform MAW into Winter Intermediate Water (WIW) that reaches the buoyancy equilibrium between the MAW and the LIW. This process can be compared to the dense water formation in the Gulf of Lions, but WIW

formation occurs for less severe weather conditions and only involves the MAW layer (Gasparini et al. 1999).

During the cold season, a high mesoscale activity associated with meanders in the NC, eddy formation or displacement in the Ligurian-Provencal front have been observed (Sammari, Millot and Prieur, 1995). The presence of mesoscale eddies is well documented in the western Mediterranean Sea and in the Ligurian Sea. For example, Santoleri et al. (1983) and Marullo et al. (1985) discuss observations of small submesoscale eddies ascribed to the baroclinic instability of the coastal current. The hydrographic measurements discussed by Gasparini et al. (1999) indicate the presence of winter intermediate water lenses, suggested to be the product of the sinking of water in the central region of the basin. Numerical simulations with regional models confirm the presence of intense mesoscale and submesoscale activity in the Ligurian Sea (Echevin et al., 2003).

In coastal regions and in the open ocean, mesoscale and submesoscale vortices play a crucial role in determining transport processes and the statistical properties of the mesoscale turbulence field (Provenzale, 1999; Bracco et al., 2000; 2003). In addition, eddies can significantly affect the dynamics of the marine ecosystem (Jenkins, 1988; Falkowski et al., 1991; McGillicuddy and Robinson, 1997; Abraham, 1998; Martin et al., 2002; Lévy and Klein, 2004; Pasquero et al., 2005). A particularly important aspect of mesoscale and submesoscaled eddies, rooted in the ageostrophic nature of the intense circulations associated with strong vortices, is the fact that they can generate significant upward and downward vertical velocities, up to 50 m/day, that are comparable with the strongest velocities found in proximity of frontal areas, as shown by Koszalka et al. (2009) in a study of coherent vortices in an idealized primitive-equation configuration representing the open ocean. Similarly, shallow-water mesoscale vortices impinging on a coastal slope generate a complex pattern of strong vertical velocities (Zavala Sanson and Provenzale, 2009). Such an intense vertical velocity field

provides a link between the nutrient-rich deep waters and the upper layer where phytoplankton thrive. For this reason, mesoscale and submesoscale eddies can play an important role in the fertilization of the euphotic layer of the ocean.

2.4 Main features of seasonal dynamic of primary production in the Ligurian Sea

The Mediterranean Sea is considered as oligotrophic, and characterized by low primary production (Margaleff, 1985; Minas et al., 1988). However, satellite imagery has exhibited the spatial and temporal heterogeneity of phytoplankton distribution (Morel and André, 1991). In the Ligurian Sea, spatial variations, are essentially related to the presence of the NC. In the central part of the basin the seasonal succession of hydrologic conditions induces the production systems varying from mesotrophy in spring to oligotrophy in summer and fall (Marty et al., 2002). The Ligurian Sea is subject to intense vertical convection, which mixes the cool dense surface water and the underlying saltier Levantine intermediate water during winter. The winter mixing brings nutrients into the upper layer but the short residence time of them in this layer prevents the development of biomass (Morel and André, 1991). Short periods of stabilization during winter, due to good weather conditions, can occur and are associated with short-lived diatom blooms (DYFAMED, 1995). Progressing in the year, the surface layer becomes stable over a long period, thus allowing the winter nutrient enrichment to be utilized continuously and it leads to a spring bloom. The bloom have observed between early April and mid-May (Morel and André, 1991). Oligotrophy prevails during summer while perturbations in the meteorological forcing can generate a secondary bloom in fall. As regard the vertical distribution of nutrients, in deep waters, nitrate concentrations range between 7 and 8 $\mu\text{mol Kg}^{-1}$, phosphate between 0,4 and

0,5 $\mu\text{mol Kg}^{-1}$, and silicate between 7 and 8 $\mu\text{mol Kg}^{-1}$ (Marty et al., 2002). Surface nutrient concentrations follow the general pattern of thermal stratification. Nitrate, phosphate and silicate concentrations reach, respectively, 2–3 $\mu\text{mol Kg}^{-1}$, 0.15–0.2 $\mu\text{mol Kg}^{-1}$ and 2–3 $\mu\text{mol Kg}^{-1}$ in surface layers during winter mixing conditions. The nutrient concentrations decrease in the surface layer with increasing stratification to reach undetectable levels (below 0.05 $\mu\text{mol Kg}^{-1}$) from June to November. The distribution of phytoplankton biomass follows the hydrographic and nutrient structure. Chlorophyll-a is maximal in surface layers during spring (bloom) in March and April. The maximum of biomass becomes less pronounced and descends to deeper layers (around 50 m) following the nitracline during summer and fall. The Chlorophyll-a is significantly present down to 50 m during the destratification process, and can reach 150–250m during the winter convective-mixing period depending of years (Marty et al., 2002). Some works indicate that phosphate is a limiting factor in the Mediterranean Sea (Béthoux et al., 1998; Coste et al., 1988), while other study suggest that Mediterranean waters could be nitrate limited (Andersen and Nival, 1988; Owens et al., 1989). In the central Ligurian Sea, it appears that there is a shift from nitrate limitation during winter and spring to phosphate limitation during the oligotrophic period. Marty et al. indicate that during the period of well established stratification (July, August and September), the N/P ratio below 200m is always around 20, but the data for the superficial (0–200 m) layer are always greater than 20. This confirms that the P-limitation is particularly important during the period of oligotrophy. In this respect, the potential inputs of P by rain (Migon and Sandroni, 1999) or by deposition of Saharan dusts (Bergametti et al., 1992) are very important during summer. The depth at which P concentration is significantly different from 0 is about 50 m. This is clearly consistent with the thickness of the stratified depth. In this sense, high values of N/P ratio also can be attributed to a shift between nitracline and phosphacline,

suggesting an incomplete utilization of nitrate by phytoplankton at the bottom of the euphotic zone due to the lack of phosphate (Raimbault and Coste, 1990). From November to February the N/P ratio is below 20 for relatively shallow waters (0-40 m) and over 20 in deeper layers (90-200 m). In this period, which is characteristic of low stratification, the limitation factor is essentially due to nitrate in surface waters (where most of the production occurs). Different study (Marty et al., 2002; Barlow et al., 1993; Claustre and Marty, 1995) indicate that the dominant group of phytoplankton, in the western Mediterranean Sea, is the prymnesiophytes and that this predominance is independent of seasons. The 10 years study of Marty et al., indicates a large abundance of diatoms and, this abundance, is variable with time particularly associated to blooms. The diatoms are opportunistic species (Fogg, 1991), which bloom as soon as stratification breaks down and nutrients are already present, due to winter mixing. Diatoms are well known to be responsible of spring blooms and likely main contributors to the new production in the open ocean (Goldman, 1993; Claustre, 1994), and to high particle fluxes associated to the bloom period (Miquel et al., 1994).

The description of the distribution and the seasonal evolution of nutrients allows, in part, to define the evolution of the primary production. The production of biomass depends mainly on the availability of nutrients and light. The distribution and evolution of primary production follows the hydrographic and nutrients structure. The field data collected at the DYFAMED station during the Tanaka and Rassoulzadegan seasonal study (Tanaka and Rassoulzadegan, 2002) indicates a range of value of primary production integrated in the upper 90 m during the different months of the year, between 65 (July) to 378 (May) $\text{mgCm}^{-2}\text{d}^{-1}$. The maximum value of primary production is reached in May after the start of chlorophyll spring bloom when hydrodynamic and atmosphere conditions are stable and nutrients are available into the euphotic layer. During the study, the

CHAPTER 2: SCIENTIFIC BACKGROUND AND OBJECTIVES

minimum value of primary production has been measured in July when oligotrophy prevails.

3 Numerical Models

3.1 Ocean Models

Numerical ocean modeling is a relatively young field. The very first comprehensive numerical global baroclinic ocean model was formulated by Kirk Bryan in the late sixties (Bryan, 1969). However, the advent of high performance computers has led to a phenomenal growth in the field, especially in the last decade.

3.1.1 Types, advantages and limitations of ocean models

Numerical ocean models can be classified in many different ways. The following is a version of Kantha and Clayson (2000).

Global or regional. The former necessarily requires high performance computing capabilities, whereas it may be possible to run the latter on powerful modern workstations. Even then, the resolution demanded (grid size in the horizontal and vertical) is critical. A doubling of the resolution in a three-dimensional model requires almost an order of magnitude increase in computing (and analysis) resources. Regional models have to contend with the problem of how to inform the model about the state of the rest of the ocean.

Deep basin or shallow coastal. The prevailing physical processes and the underlying driving mechanisms are essentially different for the two. Circulation in shallow coastal regions is highly variable, driven primarily by synoptic wind and other rapidly changing surface forcing (and near river outflows, by buoyancy differences between the fresh river water and the saline ambient shelf water). Wind mixing at the surface and processes at the bottom are important, and a numerical model that has reliable mixing physics and which resolves the bottom boundary layer is therefore better

suited to coastal applications. Deep basin, on the other hand, are comparatively sluggish, and the horizontal density gradients, especially below the wind-mixed upper layers, are a dominant factor in the circulation. The upper mixed layer can often be modelled less rigorously, especially for applications that do not require consideration of air-sea interaction processes.

Rigid lid or free surface. Oceanic response to surface forcing can often be divided into two parts: fast barotropic response mediated by external Kelvin and gravity waves on the sea surface, and relatively slower baroclinic adjustment via internal gravity, Kelvin, planetary Rossby, and other waves. On long timescales, it is the internal adjustment that is important to model and it is possible to suppress the external gravity waves by imposing a “rigid lid” on the free surface. This permits larger time stepping of the model, and models used for climatic-type simulation are usually of the rigid lid kind. Free surface models, implicit and explicit, are becoming more popular for nonclimatic simulation. A mode-splitting technique must then be employed to circumvent the severe limitation on time stepping that would otherwise be imposed by the presence of fast external modes.

Hydrostatic, quasihydrostatic, or nonhydrostatic. Most large scale circulation models for the oceans (and the atmosphere) are based on the hydrostatic form of the incompressible Navier-Stokes equations. This exploits the fact that the ratio of vertical to horizontal scales of motion is usually small and the static stability of the water column in the stably stratified oceans is significant. While they are adequate in modelling gyre scale (≥ 1000 km) circulation and mesoscale eddies (10-100 km), the hydrostatic approximation breaks down for scales less than the ~ 10 km typical of small scale processes such as deep convective chimneys which have horizontal scales of typically 1 km. Hydrostatic approximation also requires neglecting the horizontal component of Coriolis acceleration for energetic consistency, which means that the angular momentum is only

approximately conserved. Approximation where the strict hydrostatic approximation is relaxed to the extent that the horizontal component of the Coriolis acceleration is retained is known as quasi-hydrostatic approximation (White and Bromley, 1995). Fully nonhydrostatic models (Jones and Marshall, 1993; Marshall *et al.*, 1997a,b) can be used at all horizontal scales, but unlike hydrostatic models that require the inversion of only a two-dimensional elliptic equation, they involve the solution of a three-dimensional elliptic equation subject to Neumann boundary conditions, and can therefore be computationally intensive.

Quasi-geostrophic or primitive equation based. Quasi-geostrophic models assume that there is a near balance between the Coriolis acceleration and the pressure gradient in the dynamical equations in the rotating coordinate frame of reference in which most ocean models are formulated. This filters out fast gravity waves, and the resulting simplification enables longer time steps to be taken at a given resolution, or equivalently higher vertical and horizontal resolutions for a given computing capability to be achieved. Quasi-geostrophic models have strong limitations with respect to the accuracy with which some physical processes can be depicted, and are becoming obsolete in the modern high computing power environment.

Barotropic or baroclinic. In a barotropic model, the density gradient are neglected so that the current become independent of the depth in the water column. Many phenomena such as tidal sea surface elevation fluctuations and storm surges can be simulated quite adequately by a barotropic model, which is a two-dimensional (in the horizontal) model based on the vertically integrated equations of motion. One of its advantages is that it requires an order of magnitude less computing resources than a comparable baroclinic model. However, when it is important to model the vertical structure of currents, or the density field, a fully three-dimensional baroclinic model is necessary.

Purely physical or physical-chemical-biological. To model the fate of chemical and biological constituent in the ocean it is essential to solve not only the dynamical equations governing the circulation and other physical variables, but also the conservation equations for chemical and biological variables. The governing equations are transport equations with appropriate source and sink terms, whose parameterization is not always quite straightforward. This implies not only additional complexity but also requires more computing (and data) resources.

Process studies-oriented or applications-oriented. Models that are used to study some salient processes (for example, western boundary currents and gyre circulation) can be considerably simplified and hence made less computationally intensive, since it is often possible to isolate and retain only the relevant physical process, and ignore the rest. On the other hand, applications-oriented models such as those used for ocean prediction purposes require extensive observational data for realistic initialization forcing, and data assimilation.

3.2 ROMS, Regional Ocean Modeling System

In this chapter the ROMS modelling system and the configuration used have been described. Before to start with the section, I wish to thank Pierrick Penven for providing me the ROMS code with its pre and post processing tools (<http://roms.mpl.ird.fr/>) which helped me in the development of this work. Proceeding, the first section of this chapter is a general description of the main characteristics of the model while the next ones show the model's equations and their description (source: ROMSTOOLS user's guide by Pierrick Penven and Thi-Anh Tan, myroms.org and literature).

3.2.1 *Model description*

The Regional Ocean Modeling System (ROMS) is a new generation ocean circulation model (Shchepetkin and McWilliams, 2005) that has been designed for simulation of regional oceanic system. ROMS solves the primitive equations in an Earth-centered rotating environment, based on the Boussinesq approximation and hydrostatic vertical momentum balance. ROMS is discretized in coastline and terrain following curvilinear coordinates. The hydrostatic primitive equations for momentum are solved using a split-explicit time-stepping scheme which requires special treatment and coupling between barotropic (fast) and baroclinic (slow) modes. A finite number of barotropic time steps, within each baroclinic step, are carried out to evolve the free-surface and vertically integrated momentum equations. In order to avoid the errors associated with the aliasing of frequencies resolved by the barotropic steps but unresolved by the baroclinic step, the barotropic fields are time averaged before they replace those values obtained with a longer baroclinic step. A cosine-shape time filter, centred at the new time level, is used for the averaging of the barotropic fields (Shchepetkin and McWilliams, 2005). In addition, the separated time-stepping is constrained to maintain exactly both volume conservation and consistency preservation properties which are needed for the tracer equations (Shchepetkin and McWilliams, 2005). 2D and 3D equations are time-discretized using a third-order accurate predictor (Leap-Frog) and corrector (Adams-Molton) time-stepping algorithm which is very robust and stable. The enhanced stability of the scheme allows a substantial increase in the permissible time-step size.

In the vertical, the primitive equations are discretized over variable topography using stretched terrain-following coordinates (Song and Haidvogel, 1994). The stretched coordinates allow increased resolution in areas of interest, such as thermocline and bottom boundary layers. In this

configuration of ROMS model we use centred, second-order finite differences on a staggered vertical grid.

In the horizontal, the primitive equations are evaluated using boundary-fitted, orthogonal curvilinear coordinates on a staggered Arakawa C-grid. The general formulation of curvilinear coordinates includes both Cartesian (constant metrics) and spherical (variable metrics) coordinates. Coastal boundaries can also be specified as a finite-discretized grid via land/sea masking. As in the vertical, the horizontal stencil utilizes a centred, second-order finite differences.

ROMS has various options for advection schemes: second- and forth-order centred differences; and third-order, upstream biased. The configuration utilized in the simulations presented in this work of thesis is the third-order, upstream biased. This scheme has a velocity-dependent hyper-diffusion dissipation as the dominant truncation error and it allows the generation of steep gradients, enhancing the effective resolution of the solution for a given grid size (Shchepetkin and McWilliams, 2008).

There are several subgrid-scale parameterizations in ROMS. The horizontal mixing of momentum and tracers can be along vertical levels, geopotential (constant depth) surfaces, or isopycnic (constant density) surfaces. The mixing operator can be harmonic (3-point stencil) or biharmonic (5-point stencil). In this configuration the horizontal mixing of momentum is along geopotential surfaces.

The vertical mixing parameterization in ROMS can be either by local or nonlocal closure schemes. The local closure schemes are based on the level 2.5 turbulent kinetic energy equations by Mellor and Yamada (1982) and the Generic Length Scale (GLS) parameterization (Umlauf and Burchard, 2003). The nonlocal closure scheme is based on the K-profile, boundary layer formulation by Large et al. (1994). The K-profile scheme has been expanded to include both surface and bottom oceanic boundary layers. The GLS is a two-equation turbulence model that allows a wide range of vertical mixing

closures, including the popular k-kl (Mellor-Yamada level 2.5), k-e, and k-w schemes. A recent study (Warner et al., 2005a) evaluated the performance of these turbulence closures in ROMS in terms of idealized sediment transport applications. In addition, there is a wave/current bed boundary layer scheme that provides the bottom stress (Styles and Glenn, 2000) and sediment transport which become important in coastal applications. In this ROMS configuration we use the non-local, K-profile planetary (KPP) boundary layer scheme which parameterized the unresolved physical vertical subgrid-scale processes. Explicit lateral viscosity is null everywhere in the model domain except in sponge layer near the open boundaries where it increases smoothly close to the lateral open boundaries.

If a lateral boundary faces the open ocean, an active, implicit, upstream biased, radiation condition connects the model solution to the surroundings (Marchesiello et al., 2001).

The time step of the ROMS configuration used is chosen from the CFL criterion.

The ROMS configuration used has a nesting capability. The method used for embedding gridding is the AGRIF (Adaptive Grid Refinement in Fortran) package (Debreu and Blayo, 2003; Debreu and Vouland, 2003). AGRIF is a Fortran 90 package for the inclusion of adaptive mesh refinement features within a finite-difference numerical model. To preserve the CFL criterion, for a typical coefficient of refinement r_{coef} (factor of 3), for each parent time step the child must be advanced using a time step divided by the coefficient of refinement as many time as necessary to reach the time of the parent. A 2-level embedding has been done in the thesis. In this case, the procedure is as follows:

- a) Advance the parent grid by one parent time step;
- b) Interpolate the parent variables in space and time to get the boundary conditions for the child grid;

- c) Advance the child grid by as many child steps as necessary to reach the new parent model time.

The air-sea interaction boundary layer in ROMS is based on the bulk parameterization of Fairall et al. (1996). It was adapted from the COARE (Coupled Ocean-Atmosphere Response Experiment) algorithm for the computation of surface fluxes of momentum, sensible heat, and latent heat.

The entire input and output data structure of the model is via NetCDF (Network Common Data Form) which is a set of software libraries and machine-independent data formats that support the creation, access, and sharing of array-oriented scientific data.

3.2.2 Model formulation

3.2.2.1 Equations of motion

In this sub-section the primitive equations in Cartesian coordinates have been showed. The momentum balance in the x and y directions are:

$$\frac{\partial u}{\partial t} + \bar{v} \cdot \nabla u - fv = -\frac{\partial \phi}{\partial x} - \frac{\partial}{\partial z} \left(\overline{u'w'} - v \frac{\partial u}{\partial z} \right) + F_u + D_u$$

$$\frac{\partial v}{\partial t} + \bar{v} \cdot \nabla v - fu = -\frac{\partial \phi}{\partial y} - \frac{\partial}{\partial z} \left(\overline{v'w'} - v \frac{\partial v}{\partial z} \right) + F_v + D_v$$

The time evolution of a scalar concentration field, $C(x,y,z,t)$ (e.g. salinity, temperature, or nutrients), is governed by the advective-diffusive equation:

$$\frac{\partial C}{\partial t} + \bar{v} \cdot \nabla C = -\frac{\partial}{\partial z} \left(\overline{C'w'} - v_\theta \frac{\partial C}{\partial z} \right) + F_c + D_c$$

The equation of state is given by:

$$\rho = \rho(T, S, P)$$

In the Bussinesq approximation, density variations are neglected in the momentum equations except in their contribution to the buoyancy force in the vertical momentum equation. Under the hydrostatic approximation, it is

further assumed that the vertical pressure gradient balances the buoyancy force:

$$\frac{\partial \phi}{\partial z} = -\frac{\rho g}{\rho_0}$$

The continuity equation for an incompressible fluid is:

$$\frac{\partial u}{\partial x} + \frac{\partial v}{\partial y} + \frac{\partial w}{\partial z} = 0$$

The effects of forcing and horizontal dissipation are represented by the schematic terms F and D respectively.

The variables used are shown here:

Variable	Description
D_u, D_v, D_C	Diffusive terms
F_u, F_v, F_C	Forcing terms
$f(x, y)$	Coriolis parameter
g	Acceleration of gravity
$H(x, y)$	Bottom depth
ν, ν_θ	Molecular viscosity and diffusivity
K_m, K_C	Vertical eddy viscosity and diffusivity
P	Total pressure $P \approx -\rho_0 g z$
$\phi(x, y, z, t)$	Dynamic pressure $\phi = P / \rho_0$
$\rho_0 + \rho(x, y, z, t)$	Total in situ density
$S(x, y, z, t)$	Salinity
t	Time
$T(x, y, z, t)$	Potential temperature
u, v, w	The (x, y, z) components of vector velocity \vec{v}
x, y	Horizontal coordinates
z	Vertical coordinate
$\zeta(x, y, t)$	The surface elevation

These equations are closed by parameterizing the Reynolds stresses and turbulent tracer fluxes as:

$$\overline{u'w'} = -K_M \frac{\partial u}{\partial z}; \quad \overline{v'w'} = -K_M \frac{\partial v}{\partial z}; \quad \overline{C'w'} = -K_M \frac{\partial C}{\partial z}.$$

The overbar represents a time average and the prime represents a fluctuation about the mean.

The vertical boundary conditions can be prescribed as follows:

top ($z = \zeta(x, y, t)$):

$$K_m \frac{\partial u}{\partial z} = \tau_s^x(x, y, t)$$

$$K_m \frac{\partial v}{\partial z} = \tau_s^y(x, y, t)$$

$$K_c \frac{\partial C}{\partial z} = \frac{Q_C}{\rho_0 c_p}$$

$$w = \frac{\partial \zeta}{\partial t}$$

and bottom ($z = -h(x, y)$):

$$K_m \frac{\partial u}{\partial z} = \tau_b^x(x, y, t)$$

$$K_m \frac{\partial v}{\partial z} = \tau_b^y(x, y, t)$$

$$K_c \frac{\partial C}{\partial z} = 0$$

$$-w + \vec{v} \cdot \nabla h = 0$$

The new variables above are:

Variable	Description
Q_C	Surface concentration flux
τ_s^x, τ_s^y	Surface wind stress
τ_b^x, τ_b^y	Bottom stress

The surface boundary condition variables are defined in the table above. On the variable bottom, $z = -h(x, y)$, the horizontal velocity components are constrained to accommodate a prescribed bottom stress. The vertical scalar concentration fluxes are set to zero.

In this configuration we use the code for an open boundaries case. Appropriate boundary conditions are provided for u , v , C and ζ as described in section 4.3. The model domain is rectangular with the mask on land areas. Boundary conditions on these masked regions are straightforward, with a choice of no-slip or free-slip walls.

The model use biharmonic friction. The high order boundary conditions used for u are $\frac{\partial}{\partial x} \left(\frac{hv}{mn} \frac{\partial^2 u}{\partial x^2} \right) = 0$ on the eastern and western boundaries and

$\frac{\partial}{\partial y} \left(\frac{hv}{mn} \frac{\partial^2 u}{\partial y^2} \right) = 0$ on the northern and southern boundaries. The boundary

conditions for v e C are similar. These boundary conditions were chosen because they preserve the property of no gain or loss of volume-integrated momentum or scalar concentration.

3.2.2.2 Vertical Terrain-Following Coordinates

ROMS model uses vertical terrain-following coordinate system. The coordinate transformation is:

$$\hat{x} = x$$

$$\hat{y} = y$$

$$\sigma = \sigma(x, y, z)$$

$$z = z(x, y, \sigma)$$

$$\hat{t} = t$$

In the stretched system, the vertical coordinate σ spans the range $-1 \leq \sigma \leq 0$. The upper level is $\sigma = 0$ and the lower one is $\sigma = -1$.

The chain rules for this transformation are:

$$\left(\frac{\partial}{\partial x}\right)_z = \left(\frac{\partial}{\partial x}\right)_\sigma - \left(\frac{1}{H_z}\right)\left(\frac{\partial z}{\partial x}\right)_\sigma \frac{\partial}{\partial \sigma}$$

$$\left(\frac{\partial}{\partial y}\right)_z = \left(\frac{\partial}{\partial y}\right)_\sigma - \left(\frac{1}{H_z}\right)\left(\frac{\partial z}{\partial y}\right)_\sigma \frac{\partial}{\partial \sigma}$$

$$\frac{\partial}{\partial z} = \left(\frac{\partial \sigma}{\partial z}\right) \frac{\partial}{\partial \sigma} = \frac{1}{H_z} \frac{\partial}{\partial \sigma}$$

where:

$$H_z \equiv \frac{\partial z}{\partial \sigma}$$

The dynamic equations become more complicated after dropping the carats:

$$\frac{\partial u}{\partial t} - f v + \vec{v} \cdot \nabla u = -\frac{\partial \phi}{\partial x} - \left(\frac{g\rho}{\rho_0}\right) \frac{\partial z}{\partial x} - g \frac{\partial \zeta}{\partial x} + \frac{1}{H_z} \frac{\partial}{\partial \sigma} \left[\frac{(K_m + \nu)}{H_z} \frac{\partial u}{\partial \sigma} \right] + F_u + D_u$$

$$\frac{\partial v}{\partial t} - f u + \vec{v} \cdot \nabla v = -\frac{\partial \phi}{\partial y} - \left(\frac{g\rho}{\rho_0}\right) \frac{\partial z}{\partial y} - g \frac{\partial \zeta}{\partial y} + \frac{1}{H_z} \frac{\partial}{\partial \sigma} \left[\frac{(K_m + \nu)}{H_z} \frac{\partial v}{\partial \sigma} \right] + F_v + D_v$$

$$\frac{\partial C}{\partial t} + \vec{v} \cdot \nabla C = \frac{1}{H_z} \frac{\partial}{\partial \sigma} \left[\frac{(K_m + \nu)}{H_z} \frac{\partial C}{\partial \sigma} \right] + F_c + D_c$$

$$\rho = \rho(T, S, P)$$

$$\frac{\partial \phi}{\partial \sigma} = \left(\frac{-g H_z \rho}{\rho_0} \right)$$

$$\frac{\partial H_z}{\partial t} + \frac{\partial(H_z u)}{\partial x} + \frac{\partial(H_z v)}{\partial y} + \frac{\partial(H_z \Omega)}{\partial \sigma} = 0$$

where:

$$\vec{v} = (u, v, \Omega)$$

$$\vec{v} \cdot \nabla = u \frac{\partial}{\partial x} + v \frac{\partial}{\partial y} + \Omega \frac{\partial}{\partial \sigma}$$

The vertical velocity in σ coordinate is:

$$\Omega(x, y, \sigma, t) = \frac{1}{H_z} \left[w - \frac{z + h \partial \zeta}{\zeta + h \partial t} - u \frac{\partial z}{\partial x} - v \frac{\partial z}{\partial y} \right]$$

and

$$w = \frac{\partial z}{\partial t} + u \frac{\partial z}{\partial x} + v \frac{\partial z}{\partial y} + \Omega H_z$$

In the stretched coordinate system, the vertical boundary conditions become

Top ($\sigma = 0$):

$$\left(\frac{K_m}{H_z} \right) \frac{\partial u}{\partial \sigma} = \tau_s^x(x, y, t)$$

$$\left(\frac{K_m}{H_z} \right) \frac{\partial v}{\partial \sigma} = \tau_s^y(x, y, t)$$

$$\left(\frac{K_c}{H_z} \right) \frac{\partial C}{\partial \sigma} = \frac{Q_c}{\rho_0 c_p}$$

$$\Omega = 0$$

and bottom ($\sigma = -1$):

$$\left(\frac{K_m}{H_z} \right) \frac{\partial u}{\partial \sigma} = \tau_b^x(x, y, t)$$

$$\left(\frac{K_m}{H_z} \right) \frac{\partial v}{\partial \sigma} = \tau_b^y(x, y, t)$$

$$\left(\frac{K_c}{H_z} \right) \frac{\partial C}{\partial \sigma} = 0$$

$$\Omega = 0$$

The σ coordinate transformation allows the simplification of the boundary conditions on vertical velocity that we can see in the above equations.

3.2.2.3 *Horizontal Curvilinear Coordinates*

In coastal application, like in this application, the fluid is confined horizontally within an irregular region. In such problems, a horizontal coordinate system which conforms to the irregular lateral boundaries is advantageous. It is often also true in many geophysical problems that the simulated flow fields have regions of enhanced structure (e.g., boundary currents or fronts) which occupy a relatively small fraction of the

physical/computational domain. In these problems, added efficiency can be gained by placing more computational resolution in such regions.

ROMS has an appropriate orthogonal coordinate transformation in the horizontal which allows a boundary-following coordinate system and a laterally variable grid resolution. The new coordinate are $\xi(x, y)$ and $\eta(x, y)$, where the relationship of horizontal arc length to the differential distance is given by:

$$(ds)_\xi = \left(\frac{1}{m}\right) d\xi$$

$$(ds)_\eta = \left(\frac{1}{n}\right) d\eta$$

$m(\xi, \eta)$ and $n(\xi, \eta)$ are the scale factors which relate the differential distance $(\Delta\xi, \Delta\eta)$ to the physical arc lengths.

The velocity components in the new coordinate system are:

$$\vec{v} \cdot \hat{\xi} = u$$

$$\vec{v} \cdot \hat{\eta} = v$$

the equation of motion can be re-written as:

$$\begin{aligned} & \frac{\partial}{\partial t} \left(\frac{H_z u}{mn} \right) + \frac{\partial}{\partial \xi} \left(\frac{H_z u^2}{n} \right) + \frac{\partial}{\partial \eta} \left(\frac{H_z uv}{m} \right) + \frac{\partial}{\partial \sigma} \left(\frac{H_z u \Omega}{mn} \right) - \left\{ \left(\frac{f}{mn} \right) + v \frac{\partial}{\partial \xi} \left(\frac{1}{n} \right) - \frac{\partial}{\partial \eta} \left(\frac{1}{m} \right) \right\} H_z v = \\ & - \left(\frac{H_z}{n} \right) \left(\frac{\partial \phi}{\partial \xi} + \frac{g\rho}{\rho_0} \frac{\partial z}{\partial \xi} + g \frac{\partial \zeta}{\partial \xi} \right) + \frac{1}{mn} \frac{\partial}{\partial \sigma} \left[\frac{(K_m + \nu)}{H_z} \frac{\partial u}{\partial \sigma} \right] + \frac{H_z}{mn} (Fu + Du) \end{aligned}$$

$$\begin{aligned} & \frac{\partial}{\partial t} \left(\frac{H_z v}{mn} \right) + \frac{\partial}{\partial \xi} \left(\frac{H_z uv}{n} \right) + \frac{\partial}{\partial \eta} \left(\frac{H_z v^2}{m} \right) + \frac{\partial}{\partial \sigma} \left(\frac{H_z v \Omega}{mn} \right) + \left\{ \left(\frac{f}{mn} \right) + v \frac{\partial}{\partial \xi} \left(\frac{1}{n} \right) - \frac{\partial}{\partial \eta} \left(\frac{1}{m} \right) \right\} H_z u = \\ & - \left(\frac{H_z}{n} \right) \left(\frac{\partial \phi}{\partial \eta} + \frac{g \rho}{\rho_0} \frac{\partial z}{\partial \eta} + g \frac{\partial \zeta}{\partial \eta} \right) + \frac{1}{mn} \frac{\partial}{\partial \sigma} \left[\frac{(K_m + \nu)}{H_z} \frac{\partial v}{\partial \sigma} \right] + \frac{H_z}{mn} (F_v + D_v) \end{aligned}$$

$$\begin{aligned} & \frac{\partial}{\partial t} \left(\frac{H_z C}{mn} \right) + \frac{\partial}{\partial \xi} \left(\frac{H_z u C}{n} \right) + \frac{\partial}{\partial \eta} \left(\frac{H_z v C}{m} \right) + \frac{\partial}{\partial \sigma} \left(\frac{H_z \Omega C}{mn} \right) = \\ & + \frac{1}{mn} \frac{\partial}{\partial \sigma} \left[\frac{(K_m + \nu)}{H_z} \frac{\partial C}{\partial \sigma} \right] + \frac{H_z}{mn} (F_C + D_C) \end{aligned}$$

$$\rho = \rho(T, S, P)$$

$$\frac{\partial \phi}{\partial \sigma} = - \left(\frac{g H_z \rho}{\rho_0} \right) \frac{\partial}{\partial t} \left(\frac{H_z}{mn} \right) + \frac{\partial}{\partial \xi} \left(\frac{H_z u}{n} \right) + \frac{\partial}{\partial \eta} \left(\frac{H_z v}{m} \right) + \frac{\partial}{\partial \sigma} \left(\frac{H_z \Omega}{mn} \right) = 0$$

All boundary conditions remain unchanged.

3.2.3 Parameterization of sub-grid process

In this ROMS configuration, the diffusion scheme non-local K profile parameterization (KPP) for the vertical mixing and Laplacian horizontal mixing in sponge layer for the lateral mixing, are used.

3.2.3.1 Non-local K profile parameterization (KPP)

Ocean vertical mixing requires two distinct parameterizations: one for the ocean interior and one for the ocean surface boundary layer. The KPP vertical mixing parameterizations were developed for both, the OBL (Ocean Boundary Layer) and the oceanic interior. The OBL scheme has the following characteristics:

- 1) both the convective and the wind-driven boundary layers can penetrate well into the stratified region below a mixed layer. Even though such events may be short-lived, the resulting vertical fluxes can be large enough to have a significant impact on much longer timescales. Only with such penetration can the large diffusivities that represent the efficient mixing of boundary layer eddies act upon the large property gradients typically found below a mixed layer;
- 2) it is relatively insensitive to vertical resolution and may perform well in low-resolution configurations;
- 3) if it is given the correct surface forcing and advective transports, it will distribute properties properly in the vertical;
- 4) it is consistent with similarity theory; in the surface layer, the boundary layer is capable of penetrating the interior stratification (exchanges of properties between the mixed layer and thermocline), and turbulent transport vanishes at the surface;
- 5) the parameterization has been formulated to be run off surface fluxes, so it is readily coupled to an atmosphere or sea ice model.

The model's ability to exchange properties between the mixed layer and deeper stratified waters may become an essential ingredient of any model used to study mixed-layer biogeochemistry.

All forcing functions are defined to be positive when they act to increase the oceanic values of the property being transferred. Thus positive forcing moves properties downward into the ocean. The time evolution of a property X due to PBL eddies is expressed as the vertical divergence of the kinematic turbulent fluxes:

$$\partial_t X = -\partial_z \overline{w \cdot x}$$

X = represents mean quantity of a property

x = represents turbulent fluctuation of a property

w = turbulent vertical velocities

It is assumed that turbulent diffusion is down-gradient, depending linearly on the local property gradient, with an appropriate eddy diffusivity K_x , the constant of proportionality:

$$\overline{w \cdot x} = -K_x \partial_z X$$

The problem of determining the vertical turbulent fluxes of momentum and both active and passive scalars throughout the OBL is closed by adding a nonlocal transport term:

$$\overline{w \cdot x(d)} = -K_x (\partial_z X - \gamma_x)$$

d = distance from the boundary

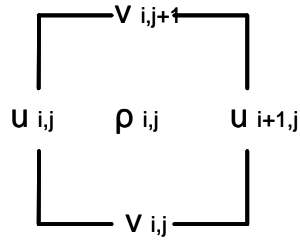
h = boundary layer depth (limit to which boundary layer eddies can penetrate in the vertical)

In practice, the external forcing is first prescribed, then the boundary layer depth, h , is determined, and finally profiles of the diffusivity and nonlocal transport are computed (Large *et al.*, 1994).

3.2.4 Numerical Solution Technique

3.2.4.1 Horizontal Discretization

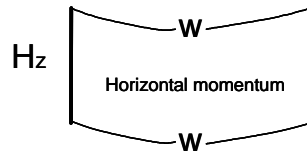
In the horizontal, the ROMS governing equations are discretized over a boundary-fitted, orthogonal curvilinear coordinates (ξ, η) grid as described in section 3.2.2.3. The general formulation of the curvilinear coordinates system allows Cartesian, polar and spherical coordinates applications. The transformation of any of these coordinates in ROMS (ξ, η) grid is specified in the metric terms (pm, pn) . The model state variables are staggered using an Arakawa C-grid. The free-surface ($zeta$), density (rho), and active/passive tracers (t) are located at the centre of the cell whereas the horizontal velocity (u and v) are located at the west/east and south/north edges of the cell, respectively. The density is evaluated between points where the currents are evaluated. It is showed in the figure below.



3.2.4.2 Vertical Discretization

The ROMS governing equations are discretized over variable topography using a stretched, terrain-following, vertical coordinate. As a result, each grid cell may have different level thickness (H_z) and volume. The model state variables are vertically staggered so that horizontal momentum (u, v), (ρ), and active/passive tracers (t) are located at the centre of the grid cell. The vertical velocity (ω, w) and vertical mixing variables ($Akt, Akv, etc.$) are located at the bottom and top faces of cell.

It is shown in the figure below.



The total thickness of the water column is $\zeta(i, j) + h(i, j)$. The bathymetry (h) is usually time invariant whereas the free-surface (ζ) evolves in time. At input and output, the bathymetry is always a positive quantity. However, the depths $z_r(i, j, k)$ and $z_w(i, j, k)$ are negative for all locations below the mean sea level.

3.2.4.3 *Time Stepping Scheme*

Numerical time stepping uses a discrete approximation to equations. The momentum equations are advanced before the tracer equation by computing the terms using the implicit scheme to find the new values for u and v . The tracer concentration equation is advanced in a predictor-corrector leapfrog-trapezoidal step, optimizing both the conservation and constancy-preserving properties of the continuous equations.

3.3 Biogeochemical Model

In this chapter the state of the art of plankton models and the biogeochemical model used in the simulations presented in this work of thesis have been presented.

Numerical modelling can help to predict ecological events over an appropriate time scale and provide strategies for marine resource management and exploitation. Various mathematical formulations have been developed to describe fundamental biological processes and forcing functions. There are two basic functions of nutrient limitation on phytoplankton growth, the Michaelis-Menten function and the Droop function, but different formulations have been developed and used in numerical simulation, with 6 functions of ammonium inhibition on nitrate uptake, 13 of light forcing on phytoplankton growth, 5 of nutrient limitation and 10 of temperature forcing on biological rates (Tian, 2006). More confusing are parameterizations of zooplankton feeding, 20 equations for feeding on a single type of prey and 15 for feeding on multiple types of prey (Tian, 2006). However, the intrinsic complexity in trophic dynamics and diversity in ecosystem function prohibit the progress in standardizing parameterization in ecological and biological models. Numerical models have the limitation in simulating and predicting the complexity of marine ecosystems. In practice the accuracy of numerical simulation depend on the quality of the data set used to constrain the model. (Tian, 2006). In this work of thesis our aim is not to predict ecological event but we focus the study on mesoscale processes and on the influence that mesoscale structures have on biological processes.

3.3.1 State of the art of Plankton models

The simplest Plankton model is Nutrient-Phytoplankton-Zooplankton (NPZ) model. NPZ models have been in use in oceanography for at least three

decades, and are still a common research tool (Franks, 2002). The NPZ model incorporate one of the simplest sets of dynamics that usefully describe oceanic plankton dynamics. A general set of NPZ model equations can be written:

$$\frac{dP}{dt} = f(I)g(N)P - h(P)Z - i(P)P$$

$$\frac{dZ}{dt} = \gamma h(P)Z - j(Z)Z$$

$$\frac{dN}{dt} = -f(I)g(N)P + (1 - \gamma)h(P)Z + i(P)P + j(Z)Z$$

There are 5 transfer function to consider: phytoplankton response to light $f(I)$, phytoplankton nutrient uptake $g(N)$, zooplankton grazing $h(P)$, and phytoplankton $i(P)$ and zooplankton $j(Z)$ loss terms due to death, excretion, and predation by organisms not included in the model. Zooplankton assimilation γ is typically modelled as a simple linear function of food ingested. The phytoplankton response to irradiance $f(I)$ range from a simple linear response to incident light, to non linear forms of saturating and photo inhibiting response. Most commonly nutrient uptake by phytoplankton $g(N)$ is modelled by the Michaelis-Menten formulation $(\frac{V_m}{K_s + N})$. This formulation was introduced to phytoplankton ecology by Dugdale in 1967, in analogy with chemical reaction kinetics. Later it has been argued that only the most limiting process (photosynthesis or nutrient uptake) should determine the growth rate, allowing for switching between the two types of limitation depending on circumstances $(V_m \min(\mu_P, \mu_N))$. Most formulations of zooplankton grazing $h(P)$ show a saturating response to increasing food but, they may also include grazing thresholds, varying degrees of nonlinearity, and acclimation of the grazing rate to changing food conditions. This non linear coupling between Z e P is a strong determinant of the dynamics displayed by the NPZ model. The death or loss terms of the phytoplankton $i(P)$, and zooplankton $j(Z)$, are the “closure” terms of the

model. These transfer functions allow nutrients to be recycled back to the dissolved pool, potentially to be taken up again during photosynthesis. While phytoplankton death is almost always modelled as a linear process (Murray and Parslow, 1999), zooplankton death is sometimes more complicated. Including a nonlinear death rate usually implies a density-dependent loss rate – higher death rates at higher zooplankton densities. While there is little field evidence supporting the use of such functional form, the use of a density-dependent loss rate has significant implications for the model behaviour (Ohman and Hirche, 2001). Under quadratic zooplankton mortality, steady-state phytoplankton biomass increased with the nutrient loading until zooplankton grazing became saturated while phytoplankton biomass did not vary with nutrient loading under linear zooplankton mortality. This brief description of how are constructed NPZ model is to say that NPZ model dynamics call for careful field experimentation and analysis in order to develop criteria for choosing a particular model formulation.

3.3.1.1 *NPZD model*

In the LS configuration of the ROMS model, an extension of the NPZ model, the NPZD model have been used. The NPZD model consists of four compartments, one more than the NPZ model: nutrients, phytoplankton, zooplankton and detritus, interacting with each other. NPZD types model are all constructed on the same basis of NPZ model, that is an extension of the Lotka-Volterra prey-predator system of coupled non-linear differential equations. This means that the model considers several differential equations (one for each biological scalar variable) that are linked (partially or completely) through non-linear biological processes such as:

- *phytoplankton (P) growth rate* that consumes nutrient (N) is a source term in the phytoplankton equation and a loss term in the nutrient equation;
- *grazing of phytoplankton* by zooplankton (Z) is a loss term for the former, a source one for the later;
- *mortality of phytoplankton and zooplankton* and *zooplankton excretion* feeds the detritus (D) compartment;
- *nutrient regeneration* (also called remineralisation) is the transformation of detrital organic matter in elementary material.

This six essential processes for planktonic ecosystem dynamics can be used in a NPZD model (in this formulation without coupling with 3D circulation model):

$$\frac{dP}{dt} = +\text{PhytoGrowth} - \text{ZooGrazing} - \text{PhytoMortality}$$

$$\frac{dZ}{dt} = +\text{ZooGrazing} - \text{ZooExcretion} - \text{ZooMortality}$$

$$\frac{dN}{dt} = +\text{NutrientRgeneration} - \text{PhytoGrowth}$$

$$\frac{dD}{dt} = +\text{PhytoMortality} + \text{ZooExcretion} + \text{ZooMortality} - \text{NutrientRgeneration}$$

In such model, biological processes drive exchange of matter between variables that must be all calculated in the same units (generally Nitrogen in NPZD model). The total amount of Nitrogen (N+P+Z+D) is conserved.

$$\frac{dN_{TOT}}{dt} = \frac{d(N + P + Z + D)}{dt} = \frac{dP}{dt} + \frac{dN}{dt} + \frac{dZ}{dt} + \frac{dD}{dt} = 0$$

The same concept is used in 3D circulation framework except that these equations describe the local time derivative. Such models can be enriched through the inclusion of more than one phytoplankton, nutrient, zooplankton and detritus compartment. Only simple models with linear biological function can be analytically solved. These are not efficient for “realistic” plankton modelling that implies strong and non-linear inter-

dependency between variable. For example, Phytoplankton growth rate depends on light while phytoplankton is itself a factor of light attenuation.

3.3.2 *Biological Dynamics in NPZD model*

In this section the formulations used in the biological routine with the modifications done in this work of thesis have been described.

3.3.2.1 *Phytoplankton growth rate*

The formulation for phytoplankton growth rate is written as:

$$\text{PhytoplanktonGrowth} = \mu^P \cdot P$$

with

$$\mu^P = V^P \cdot \text{lim}(PAR) \cdot \text{lim}(N)$$

where V^P is a maximum potential growth rate and $\text{Lim}(PAR)$ and $\text{Lim}(N)$ are non-dimensional limitation terms (ranging from 0 to 1) for light (PAR) and nutrients (N), that are assumed to act in a multiplicative form. Phytoplankton growth rate is forced by PAR (Photosynthetically Available Radiation), *temperature* and *nutrient*. PAR is calculated at each time step by linearly interpolating forcing values. The PAR is calculated using the following formulation:

$$PAR = PAR_0 \cdot \exp(k_{water} + k_{chla} \cdot \theta \cdot r_{C/N,phyto} \cdot [P] \cdot \Delta z)$$

where PAR_0 is the surface PAR , k_{water} and k_{chla} are attenuation coefficients for pure water and chlorophyll, θ is the chlorophyll/carbon ratio, $r_{C/N,phyto}$ is the C/N ratio for phytoplankton, $[P]$ is phytoplankton concentration, and Δz is the depth step. Since the chlorophyll concentrations vary spatially, the attenuation coefficients will also do so. PAR_0 is a fraction (0.43) of the short wave radiation forcing used in the physical model for the heat budget of the surface layer: $PAR_0 = 0.43(\text{srflux} \cdot \rho_0 \cdot C_p)$ in the ROMS biological routines.

The temperature dependent growth rate, V^P , is parameterized using the relationship of Eppley (1972):

$$V^P(T) = \ln 2 \cdot 0.851 \cdot (1.066)^T$$

where T is given in degree Celsius and the units is d^{-1} . The term $Lim(N)$ is defined through a Michaelis-Menten type formulation (growth or assimilation increase as the substrate (N) increase up to an asymptotic “plateau”). Assuming only nutrient limitation, the phytoplankton growth rate is well described with:

$$\mu^P = V^P \left[\frac{N}{N + K_N} \right]$$

where K_N is the substrate concentration for which $\mu^P = 1/2V^P$ so called the half saturation constant.

The phytoplankton growth rate limitation by PAR and temperature is given by:

$$\mu^P = V^P \left[\frac{PAR \cdot \alpha \cdot \theta}{\sqrt{V_p^2 + (\alpha \cdot PAR \cdot \theta)^2}} \right]$$

where α (gC gChla-1 (W m⁻²)-1 d) is the initial slope of photosynthesis-irradiance (P-I) curve, θ is the Chla/C mass ratio, PAR is the amount of photosynthetic available radiation and V_p is the light-saturated growth. Photosynthesis, and hence phytoplankton growth, increase with light up to some saturation light levels above which it reaches a maximum value.

3.3.2.2 *Grazing, zooplankton growth and excretion*

The grazing term define the consumption of phytoplankton by zooplankton. It is the main food step of the oceanic food web. The grazing of zooplankton is described by a modified Ivlev function (Franks et al., 1986):

$$Z_{grazing} = g_{\max} \cdot P \cdot iv_p \cdot \left(1 - e^{(-iv_p \cdot P)} \right) \cdot Z$$

where g_{\max} is the zooplankton maximum grazing rate (d^{-1}), P is phytoplankton concentration, iv_p is the Ivlev parameter of zooplankton grazing. In contrast to the classical Ivlev function, this formulation shows a non-saturating response of the grazing rate for high prey levels. Its use permits to dampen predator/prey oscillations (e.g., Franks et al., 1986), and thus can provide stability to the planktonic ecosystem model forced by a highly changing physical environment. The term $Z_{grazing}$ feeds the zooplankton variable but not completely as the model considers that only a fraction of the ingested food benefits to the organisms. Hence a parameter of assimilation efficiency ($\beta = 0.75$) that define the fraction of ingested food leading to zooplankton growth. The remainder ($1-\beta$) benefits to the detritus compartment (production of fecal pellets). In addition zooplankton excretes a small amount of their biomass through metabolism that feeds the nutrient compartment. This simple linear term $-\mu_E^Z \cdot Z$ of zooplankton biomass appears as a source in the nutrient equation.

3.3.2.3 *Regeneration and the nutrient and detritus equations*

The nutrient regeneration is a simple linear function of detritus:

$$NutrientRgeneration = \mu_D^N \cdot D$$

with a constant rate of detritus remineralization. This is a source term for nutrient and a loss one for detritus.

The two equation are:

$$\frac{\partial N}{\partial t} = +\mu_D^N D + \mu_E^Z Z - \mu^P P$$

$$\frac{\partial D}{\partial t} = +(1-\beta) \cdot g_{\max} \cdot \left(\frac{P}{P+K_p} \right) \cdot Z + m^Z Z^2 + m^P P - \mu_D^N D$$

3.3.2.4 *Sedimentation of phytoplankton and detritus*

In addition to these biological terms, we may consider the sinking terms for phytoplankton and detritus since the dead particulate matter tend to sink in the water column at high speed ($O(10-100 \text{ m d}^{-1})$). Some species of phytoplankton, mainly diatoms that are “large” cells embedded in a mineral test, may also sink but at slower rate ($O(0-5 \text{ m d}^{-1})$) or aggregate with the detritus pool. This sinking of organic matter is the preferential way out in the *biological pump*. The assimilation of inorganic carbon by phytoplankton during photosynthesis, followed by a long time sequestration of a fraction of this organic matter at depth (through sedimentation), make the ocean a sink term source for atmospheric CO_2 . The justification of these sedimentation is not purely geochemical, as slow sinking of living phytoplankton cells and the export of organic matter may affect phytoplankton dynamics and the regeneration processes, hence the functioning of the ecosystem.

The sedimentation processes are:

$$\text{Phytoplankton Sedimentation} = -w^P \cdot \frac{\partial P}{\partial z}$$

$$\text{Detritus Sedimentation} = -w^D \cdot \frac{\partial D}{\partial z}$$

3.3.2.5 *Phytoplankton, Zooplankton, Nutrient and Detritus full equations*

The phytoplankton mortality is a simple linear term of phytoplankton biomass:

$$\text{Phytoplankton Mortality} = m^P \cdot P$$

A constant small fraction of phytoplankton cells dead at each time and enter the detrital compartment.

The zooplankton mortality is:

$$\text{ZooplanktonMortality} = m^Z \cdot Z^2$$

The use of such quadratic term impedes the occurrence of predator-prey oscillation that can be generated by the use of a linear term.

Phytoplankton, Zooplankton, Nutrient and Detritus biological dynamics equations are:

$$\frac{dP}{dt} = +\mu^P \cdot P - g_{\max} \cdot \left(\frac{P}{P + K_p} \right) \cdot Z - m^P P$$

$$\frac{dZ}{dt} = +\beta \cdot g_{\max} \cdot \left(\frac{P}{P + K_p} \right) \cdot Z - \mu_E^Z D - m^Z Z^2$$

$$\frac{dN}{dt} = +\mu_D^N D + \mu_E^Z Z - \mu^P P$$

$$\frac{dD}{dt} = +(1 - \beta) \cdot g_{\max} \cdot \left(\frac{P}{P + K_p} \right) \cdot Z + m^Z Z^2 + m^P P - \mu_D^N D$$

3.4 Improvement of the biogeochemistry and the regional biogeochemistry of the model

Additional changes to the classical schemes proposed in the UCLA-IRD ROMS and associated NPZD packages have been done to improve the regional dynamics and biogeochemistry and to achieve the aims of the work. In this section the additional changes have been described.

The main food step of the oceanic food web is the consumption of phytoplankton by zooplankton. In the classical scheme, the grazing of zooplankton is described by a Michaelis-Menten type of formulation where the growth increase as the substrate increase until to an asymptotic “plateau”. The Michaelis-Menten formulation is:

$$Z_{\text{grazing}} = g_{\max} \cdot \left(\frac{P}{P + K_p} \right) \cdot Z$$

where g_{\max} is the zooplankton maximum grazing rate, P is phytoplankton concentration and K_P the half-saturation constant of the kinetic.

With this formulation the model output showed oscillations (predator/prey oscillations).

In the configuration used in this work, to avoid the predator/prey oscillations and to improve the biogeochemistry of the model, we changed the function of grazing of zooplankton. The modified Ivlev function (Franks et al., 1986) have been introduced in the biogeochemical model:

$$Z_{\text{grazing}} = g_{\max} \cdot P \cdot i\nu_p \cdot \left(1 - e^{(-i\nu_p \cdot P)}\right) \cdot Z$$

where g_{\max} is the zooplankton maximum grazing rate, P is phytoplankton concentration, $i\nu_p$ is the Ivlev parameter of zooplankton grazing. This formulation shows a non-saturating response of the grazing rate for high prey levels. Its use permits to dampen predator/prey oscillations (e.g., Franks et al., 1986), and thus can provide stability to the planktonic ecosystem model forced by a highly changing physical environment.

To improve the regional biogeochemistry of the model, the nutrients forcing files have been collected from DYFAMED data base (site: <http://www.obs-vlfr.fr/dyfBase/>). The DYFAMED station is located in the Ligurian Sea (section 4.3).

In the classical schemes proposed in the UCLA-IRD ROMS & associated NPZD packages, nitrates data are from WOA2005 climatology. The spatial resolution of nitrate from WOA dataset, is 1° and the temporal resolution is seasonally in the first 500 m of depth while, after 500 m, it is annually. Besides the resolutions, the temporal evolution of nitrates from WOA do not appropriately fit the regional biogeochemistry and its seasonal evolution.

For these main reasons, nitrate data, from DYFAMED data base, have been collected from 1991 to 2007. The temporal resolution of the nitrate data is

monthly and they are distributed in the first 2000 m of depth (about 30 sampling stations along the 2000 m). The data have been checked and the months of each year (from 1991 to 2007) have been averaged in order to have a “DYFAMED monthly climatology” for a typical seasonal evolution of nitrate in the Ligurian Sea. This data have been used as initial and boundary condition for the LS-ROMS model making substantially an error of positioning since the nitrate collected at the DYFAMED station have been positioned at the boundary of the LS-ROMS model.

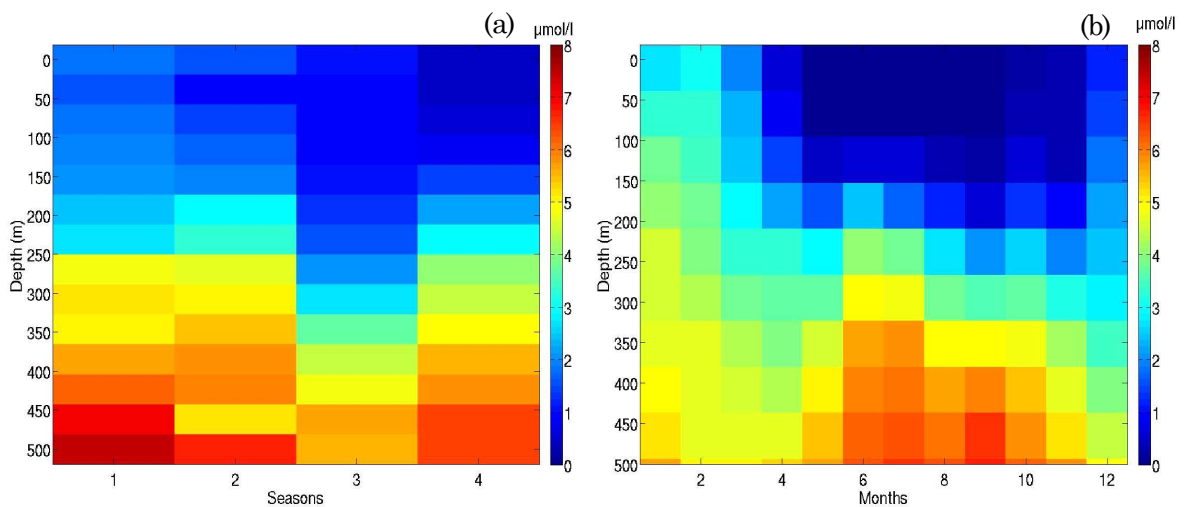


Fig. 3.4.1 Seasonal evolution of nitrate ($\mu\text{mol l}^{-1}$) in the first 500 m of depth from (a) WOA2005 and (b) DYFAMED datasets in the study region.

Figure 3.4.1 shows the seasonal evolution of nitrate on the first 500 m of depth from (a) WOA and (b) DYFAMED datasets in the study region. Figure 3.4.1a shows a low concentration of nitrate in the first surface layers at the begin of the year. During winter mixing the surface layers become rich of nutrients as it is showed in figure 3.4.1b. Figure 3.4.2 shows the distribution along the vertical (2000 m) of nitrate from DYFAMED dataset. It shows a typical Ligurian sea seasonal evolution of nitrate. There is i) high nitrate concentration variability in the first 500 m of depth during the year; ii) a higher surface concentration of nitrate during the winter mixing; and iii) a

low surface concentration during the stratified period. Under the depth of 500 m, the concentration is nearly constant.

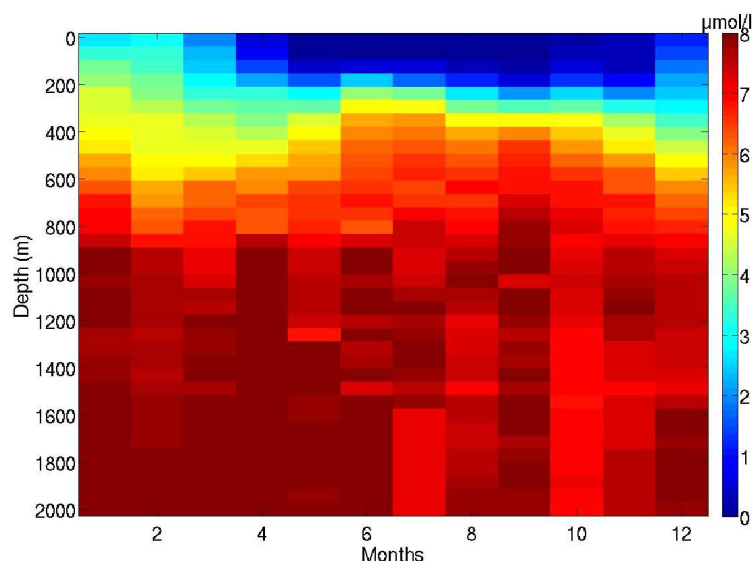


Fig. 3.4.2 Seasonal evolution of nitrate ($\mu\text{mol l}^{-1}$) in 2000 of depth from DYFAMED dataset.

Figure 3.4.3 shows the yearly mean vertical distribution of nitrate in the 2000 of depth. The slope of nitracline is the main difference between the profiles. The WOA yearly nitracline has a steep slope while the DYFAMED yearly nitracline shows the typical regional vertical distribution with a gentle slope.

An aim of the thesis is to study and to estimate the primary production of the Ligurian Sea. To know primary production allows to understand the energy that feed the biological system, therefore, the energy available for the whole food chain. The primary production term is also an index of the available energy for top-predators (e.g. marine mammals). To achieve this aim and to improve the biogeochemistry of the model, the daily integrated production has been calculated.

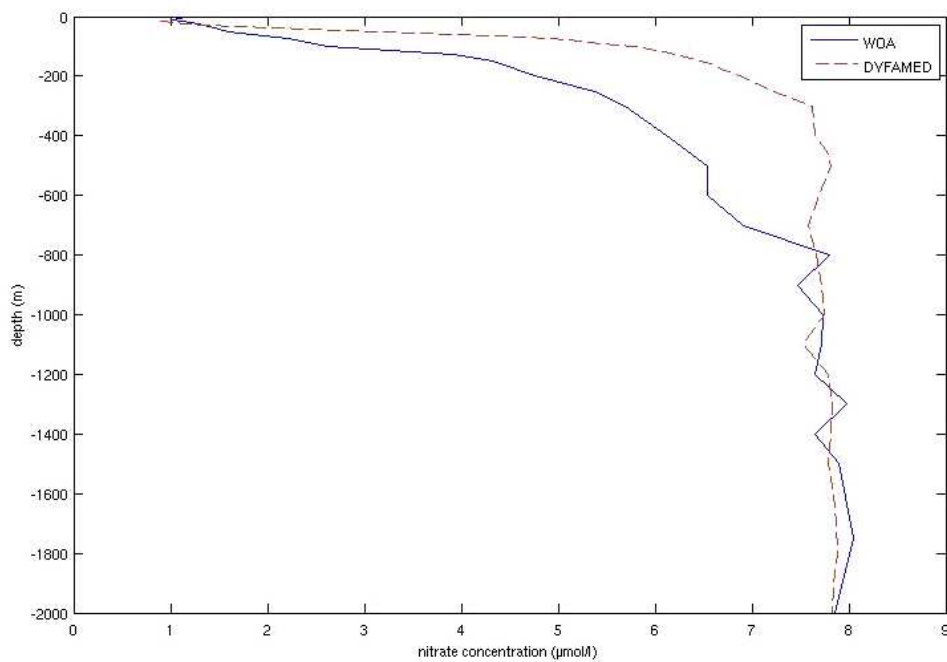


Fig. 3.4.3 Year vertical distribution of nitrate ($\mu\text{mol l}^{-1}$) in the 2000 m of depth from WOA2005 (line) and DYFAMED (dotted-line) datasets in the study region.

The primary production term, defined as $Primary\ Production = \mu^P \cdot P$, has been added into the biological code and it has been integrated on 24 h. This term allows to detect new production area, where production is due to the presence of the limiting factor (e.g. nutrients).

In conclusion, the additional changes to the classical schemes proposed in the UCLA-IRD ROMS and associated NPZD packages described in this section, are related to the grazing term of zooplankton, to the input file (nutrients), to the primary production term and to the parameters explained in table 4.7.1 (section 4.7).

3.5 NPZD model coupled with ROMS model

The NPZD model is coupled to the physical model through the advection-diffusion equation. Each state variable of the NPZD model will have a separate equation describing its motion in space and time.

The partial differential equation used to compute the evolution of the simulated tracers (N, P, Z, D), here C, is of the form:

$$\frac{\partial C}{\partial t} + u \frac{\partial C}{\partial x} + v \frac{\partial C}{\partial y} + (w + w_s) \frac{\partial C}{\partial z} = \frac{\partial}{\partial x} \left(K_x \frac{\partial C}{\partial x} \right) + \frac{\partial}{\partial y} \left(K_y \frac{\partial C}{\partial y} \right) + \frac{\partial}{\partial z} \left(K_z \frac{\partial C}{\partial z} \right) + \text{BioDinamis}$$

where C is the concentration of the state variable (N, P, Z, D), u , v and w are the horizontal and vertical water velocities determined by the physical model, w_s is the vertical swimming or sinking speed of the state variable, and K_x , K_y and K_z are the horizontal and vertical eddy diffusivities. At each time step, the transport of each biological variable is performed by the advection-diffusion routine of the physical model while the biological dynamics is computed afterwards in the biological routine.

4 Results

4.1 Description of the main simulations

To achieve the aims of the work (chap. 1) 10 main simulations have been done (Tab. 4.1.1). The simulations are divided into 2 main categories: climatology and interannual. Climatology simulations describe a typical year evolution of the model variables since the input data come from climatological dataset described in section 4.3 while interannual simulations describe a particular year. We have chosen 2006 due to the availability of input data, which come mainly from operational models, and measured data, used to validate the model output. In the first part of the work, climatology simulations using climatological datasets as input data have been done. Climatology simulations have been carried out to understand the model ability to simulate proper spatial and temporal evolution of the model variables and the general processes of the study area. In order to analyse the effect of wind variability, in the second part of the work, interannual simulations have been forced with higher spatial and temporal resolution wind forcing showing a richer small-scale dynamics. The configuration of the simulations presented in table 4.1.1 also indicate different output resolutions. As expected, the increase of resolution allows to detect more structures and processes (section 4.5). All of these simulations have been used to understand the ability of the model, with different forcing, to simulate the Ligurian Sea hydrodynamic and mesoscale processes. The interest is to study mesoscale structures and the processes linked to them (upwelling, downwelling). These in turn influence biological processes linked to the plankton dynamic. To understand these processes, we use the NPZD biogeochemical model coupled to the LS-ROMS climatological and interannual simulations.

Runs		Atmospheric Forcing Spatial and Temporal Resolution	Marine Boundary Condition Spatial and Temporal Resolution	Output Spatial Resolution	Model Temporal Resolution	Output Temporal Resolution	Simul. Years	Bio Mod	Zoom
1	Climatology	COADS; 1/2°; 1 month.	WOA; 1°; 1 month.	1/16°	1080 sec	60 h	10 y		
2	Climatology	COADS; 1/2°; 1 month.	WOA; 1°; 1 month.	1/32°	580 sec	24 h	10 y	x	
3	Climatology	COADS; 1/2°; 1 month.	MFSclim; 1/16°; 1 month.	1/16°	1080 sec	60 h	10 y		
4	Climatology	COADS; 1/2°; 1 month.	MFSclim; 1/16°; 1 month.	1/32°	580 sec	30 h	4 y		
5	Interannual	COADS; 1/2°; 1 month.	MFSclim; 1/16°; 10 days.	1/16°	1080 sec	60 h	1 y		
6	Interannual	COADS; 1/2°; 1 day(interp).	MFS2006 1/16°; 1 day.	1/16°	1080 sec	60 h	1 y		
7	Interannual	COADS; 1/2°; 1 day(interp).	MFS2006 1/16°; 1 day.	1/32°	580 sec	24 h	1 y	x	
8	Interannual	LAMI2006 1/16° + COADS 1/2°; 1day.	MFS2006 1/16°; 1 day.	1/16°	1080 sec	60 h	1 y		
9	Interannual	LAMI2006 1/16° + COADS 1/2°; 1day.	MFS2006 1/16°; 1 day.	1/32°	580 sec	24 h	1 y	x	~1 Km
10	Interannual	LAMI2006 1/16° + COADS 1/2°; 1day.	MFS2006 1/16°; 1 day.	1/64°	135 sec	24 h	1 y		~300 m

Tab. 4.1.1 Configuration of the main simulations.

4.2 Model configuration

To study the mesoscale processes of the Ligurian Sea we use the ROMS model for a domain covering the Ligurian Sea. The model domain comprises the northwestern part of the Mediterranean Sea, from 42.5° N to 44.5° N and from 6.5° E to 11.1° E. The bottom topography is based on the global topography dataset at 2' resolution (Smith and Sandwell, 1997). The resulting topography is shown in figure 4.2.1 which displays the major features of the domain including the North part of Corsica and the Elba island. In this model version (Ligurian Sea configuration, LS-ROMS) there are three open lateral boundaries; at 42.5° N, 6.5° E and 11.1° E. The LS-

ROMS model has been configured, for the main simulations, with a horizontal resolution of $1/32^\circ$. At this resolution, the Rossby radius of deformation (5-12 km in the whole Mediterranean and for different seasons, Grilli and Pinardi, 1998) is resolved and consequently the configuration is adequate to simulate mesoscale structures. The grid has 32 vertical levels with vertical refinement near the surface for a reasonable representation of the surface, the euphotic layer.

To better understand mesoscale processes, we apply the one-way LS-ROMS embedding procedure to a small coastal area of the Ligurian Sea where mesoscale processes are simulated. The domain of the child grid is located in the northwestern part of the study region and it extends from 6.8° E to 8.3° E and from 43° N to 44.1° N. The child grid is embedded in a one-way nesting within the parent grid: Information on the state of the model is passed from the parent to the child grid at each time step, while no back-transfer from the child grid to the parent model occurs. Both grids have 32 vertical levels.

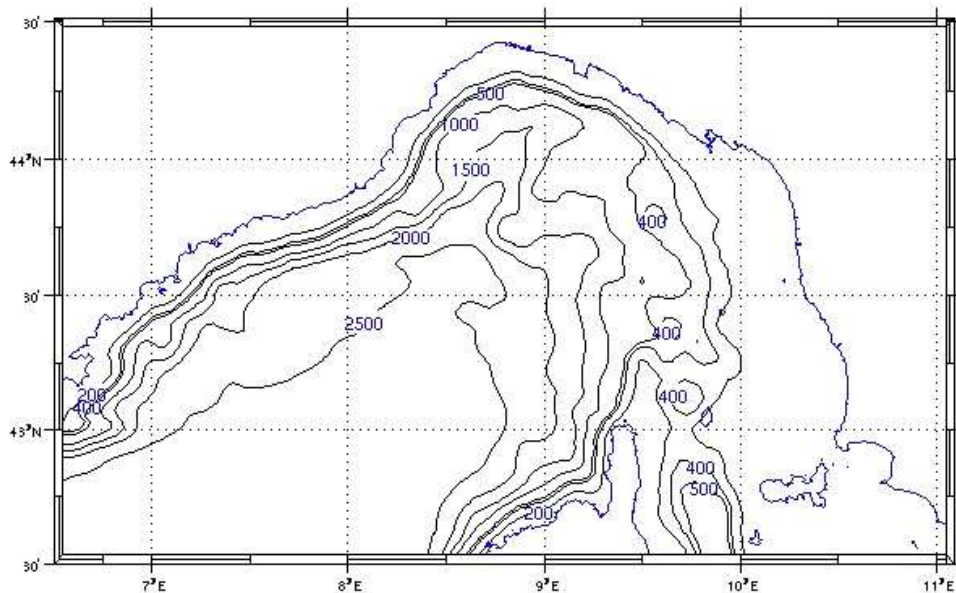


Fig. 4.2.1 The Ligurian Sea model domain and bottom topography based on the global topography dataset at $2'$ resolution (Smith and Sandwell, 1997).

4.3 Initial and boundary conditions

Along the open sea boundaries and for initial conditions, the LS-ROMS configurations of the model are forced with temperature and salinity obtained from WOA2005 and MFS datasets. WOA2005, World Ocean Atlas, is a set of objectively analyzed (1° grid) climatological fields of in situ temperature, salinity, phosphate, silicate, nitrate and other parameters at standard depth levels for annual, seasonal, and monthly compositing periods for the World Ocean from the national oceanographic data centre (NOAA, USA). MFS, the Mediterranean Forecasting System, is an operational model of the Mediterranean Sea. The horizontal spatial output resolution is $1/16^\circ$ and the temporal output resolution is daily. The code used in MFS is OPA (Ocean PARallelise), developed by Institut Pierre Simon Laplace, Laboratoire d’Oceanographie DYnamic et de Climatologie (LODYC), Paris. The OPA model is a primitive equation model which solves the Navier-Stokes equations in the approximation of thin-shell, Boussinesq, hydrostatic and incompressible fluid (Madec et al., 1998). With regard to MFS, the LS-ROMS model is forced with a MFS climatology or MFS 2006 dataset, depending on the simulation. MFS climatology is a climatology from the MFS model while MFS 2006 is the output dataset of the MFS model for the year 2006.

At the surface the LS-ROMS model is forced using monthly-mean climatologies of wind stress and fluxes of heat and freshwater derived from the Comprehensive Ocean-Atmosphere Data Set, COADS (da Silva et al., 1994) and/or wind stress data from the Limited Area Model Italy, (COSMO-I7). COADS contains the global surface fluxes climatology at $1/2^\circ$ spatial resolution and 1 month temporal resolution. COSMO-I7, a non-hydrostatic and fully compressible numerical weather prediction model, is the Italian version of the COSMO Model with horizontal resolution $1/16^\circ$ and temporal resolution 3 hours (Steppeler et. al., 2003). As wind forcing for the LS-

ROMS version of ROMS model, the wind data from COSMO-I7 dataset have been used to calculate the daily wind stress necessary to force the model.

As regard the field on the two models (ocean and atmosphere) used to force the regional simulation, ANNEX1 and ANNEX2 show a comparison between fields from different datasets.

ANNEX 1 shows a comparison between the wind stress intensity and direction from COADS and COSMO-I7(LAMI) datasets interpolated on the ROMS grid. The temporal resolution of COADS dataset is monthly and the 12 figures of COADS (showed in ANNEX 1) show the wind stress for each month. The temporal resolution of COSMO-I7 dataset is three hours. The 12 figures of COSMO-I7(LAMI) show the monthly mean of wind stress of each month. ANNEX 1 shows that the wind stress from COSMO-I7 has a greater spatial variability and a higher intensity than wind stress from COADS dataset. It is also possible to see the monthly variability of the two datasets. Wind stress from COSMO-I7 dataset has also a greater monthly variability. From ANNEX 1 is not possible to see the daily variability of COSMO-I7 since the data are monthly averaged. Besides the differences in the temporal resolution, also the native spatial resolution of the two dataset need to be remarked. The spatial resolution of the COADS dataset is $1/2^\circ$ while the spatial resolution of the COSMO-I7 (LAMI) dataset is $1/16^\circ$.

ANNEX 2 shows the surface temperature field from WOA and MFS datasets interpolated on the ROMS grid. The temporal resolution of WOA dataset is monthly and the 12 figures of WOA (showed in ANNEX 2) show the surface temperature for each month. The temporal resolution of MFS dataset is daily. The 12 figures of MFS show the monthly mean of surface temperature of each month. There are several differences between the surface temperature of the two datasets. The space variability, the value range and the temporal variability of the field are the main differences. ANNEX 2 shows that the space and monthly variability of the field is greater for the MFS dataset and the range of surface temperature value is larger for the

MFS dataset. Besides the differences in the temporal resolution, also the native spatial resolution of the two dataset need to be remarked. The spatial resolution of the WOA dataset is 1° while the spatial resolution of the MFS dataset is $1/16^\circ$.

As regards boundaries and initial conditions for the NPZD model, the model needs input nitrate, chlorophyll, phytoplankton and zooplankton data. The global SeaWIFS chlorophyll climatology and measured *in situ* data of nitrate have been used to force the NPZD model. Nitrate input data (section 3.4) come from measured data at the DYFAMED (from the program “Dynamics of atmospheric fluxes in the Mediterranean Sea” part of the France-Joint Global Ocean Flux Study) station which provides a rich dataset of biological, geochemical, and physical parameters. The DYFAMED site is located 52 km off Cape Ferrat, at $43^\circ 25'N$, $07^\circ 52'E$ in the Ligurian Sea and has a water depth of 2350m. To force the model, nitrate and nitrite data (NO_3^- and NO_2^-) monthly mean from 1991 to 2007 have been used. SeaWIFS is a surface chlorophyll-a climatology dataset based on SeaWIFS observations. The extrapolation of chlorophyll data on the Ligurian Sea region have been done. From this surface values, the chlorophyll is extrapolate on vertical levels using Morel and Berthon (1989) parameterization. Phytoplankton and zooplankton input data have been calculated from the chlorophyll concentration. In the NPZD model the ratio mgC/mgChla is fixed at 50. To have the phytoplankton concentration for the input data, we use this fixed ratio and the Redfield ratio (106molC/16molN) to obtain a parameter ($\theta=0.6289$) to estimate the phytoplankton concentration from the chlorophyll concentration. Since the LS-ROMS model has not the same horizontal and vertical resolution as the MFS, WOA, COADS, COSMO-I7, SeaWIFS or DYFAMED datasets, a horizontal and vertical linear interpolation of each dataset field is necessary.

4.4 Comparison between climatological and interannual simulations

In this chapter a climatology simulation and its comparison with an interannual simulation is presented.

The model configurations are summarized in table 4.1.1. The climatological configuration into the row “Run 2” of the table 4.1.1 corresponds to the simulation described in this section. Along the open sea boundaries and for initial conditions, the LS-ROMS configuration of the model is forced with temperature and salinity obtained from WOA dataset while at the surface it is forced using monthly-mean climatologies of wind stress and fluxes of heat and freshwater derived from COADS dataset. The climatological year presented is the tenth year of the simulation. The spin-up phase involve the first 3 years. This simulation allows to observe the main hydrodynamic processes of the Ligurian Sea.

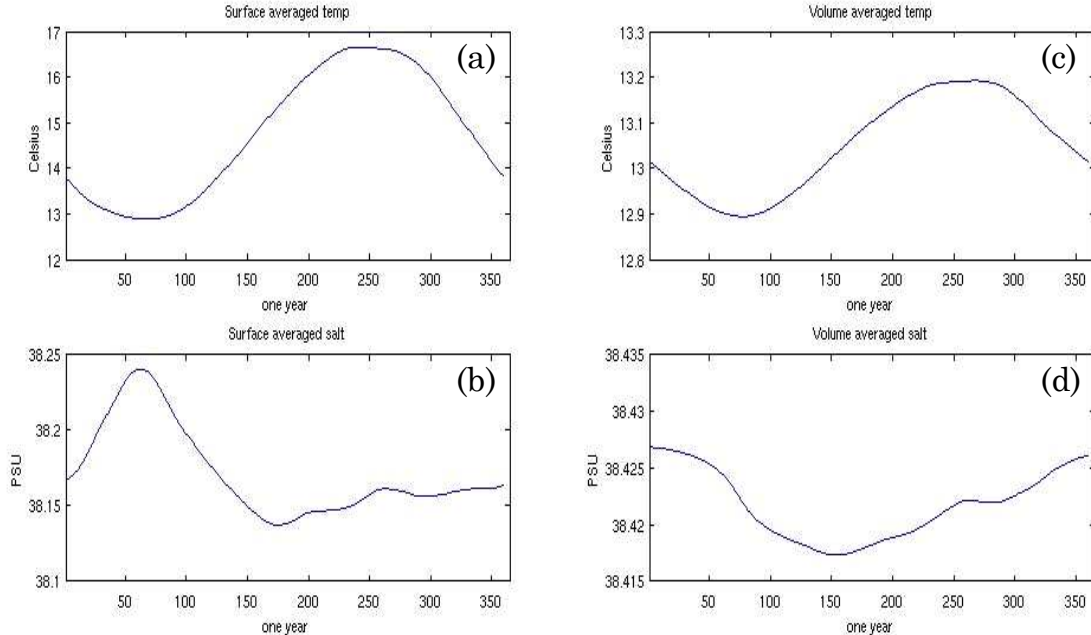


Fig. 4.4.1 Temporal variability of temperature and salinity of the Ligurian Sea simulation averaged (a,b) in the first layers (100m) and (c,d) in the volume.

Figures 4.4.1 shows the seasonal variability of the physical parameters (temperature and salinity). The variables are averaged in the first 100m depth (fig. 4.4.1a,b) and in the whole volume (fig. 4.4.1c,d). In the first layers (100m) the temperature is low (about 13°C) during the first 3 months of the year, then it increase as far as August when it reaches 16.8°C. A similar qualitative evolution occurs in the whole volume (fig. 4.4.1c). The model reproduces the seasonal variability of the Ligurian Sea. In the following part of the section, the LS-ROMS climatology model results for a typical summer (July), autumn (November), winter (February) and spring (May) month, monthly mean, will be analyzed. During July (fig. 4.4.2) the model domain is characterized by a well-defined large-scale cyclonic circulation at least up to 400 m depth. The Ligurian Sea current is fed by the eastern Corsica Current and the western Corsica Current coming from the eastern and the western side of Corsica, respectively and it flows along the continental slope of the Liguria. The Levantine Intermediate Water and Western Mediterranean Deep Water, possibly constrained by the bottom topography, follow the cyclonic path. During November (fig. 4.4.2) the large-scale cyclonic circulation is basically the same as in August but, in this case, it is significant the presence of few mesoscale eddies along the Ligurian current and in the centre of the cyclonic system. In February, the large-scale cyclonic circulation appears relatively less coherent than in the previous months. During this month, the Ligurian current shows meanders and some eddies are displayed on its right side after the Corsica channel and on the left side after the Gulf of Genoa. Finally, during May, the western Corsica Current becomes relatively more intense than in February and November and, in this month, along the Ligurian current, some large gyres appear.

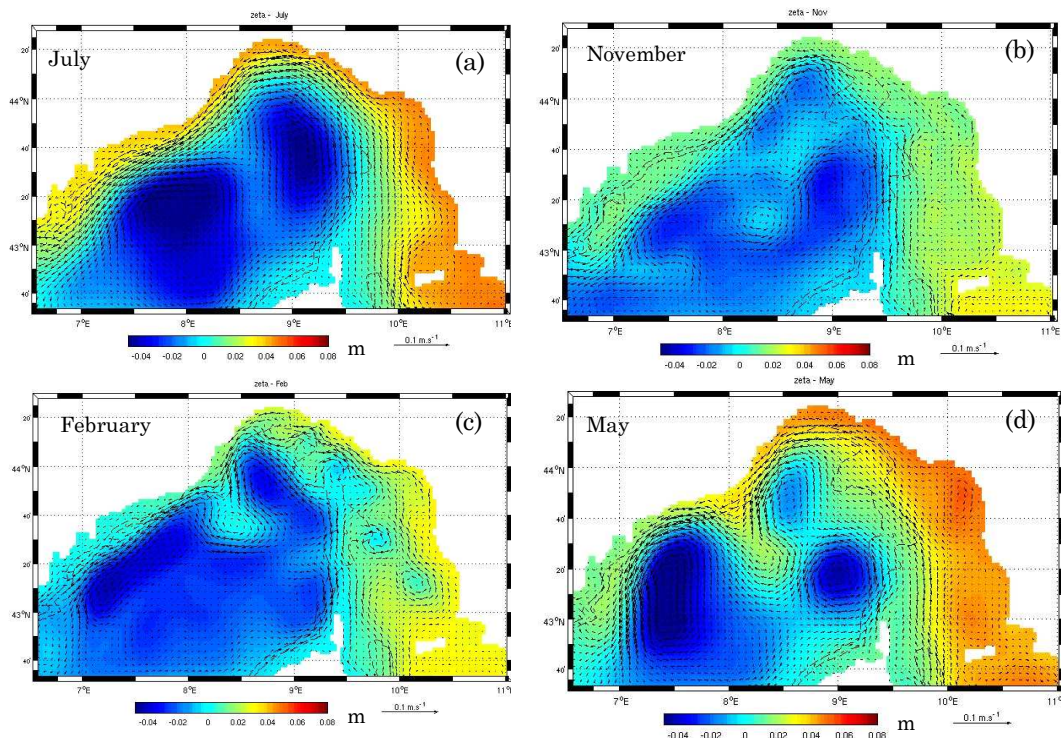


Fig. 4.4.2 Monthly averaged velocity field at the depth of 10 meters and distribution of SSH during (a) July, (b) November, (c) February and (d) May from the climatological experiment.

To detect mesoscale structures and their variability of a particular year an interannual simulation of the year 2006 have been done (Tab.4.1.1, Run 9). In this case the model is mainly forced by operational model output dataset: MFS at the open sea boundary and COSMO-I7 wind stress at the surface as described in section 4.3. The main differences between the output of the two simulations are the dynamic of the basin, the numbers and intensity of structures simulated, and the variability of the system.

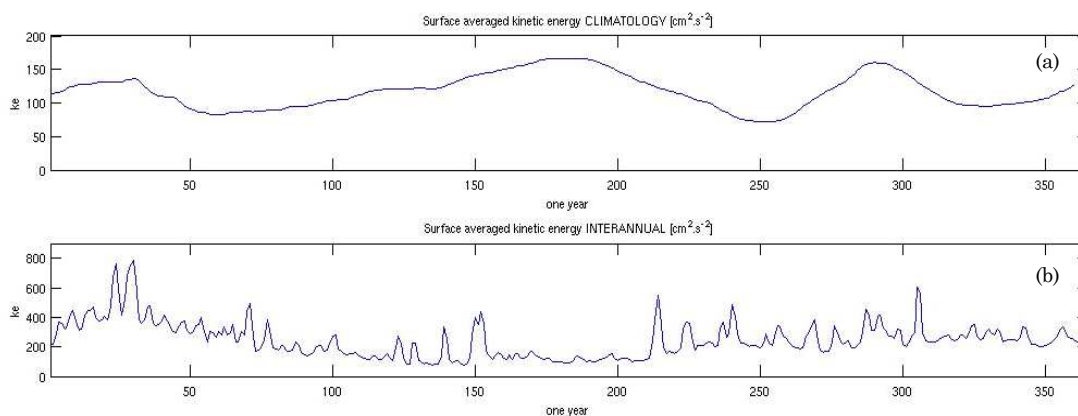


Fig. 4.4.3 Surface averaged Kinetic Energy during the tenth year of the climatological experiment (a) and during the year 2006 of the interannual experiment (b).

Figure 4.4.3 depicts the surface horizontal averaged kinetic energy of the climatology simulation (a) and the interannual simulation (b), showing a clear different behaviour. It is evident the different kinetic of the two runs. In the climatological experiment (Run 2), the evolution of the surface kinetic energy (4.4.3a) is smoothly and less dynamic than in the interannual simulation (Run 9) (figure 4.4.3b) where it reaches higher values and shows a marked dynamical evolution due to the different forcing. To observe the different dynamic and variability of the two simulation is useful to compare the transport simulated by the model into the Corsica Channel. The Corsica channel is an input of water and properties for the whole basin and is located, in the model, far enough from the sponge layer. Moreover, in the section 4.9, the simulated Corsica Channel transport is compared with measured in situ data.

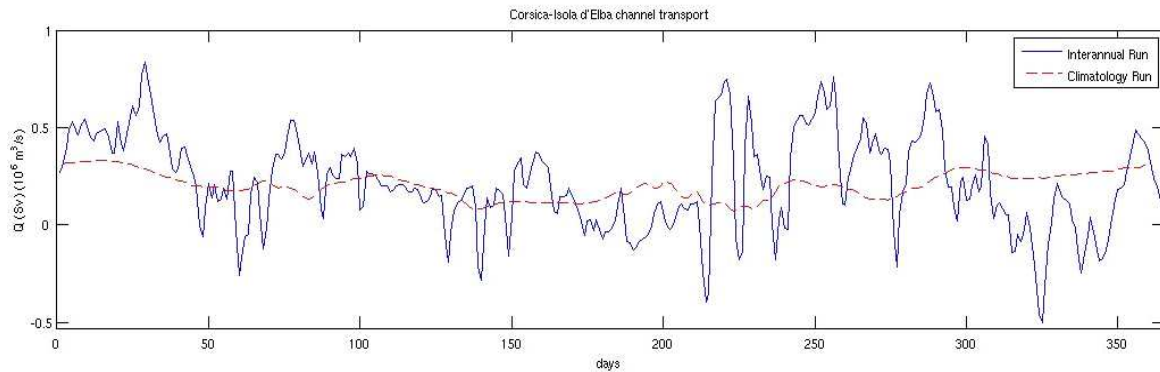


Fig. 4.4.4 Comparison between the transport simulated by the interannual simulation (year 2006) and by the climatological simulation into the Corsica channel.

Figure 4.4.4 shows the comparison between the transport (Sverdrup, $10^6 \text{ m}^3 \text{ s}^{-1}$) simulated by the interannual simulation (Run 9) and by the climatology simulation (Run 2). The daily variability of the input flow of water, showed in figure 4.4.4, is greater in the Run 9. The transport simulated by the Run 9 reaches values of 0.8 Sv during the more dynamical season while the Run 2 simulate lower values of transport which never reach 0.5 Sv. The transport simulated by the Run 2 shows a seasonal evolution less variable than the evolution of the transport of the Run 9. This is due to the different forcing data files. The different forcing cause also differences as regard the structures simulated. The Run 9 shows a large number of intense eddies which are not simulated in the climatology experiment (Run 2).

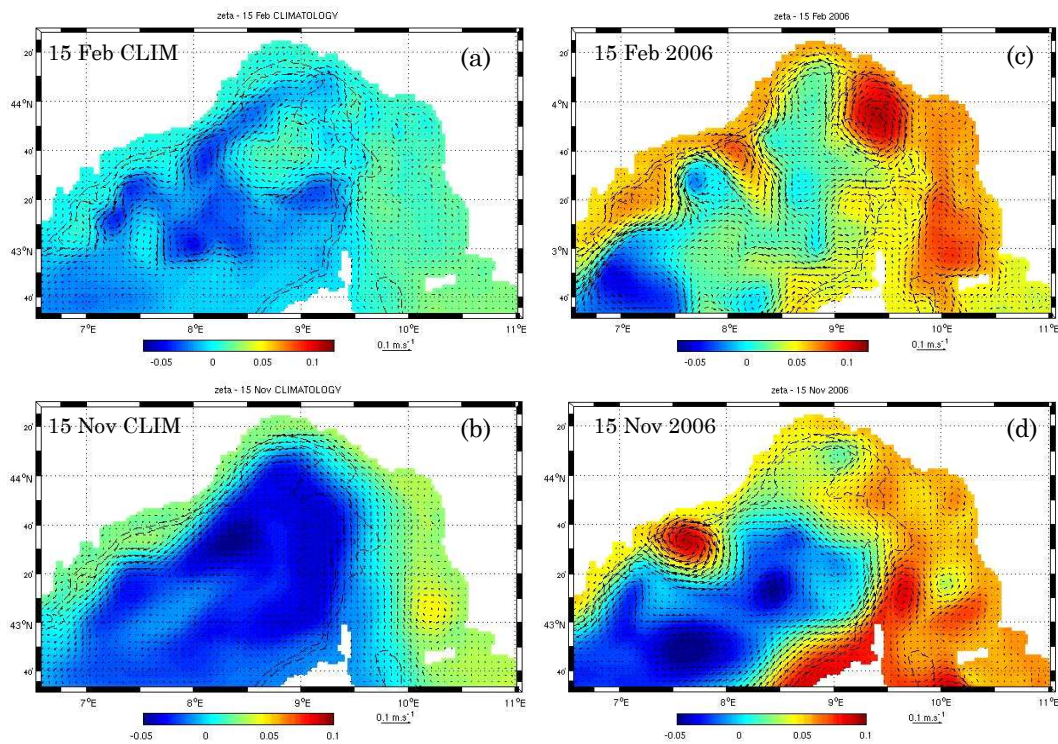


Fig. 4.4.5 Velocity field at the depth of 10 meters and distribution of SSH during 15 February and 15 November from (a,b) climatological and (c,d) interannual experiments.

Figures 4.4.5c,d show, during the high mesoscale activity period, a number of structures simulated by the interannual run (Run 9). They show the presence of cyclonic and anti-cyclonic eddies associated with meanders in the NC. Figure 4.4.5c shows a well marked anti-cyclonic eddy, along the NC, before the Gulf of Genoa, and a couple of anti-cyclonic and cyclonic eddies close to the Gulf of Nice, and meanders along the current. Figure 4.4.5d shows a less marked cyclonic and anti-cyclonic eddies after the Corsica channel and an intense coastal anti-cyclonic eddy off-shore Nice, and meanders along the current. The climatology experiment (figures 4.4.5a,b) shows a less prominent mesoscale activity. Moreover the interannual simulation (Run 9) has a marked daily variability, due to the daily variable forcing files (wind stress and marine boundary conditions).

CHAPTER 4: RESULTS

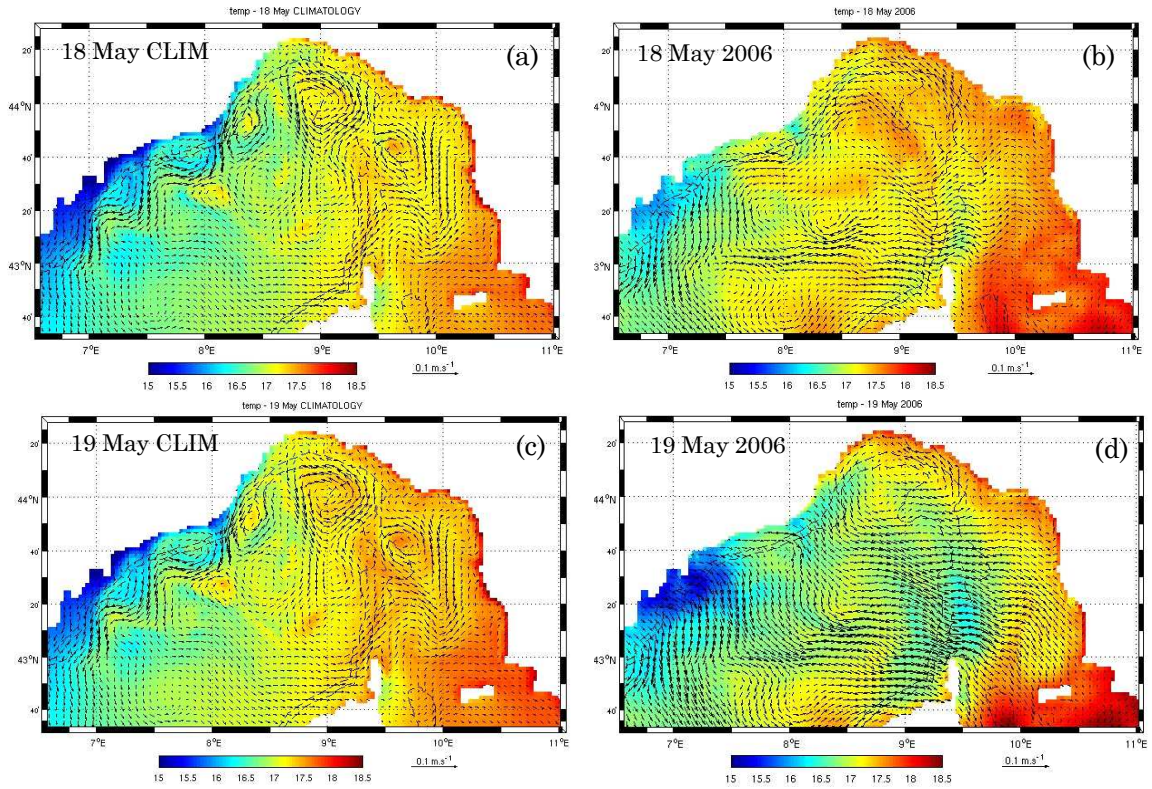


Fig. 4.4.6 Surface velocity field and horizontal distribution of SST (m) during 18 and 19 May from (a,c) climatological and (b,d) interannual experiments.

Figures 4.4.6a,c and 4.4.6b,d show an example of the daily variability of the climatological (Run 2) and interannual (Run 9) runs respectively. Figures 4.4.6 show the surface velocity field and horizontal distribution of SST in meters. The climatology experiment (figure 4.4.5a,c) shows two cyclonic eddies into the NE part of the domain and it simulates a NC with several meanders. The fields showed in figures 4.4.6a and 4.4.6c are similar, there is not a marked variability between the two figures since in the whole Run 2 there is not a noticeable variability between two following days. Figures 4.4.6b and 4.4.6d show an example of marked daily variability of the Run 9. This is due to the forcing data files which have mainly daily temporal resolution for the interannual simulation (Run 9). In the figure 4.4.6b, 18 May, the surface direction of currents is typical; there is not a strong mesoscale activity due to the spring period, the NC follows the Ligurian

CHAPTER 4: RESULTS

coast and the surface temperature is between 17-18°C. Comparing this picture with figure 4.4.6d, 19 May, the day after, the background is different. The main direction of surface current is off-shore, certainly due to the atmospheric forcing, and the distribution of surface temperature is changed. The SST is lower than the previous day and there is a minimum of temperature close to the coastline which coincide with an upwelling region.

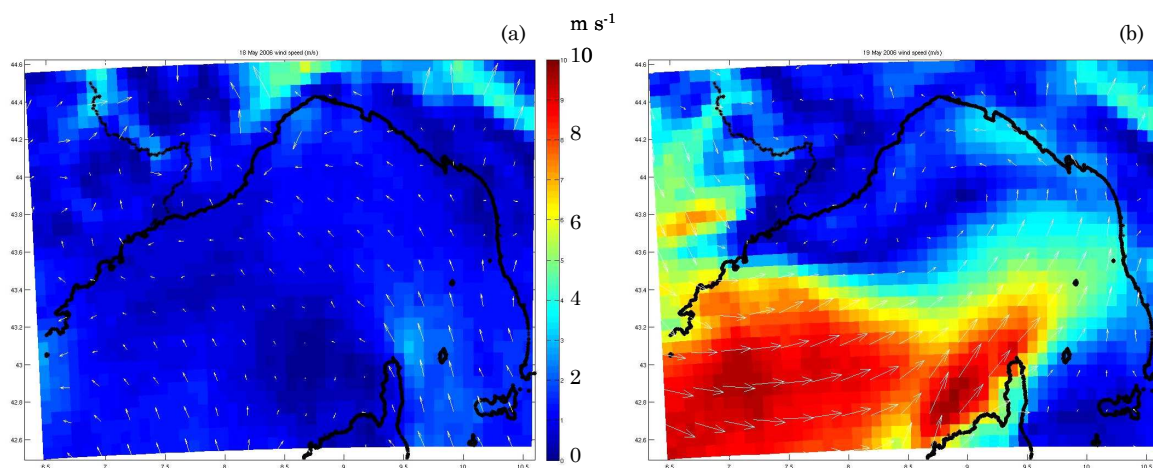


Fig. 4.4.7 Velocity field of wind (direction and speed) from COSMO-I7 dataset of (a) 18 May 2006 and (b) 19 May 2006.

Observing the wind speed distribution (figure 4.4.7) of the 18 and 19 May 2006 from the COSMO-I7 dataset, a marked daily variability is shown. The daily mean of wind speed on 18 May 2006, showed in figure 4.4.7a, is weaker than the one showed on 19 May 2006 (figure 4.4.7b) and the wind direction is different. On 18 May the mean wind speed on the study area is less than 10 km h⁻¹ while on 19 May it is about 40 km h⁻¹. The wind direction on 18 May is variable in space but the predominant wind direction is from S-SE while on 19 May the predominant wind direction is changed and is from SW. This improve of the wind intensity and the change of the wind direction has an impact on the flow dynamic showed in figure 4.4.6.

To compare the wind forcing of the two runs, on these two days figures 4.4.8a,b,c have been done. Figure 4.4.8 shows the different wind stresses

which force the simulations. Figure 4.4.8a shows the wind stress of the month of May from the monthly climatology COADS dataset. The wind stress is about 0.02 Nm^{-2} for the whole domain in the month of May. Figures 4.4.8b (18 May) and 4.4.8c (19 May) show the daily variation from 18 to 19 May of the wind stress coming from COSMO-I7 dataset.

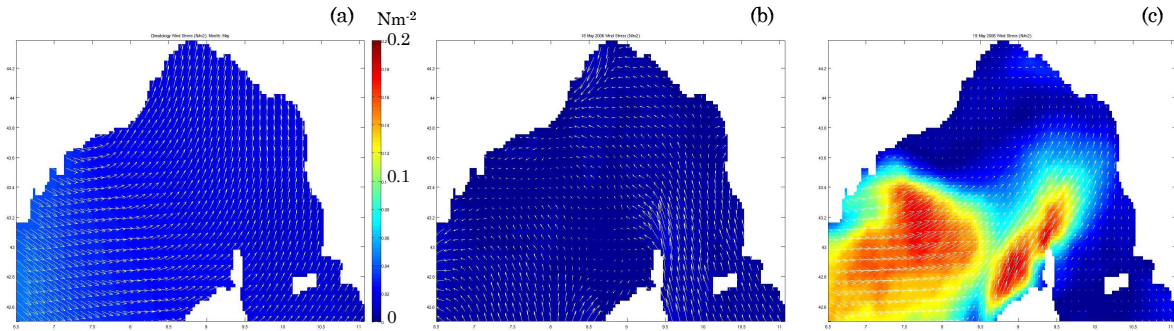


Fig. 4.4.8 Wind stress field (direction and intensity Nm^{-2}) from forcing files. (a) May climatology monthly mean from COADS dataset, (b) 18 May 2006 from COSMO-I7 dataset, (c) 19 May 2006 from COSMO-I7 dataset.

Summarizing, figures 4.4.5 and 4.4.6 indicate the ability of the interannual run (Run 9) in simulating mesoscale structures and a great fields daily variability. As, in this work of thesis, we are interested in the influence of mesoscale structure on biological production, we focus the attention, in the following sections, on interannual runs which clearly simulate mesoscale structures and a greater fields variability.

4.5 Wind effect on mesoscale eddies structures

In this section the LS-ROMS model has been used to study numerically the dynamics of the Liguro-Provençal-Catalan current. We show that the coastal current undergoes meandering instabilities that generate intense anticyclonic mesoscale and submesoscale eddies in the Ligurian Sea. Vortex generation is particularly efficient when realistic wind forcing, instead of climatological wind forcing, is adopted, confirming the importance of the

interaction between variable winds, surface currents and topographic features.

To this end, we compare the results of two sets of simulations, called RUN1 (the configuration into the row “Run 7” of the table 4.1.1 corresponds to the simulation hereafter referred to as RUN1) and RUN2 (the configuration into the row “Run 9” of the table 4.1.1 corresponds to the simulation hereafter referred to as RUN2). Both types of run are forced by daily mean boundary conditions (from the MFS 2006 dataset) at the open lateral boundaries. The sea-atmosphere heat and freshwater fluxes in both simulations are provided by the climatological monthly mean dataset COADS. In RUN1, the wind stress has low spatial and temporal resolution ($1/2^\circ$ and 1 month respectively) and it is provided by the COADS climatology dataset. As it is a climatological mean, the peak strength and the spatial variance of the wind stress are smaller than the instantaneous values and the energy injected into the surface sea layer is correspondingly lower. In RUN2, the wind stress refers to the year 2006 and it is provided by the COSMO-I7 (LAMI) dynamic model of the atmosphere; in RUN2, the wind stress has both higher spatial and temporal resolution ($1/16^\circ$ and 3 hours respectively) and larger instantaneous values.

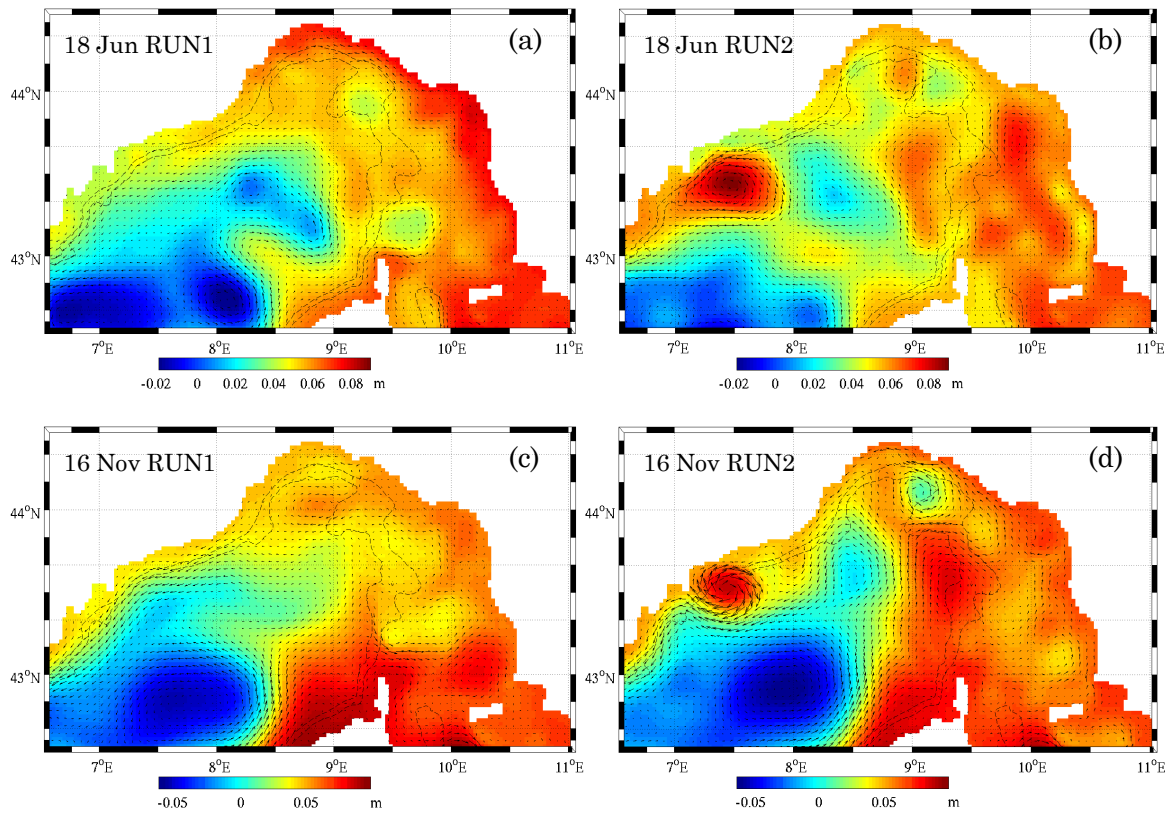


Fig. 4.5.1 Comparison of (a) RUN1 and (b) RUN2. Distribution of SSH in meters on 18 June 2006 and comparison of (c) RUN1 and (d) RUN2. Distribution of SSH in meters on 16 November 2006. Vectors indicate current direction at a depth of 10 meters.

Figures 4.5.1a and 4.5.1b show two examples circulation patterns obtained with the two types of wind stress. The variable shown in the figures is sea surface height (SSH), which allows for detecting mesoscale structures and the associated geostrophic circulations. Vectors indicate horizontal currents at a depth of 10 meters. Figures 4.5.1a and 4.5.1c show the output of RUN1 and figures 4.5.1b and 4.5.1d shows the results obtained in RUN2. Figures 4.5.1a and 4.5.1b refer to 18 June 2006 and figures 4.5.1c and 4.5.1d to 16 November 2006.

Clearly, one cannot compare the details of the circulation in RUN1 and RUN2 owing to the different properties of the wind-stress forcing. However, observation of these figures and quantitative analysis of the whole dataset indicate that there are significant differences between the two types of run:

In general, the circulations simulated in RUN2 are characterized by the presence of intense mesoscale eddies which are instead rather weak in RUN1. This is particularly evident in the western portion of the simulation region and during the fall, where the results of RUN2 indicate the emergence of coastal anticyclonic eddies which slowly move with the Ligurian Sea current. These results suggest that the instability of the current is triggered and amplified by the more intense and higher-frequency wind stress pattern provided by the meteorological model.

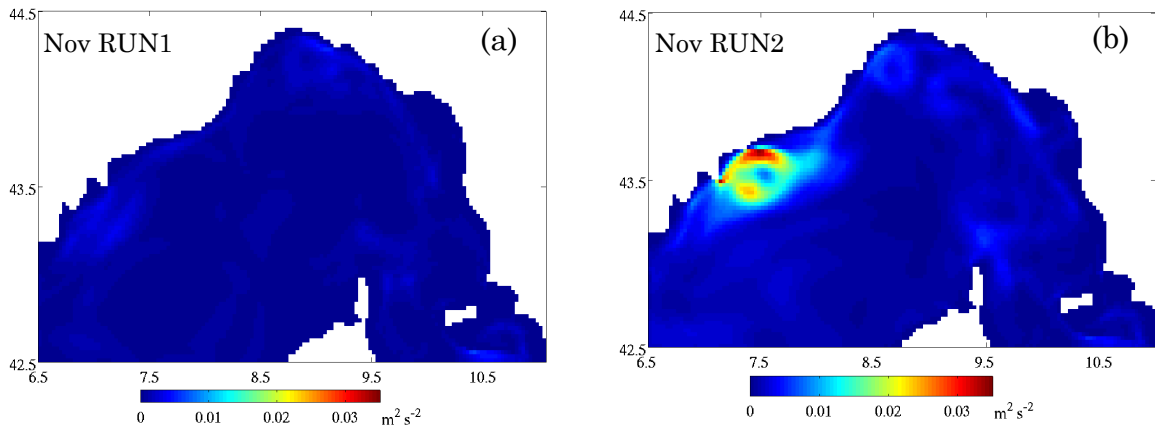


Fig. 4.5.2 Comparison of (a) RUN1 and (b) RUN2. Distribution of the mean eddy kinetic energy (in $\text{m}^2 \text{s}^{-2}$), averaged over the whole month of November 2006 and over the upper 100 meters of the water column.

To quantify the differences between RUN1 and RUN2, figure 4.5.2 shows the mean horizontal eddy kinetic energy (EKE) in November 2006 in the upper portion of the water column, for RUN1 (figure 4.5.2a) and RUN2 (figure 4.5.2b). The mean horizontal EKE has been defined as the average, over the month of November and the upper 100 meters of the water column, of

$$EKE = \frac{1}{2} \left\{ [u(x, y, z, t) - U(x, y)]^2 + [v(x, y, z, t) - V(x, y)]^2 \right\}$$

where $u(x,y,z,t), v(x,y,z,t)$ are respectively the zonal and meridional components of horizontal velocity at point (x,y,z) and time t and $U(x,y), V(x,y)$ are the average monthly horizontal velocities in the upper 100 meters. In the case of the COSMO-I7 2006 dataset, the average EKE is much larger, and clearly marks the area where the strong anticyclonic structure has been generated.

The anticyclonic vortex evident in figures 4.5.1d and 4.5.2b is a persistent eddy and its lifetime has been estimated, from the numerical simulation, to be about 43 days. The eddy diameter varies with time, reaching a maximum of about 80 km. The eddy slowly moves with the Ligurian Sea current with a total displacement of about 130 km; that is, the eddy does not move much during its lifetime and it is trapped between the current and the coastline.

To further characterize the structure of this anticyclonic eddy, we resort to Okubo-Weiss parameter, $Q(x,y,t)$, usually adopted to study two-dimensional coherent vortices (see Weiss, 1991; Provenzale, 1999). This parameter can be estimated from the Jacobian of the horizontal velocities as $Q = s^2 - \zeta^2$

where $s^2 = \left(\frac{\partial u}{\partial x} - \frac{\partial v}{\partial y}\right)^2 + \left(\frac{\partial v}{\partial x} + \frac{\partial u}{\partial y}\right)^2$ is the square of the total horizontal strain

and $\zeta^2 = \left(\frac{\partial v}{\partial x} - \frac{\partial u}{\partial y}\right)^2$ is the squared vorticity of the horizontal motion. In the

cores of barotropic vortices, vorticity dominates and $Q \ll 0$, while at the vortex periphery strain dominates and one finds a ring where $Q \gg 0$. In the background turbulence far from coherent vortices, strain and vorticity nearly balance and $Q \approx 0$. For baroclinic vortices such as those studied here, the situation is more complex but the Okubo-Weiss parameter still provides a heuristic way to identify the presence of vortices.

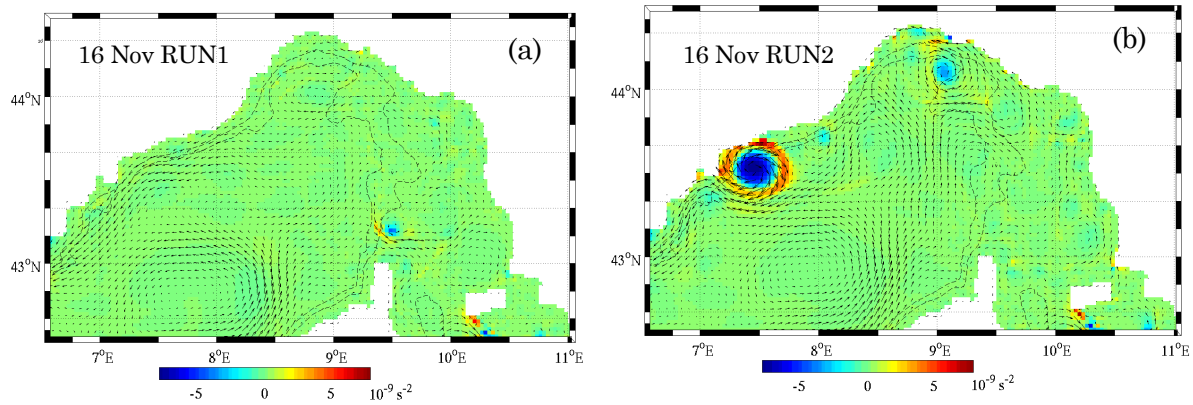


Fig. 4.5.3 Comparison of (a) RUN1 and (b) RUN2. Distribution of the Okubo-Weiss parameter (in s^{-2}) on 16 November 2006. Vectors indicate current direction at a depth of 10 meters.

Figure 4.5.3 shows the spatial distribution of the Okubo-Weiss parameter for the case shown in figures 4.5.1c,d. The difference between RUN1 and RUN2 is striking: While in RUN1 (figure 4.5.3a) the modulus of Q is small everywhere, in RUN2 (figure 4.5.3b) the parameter Q clearly identifies the presence of a strong coherent vortex in the western portion of the domain, between the coast and the current. This confirms that the stronger and more variable wind stress has a significant impact on mesoscale structures and, in the simulation considered here, it generates intense eddy structures in the coastal area.

To better understand the processes associated with this eddy, we apply the one-way LS-ROMS embedding procedure to the area containing the eddy. To this end, a reduced-domain model (the "child grid" model) with resolution 1 km is embedded in the "parent" model to better resolve the dynamics of intense coastal eddies. The domain of the child grid is located in the northwestern part of the study region and it extends from 6.8° E to 8.3° E and from 43° N to 44.1° N . The child grid is embedded in a one-way nesting within the parent grid.

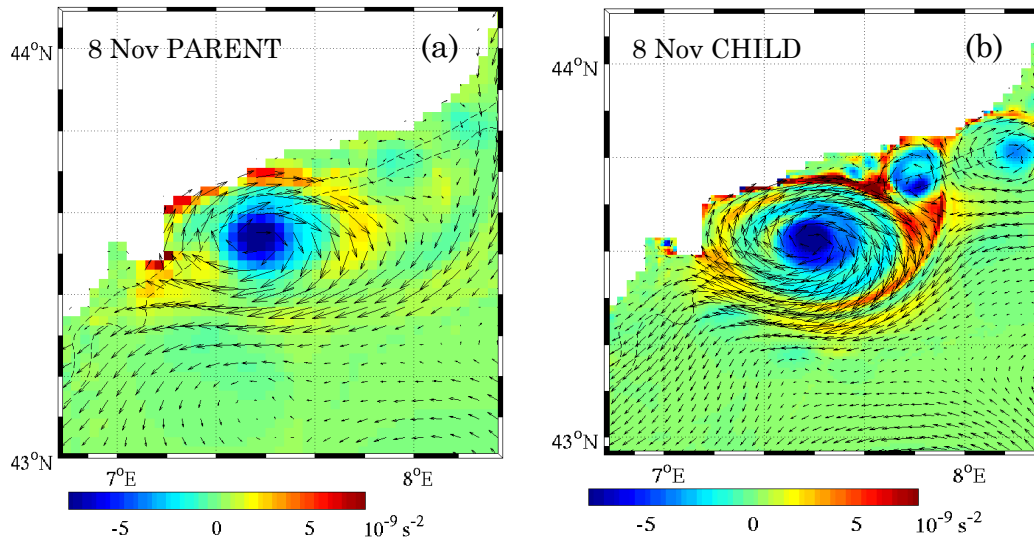


Fig. 4.5.4 Comparison of (a) parent and (b) child grid model. Okubo-Weiss parameter (in s^{-2}) on 8 November 2006. Vectors indicate current direction at a depth of 10 meters.

With this procedure, we increase the resolution in the region of interest from 3 km to 1 km. Figure 4.5.4 shows the Okubo-Weiss parameter computed from the lower resolution (parent) and higher resolution (child) simulations. In the child grid model (figure 4.5.4b), the structure of the eddy is defined much better. In addition, the simulation at higher resolution reveals the presence of more structures than those detected with the lower-resolution, parent model. In particular, to the East (upstream) of the anticyclonic eddy, one notices at least two smaller sub-mesoscale eddies, including a cyclonic coastal eddy, which are barely visible in the parent model simulation.

Mesoscale and submesoscale eddies are accompanied by a complex pattern of vertical velocities. In the open ocean, the results of Koszalka et al. (2009) show that mesoscale anticyclones induce a field of intense vertical motions, associated with the presence of vortex Rossby waves and of inertial waves at larger depths. These vertical velocities cannot be described in the framework of the quasigeostrophic approximation and become so strong to be comparable with those encountered in frontal regions.

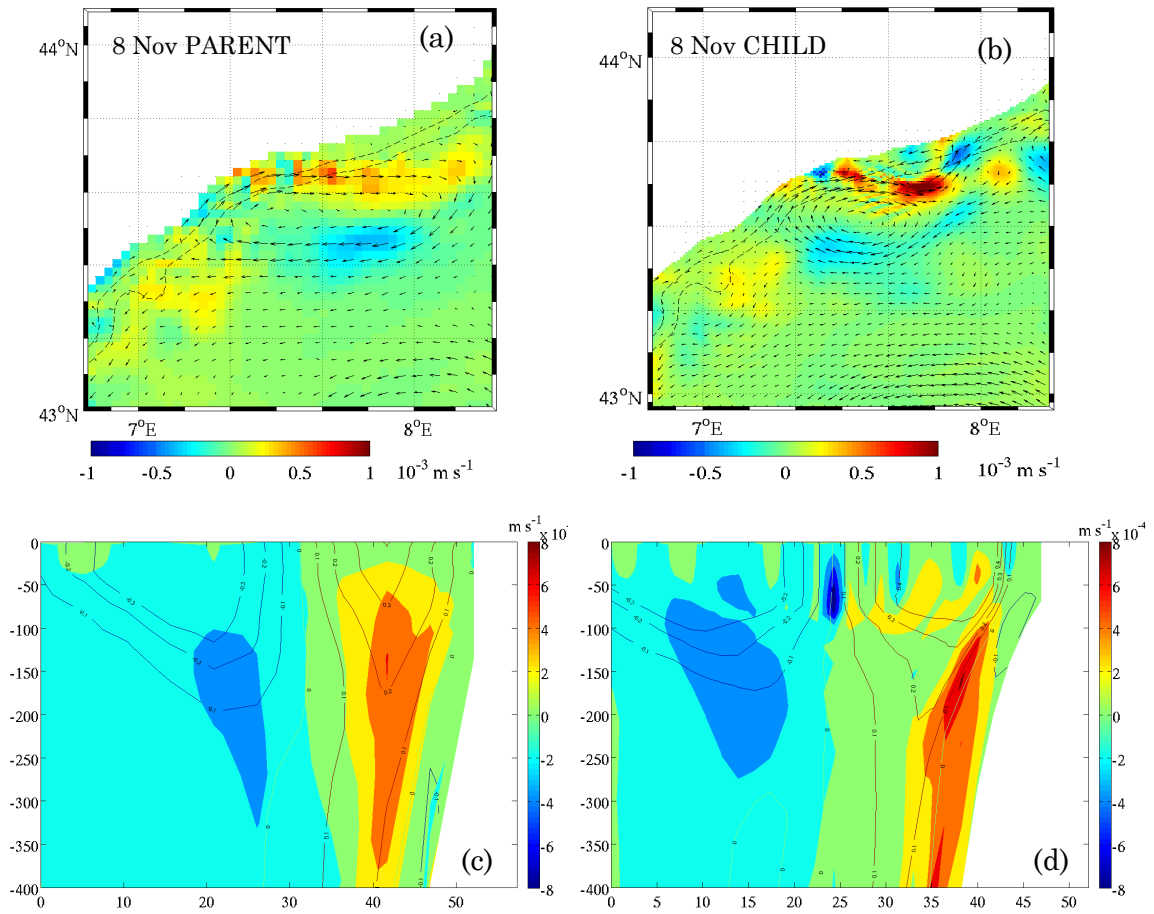


Fig. 4.5.5 Panels (a,b): Vertical velocity, in m s^{-1} , at a depth of 150 meters, for the parent (a) and child grid (b) models. Panels (c,d): Vertical velocity field, in m s^{-1} , in a meridional slice at longitude 7.49° E crossing the vortex shown in figure 4.5.3, for the parent (c) and child grid (d) models. Contours indicate the zonal (u) component of velocity. All data refer to 8 November 2006.

The anticyclonic eddies generated by the instability of the coastal Liguro-Provençal-Catalan current are also associated with intense vertical motion. Figures 4.5.5a,b show the pattern of instantaneous vertical velocities at a depth of 150 meters and figures 4.5.5c,d show the vertical velocity distribution in a meridional vertical slice located at longitude 7.49° E and latitude between 43.31° and 43.79° N , that cross the vortex shown in figure 4.5.3. Panels (a,c) are for the parent model with resolution 3 km and panels (b,d) are for the child grid model with resolution 1 km. Associated with the

vortex system, one can see a complex pattern of strong, alternating positive and negative vertical velocities. On the coast-ward side of the main anticyclonic vortex, it is visible an area of intense, positive vertical velocities associated with upwelling. On the open-sea side of the main vortex, there is strong downwelling. Nothing of this can be seen when the vortex is absent, as in RUN1, where there is only a weak coastal downwelling associated with the cyclonic coastal current. The use of a higher-resolution model, as in the case of the child grid of figure 4.5.5b, further emphasizes the strength of the vertical velocity pattern. Maximum values of the modulus of vertical velocity for the parent model are 50 meters per day, while for the higher-resolution child grid model they can reach values of about 70 meters per day. These vertical velocities are rather strong and can lead to a significant nutrient input into the euphotic layer at the coastal side of the eddies.

4.6 Downscaling from 3km to 300m

This section is a supplementary section where the resolution of the LS-ROMS model for the whole year 2006 has been firstly increased and, successively the one way embedding procedure has been applied to the high resolution LS-ROMS model, for the month of November. The aim of the downscaling is, once more, to finely resolve the dynamic of intense coastal eddies. The domain of the child grid is in the North West part of the study region and extends from 6.7° E to 8.4° E and from 43° N to 44.2° N. The child grid is embedded in a one-way manner within the parent grid. The grids have 32 vertical levels.

The goal of this section is to show how different configurations of the model act on the simulation of the eddy identified in section 4.5.

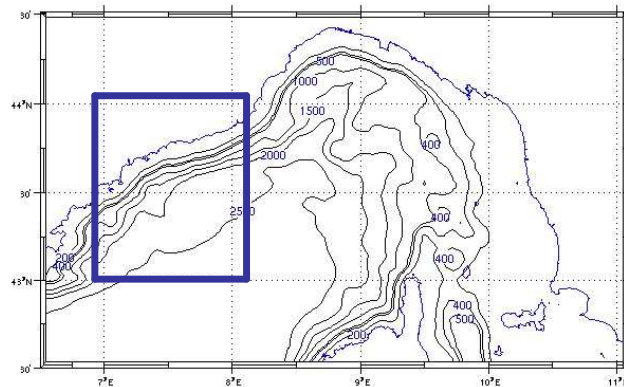


Fig. 4.6.1 Representation of the parent and the child domain. The domain of the child grid extends from 6.7° E to 8.4° E and from 43° N to 44.2° N. The bottom topography is based on the global topography dataset at $2'$ resolution (Smith and Sandwell, 1997).

Figure 4.6.1 shows the parent (entire figure) and the child (smaller box) domain. Hereafter a comparison between four simulations is presented. The configuration of these simulations is included in table 4.1.1, run 9 and run 10. Run 9 (hereafter referred to as parent 1) is the simulation with resolution 3 km described in chapter 4.5. Run 10 (hereafter referred to as parent 2) is a simulation of the year 2006 with the same configuration of the run 9, except for the resolution. The spatial resolution of run 10 is 1 km. In both simulations the embedding procedure has been applied achieving the spatial resolution of 1 km and 300 m respectively.

Figure 4.6.2 shows the speed (colour) into the region dominated by the coastal anticyclonic eddy. Figure 4.6.2a shows the speed computed from the lower resolution (parent 1) simulation with spatial resolution 3 km. Figure 4.6.2b shows the speed computed from the higher resolution (child 1) simulation with spatial resolution 1 km. Figure 4.6.2c represents the lower resolution (parent 2) simulation with spatial resolution 1 km and figure 4.6.2d represents the higher resolution (child 2) simulation with spatial resolution of 300 m. The two simulations, child 1 and parent 2, have the

same resolution but they differ for the boundaries. In fact, in the first case (child 1) it is a downscaling from the simulation parent 1 while in the second case (parent 2) it is a simulation for the whole study area and for the whole year. Indeed the difference between the two simulations is the domain.

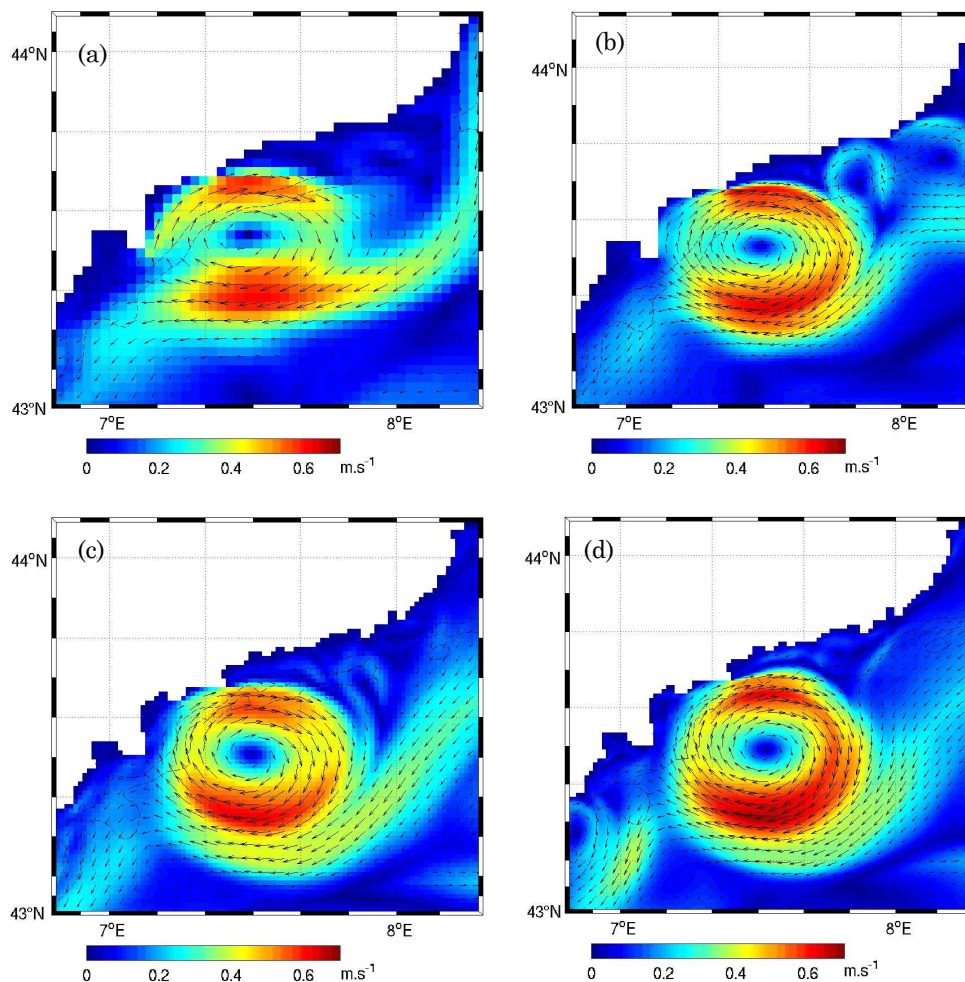


Fig. 4.6.2 Comparison of (a) parent 1 and (b) child 1 grid model and of (c) parent 2 and (d) child 2 grid model. Speed variable (colour) at the depth of 10 meters on 8 November 2006. Vectors indicate current direction at a depth of 10 meters.

Figure 4.6.2 indicates that there is not a noticeable difference for the horizontal velocities increasing the resolution. One can observe that the structure of the eddy is better defined into the higher resolution simulations (4.6.2b,c,d) but the values of velocity don't differ significantly between the

simulations. In the lowest resolution run (figure 4.6.2a), the maximum value of speed is 0.61 m s^{-1} which increases at 0.64 m s^{-1} into the two runs with 1 km of resolution. The highest resolution simulation (figure 4.6.2d) has a maximum speed value of 0.66 m s^{-1} .

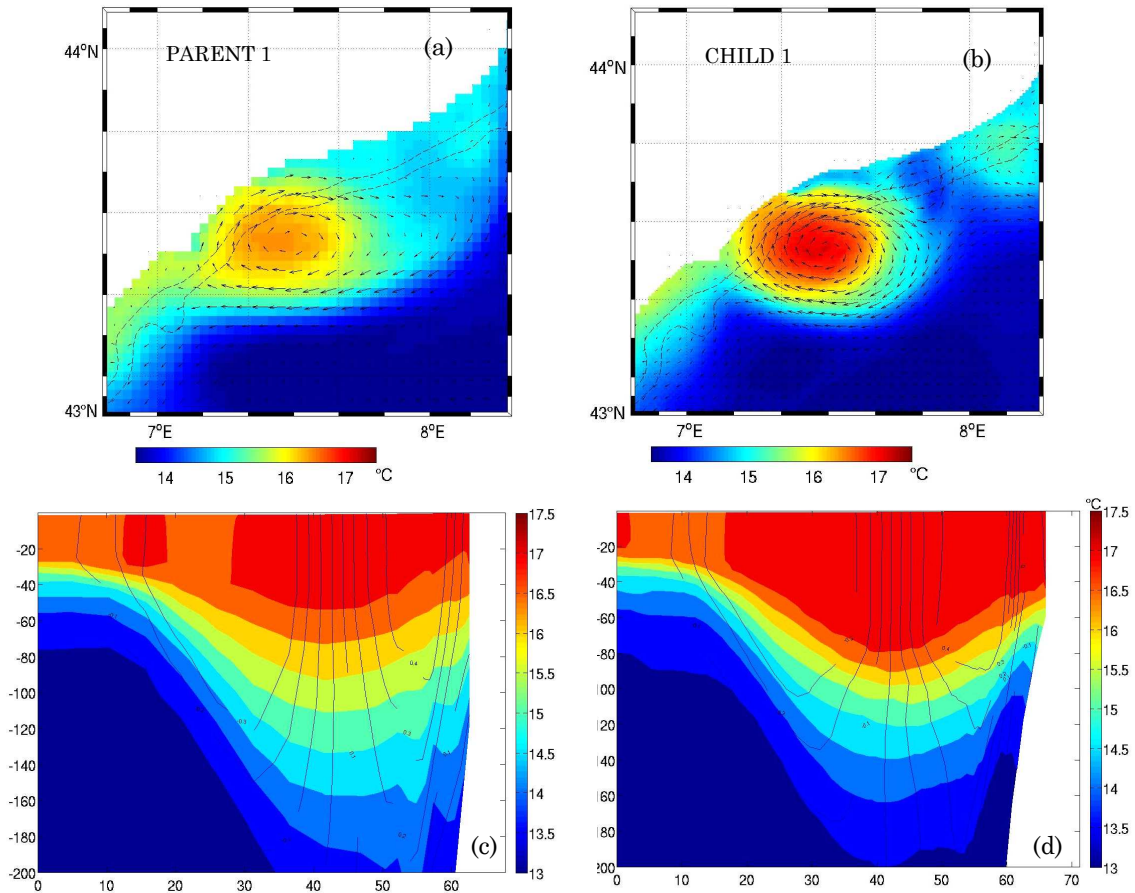


Fig. 4.6.3 Comparison of (a) (c) parent 1 and (b) (d) child 1 grid model on 8 November 2006. Panels (a, b): Horizontal distribution of temperature in $^{\circ}\text{C}$ at the depth of 80 meters. Vectors indicate current direction at the depth of 80 meters. Panels (c, d): Vertical distribution of temperature in $^{\circ}\text{C}$ in a meridional slice at longitude 7.51°E crossing the vortex, for the parent 1 (c) and child 1 (d) grid models. Contours indicate the zonal (u) component of velocity.

Figure 4.6.3 shows the horizontal and vertical distribution of temperature in correspondence of the eddy. It compares the distribution of temperature computed from the parent 1 and the child 1 simulations. Figures 4.6.3a and b show a warmer core in correspondence of the coastal anticyclonic eddy due

to surface convergence. The parent 1 simulation (figure 4.6.3a) indicates, into the core of the eddy, a temperature of 16.5°C , at the depth of 80 m, while the surrounding environment has a temperature between 14 and 15.5°C . The child 1 simulation (figure 4.6.3b) shows, into the core of the eddy, a temperature of about 17°C , at the depth of 80 m. In this simulation the structure of the eddy is defined much better. Figures 4.6.3c and d show the vertical distribution, in the first 200 m, of temperature in a meridional vertical slice located at longitude 7.51°E and latitude 43.15° and 43.79°N that cross the vortex. Both figures show a depression of the thermocline in correspondence of the core of the eddy. The child 1 simulation shows a higher depression of the thermocline which reaches 80 m and it has a higher temperature gradient.

Figure 4.6.4 shows the horizontal and vertical distribution of temperature in correspondence of the eddy. It compares the distribution of temperature computed from parent 2 and child 2 simulations. Figures 4.6.3b,d and 4.6.4a,c show the temperature distribution computed from the same resolution model, 1km, but different domain as described in the first part of the section. They show similar values of temperature but there are some differences in the structure of the eddy due to the different domain. Figures 4.6.4b and d show the distribution of temperature computed from child 2 which is the highest resolution simulation (300 m). The structure of the eddy is defined much better and reveals the presence of more small structures. Figure 4.6.4d shows the vertical distribution, in the first 200 m, of temperature in a meridional vertical slice located at longitude 7.51°E and latitude 43.15° and 43.79°N that cross the vortex. The figure shows a warm core in correspondence of the eddy which is warmer than the core in the other simulations probably due to the effect of the resolution.

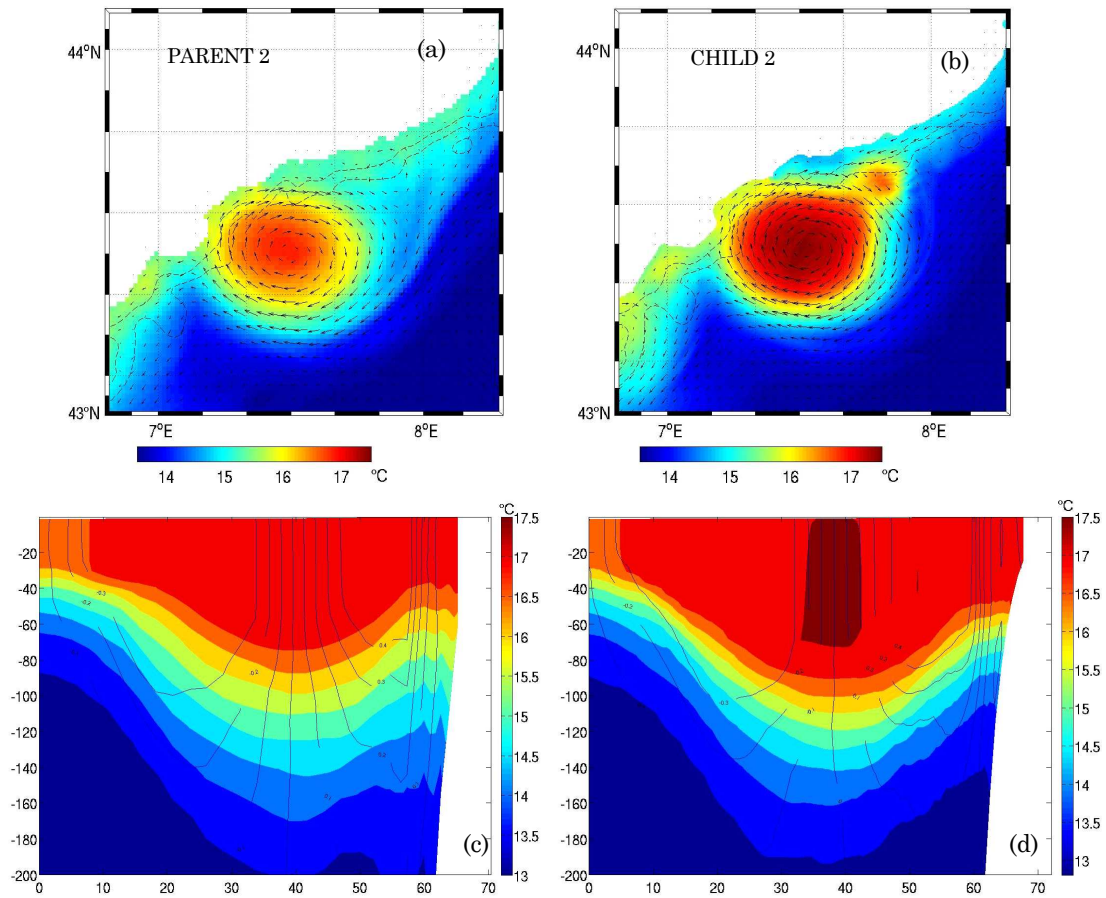


Fig. 4.6.4 Comparison of (a) (c) parent 2 and (b) (d) child 2 grid model on 8 November 2006. Panels (a, b): Horizontal distribution of temperature in °C at the depth of 80 meters. Vectors indicate current direction at the depth of 80 meters. Panels (c, d): Vertical distribution of temperature in °C in a meridional slice at longitude 7.51°E crossing the vortex, for the parent 2 (c) and child 2 (d) grid models. Contours indicate the zonal (u) component of velocity.

All simulations indicate that the horizontal and the vertical distribution of temperature can give information about the presence and structure of anticyclonic eddies. The high resolution allows to detect a much better defined structure, at large scale, and several smaller scale structures.

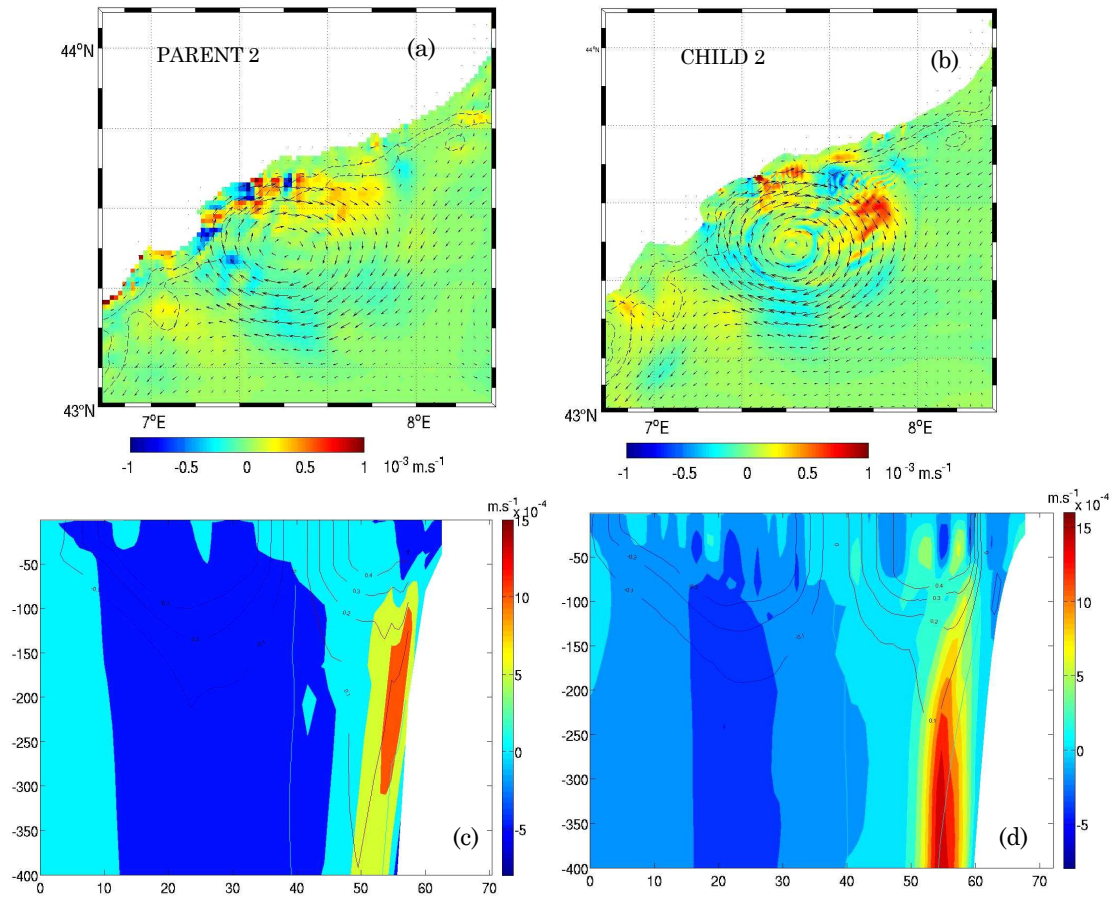


Fig. 4.6.5 Panels (a,b): Vertical velocity, in m s^{-1} , at a depth of 80 meters, for the parent 2 (a) and child 2 grid (b) models. Panels (c,d): Vertical velocity field, in m s^{-1} , in a meridional slice at longitude 7.49° E crossing the vortex, for the parent 2 (c) and child 2 grid (d) models. Contours indicate the zonal (u) component of velocity. All data refer to 8 November 2006.

Figure 4.6.5 shows a similar situation showed in figure 4.5.5 (section 4.5) between the parent 1 and child 1 simulations.

Figures 4.6.5a,b show the pattern of instantaneous vertical velocities at a depth of 80 meters and figures 4.6.5c,d show the vertical velocity distribution in a meridional vertical slice located at longitude 7.49° E and latitude between 43.15° and 43.79° N , that cross the vortex. Panels (a,c) are for the parent 2 model with resolution 1 km and panels (b,d) are for the child 2 grid model with resolution 300 m. Associated with the vortex system,

one can see a complex pattern of strong, alternating positive and negative vertical velocities. On the coast-ward side of the main anticyclonic vortex, it is visible an area of intense, positive vertical velocities associated with upwelling. On the open-sea side of the main vortex, there is a downwelling. The values of positive vertical velocity described in section 4.5 indicate that the maximum values of the modulus of vertical velocity for the parent 1 model are 50 m d^{-1} , while for the higher-resolution child 1 grid model they can reach values of about 70 m d^{-1} . Figure 4.6.5d has maximum values of the modulus of vertical velocity of the order of 120 m d^{-1} . This means that the rise of resolution allows to finely resolve the vertical velocity field. In the first 50 m depth, figure 4.6.5d, shows a complex pattern of strong, alternating positive and negative vertical velocities.

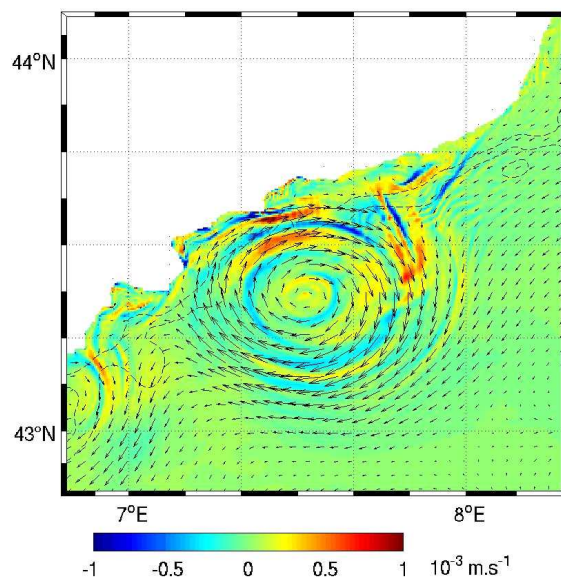


Fig. 4.6.6 Vertical velocity, in m s^{-1} , at a depth of 40 meters, for the child 2 model. Vectors indicate current direction at the depth of 40 meters. The data refer to 8 November 2006.

Figure 4.6.6 shows the pattern of instantaneous vertical velocities at a depth of 40 m for the child 2 model on 8 November 2006. One can observe the presence of a complex pattern of strong, alternating positive and negative vertical velocities in correspondence, and near, the eddy structure.

CHAPTER 4: RESULTS

This small scale processes are observable and better defined into the child 2 simulation with resolution 300 m.

The rise of resolution allowed to finely resolve the distribution of vertical velocity field which permitted to observe a complex pattern of strong, alternating positive and negative vertical velocities in correspondence of the eddy structure. For horizontal velocities, the increase of resolution has not a noticeable impact on its intensity and distribution which means that the process is sufficiently solved by the low resolution model. As regard temperature, it can give information about the presence and the structure of the eddy. Moreover, as regard temperature, the rise of resolution allows to detect a much better defined structure and more small structures.

In conclusion, one can observe that the increase of resolution has an impact on i) structure of the eddy, ii) physical parameters and iii) processes at small spatial and temporal scale.

4.7 *Biological production*

The biogeochemical model is a nitrogen based NPZD model (section 3.3.2). The input data of the biogeochemical model, described in section 4.3, are essentially nitrate and chlorophyll. Phytoplankton and zooplankton input data are estimated from chlorophyll data (section 4.3). The equations of the NPZD model are described in section 3.3.2 and a complete list of the values and explanation of all parameters is given in table 4.7.1. The system of four coupled partial differential equations governs the time and space distribution of Nitrate, Phytoplankton, Zooplankton and Detritus. Moreover, we extract the primary production flux defined as *Primary Production* = $\mu^P \cdot P$. This term has been integrated on 24 h. The state variables represent concentrations of nitrogen within the different compartments and their unit is mmol N m^{-3} , except for Primary Production which has units of $\text{mg C m}^{-3} \text{ d}^{-1}$. In this version of the model we consider a single nutrient compartment (nitrate) but a perspective for further development could be to use two nutrient compartments (nitrate and phosphate), since it appears that there is a shift from nitrate limitation during winter and spring to phosphate limitation during summer period in the Ligurian Sea (section 2.4). In this work of thesis, a simple NPZD model has been applied with single compartments coupled to the LS-ROMS version of the ROMS model.

CHAPTER 4: RESULTS

Parameter	Symbol	Value	Unit
<i>Phytoplankton parameters</i>			
Half-sat. conc. for nitrate uptake	K_N	0.5	mmol N m^{-3}
Phytoplankton linear mortality rate	m^P	0.03	d^{-1}
Initial slope of P versus I relationship	α_P	1.0	$(\text{W m}^{-2})^{-1} \text{d}^{-1}$
C:N ratio for phytoplankton	CN_{Phyt}	6.625	$\text{mmol C (mmol N)}^{-1}$
Max chlorophyll-to carbon ratio	θ^{max}	0.02	$\text{mg Chla (mg C)}^{-1}$
<i>Zooplankton parameters</i>			
Zooplankton grazing rate	g_{max}	0.9	d^{-1}
Zooplankton assimilation efficiency	β	0.75	-
Ivlev parameter of Z grazing formulation	iv_P	1.0	$(\text{mmol N m}^{-3})^{-1}$
Zooplankton quadratic mortality rate	m^Z	0.1	d^{-1}
Zooplankton specific excretion rate	μ_{ZE}	0.1	d^{-1}
<i>Remineralization</i>			
Remineralization rate of D	μ_{DN}	0.05	d^{-1}
<i>Sinking parameters</i>			
Sinking velocity of P	w^P	0.5	m d^{-1}
Sinking velocity of D	w^D	5.0	m d^{-1}
<i>Optical parameters</i>			
Light attenuation coeff. for seawater	K_w	0.04	m^{-1}
Chl-a specific light attenuation coeff.	K_{chla}	0.024	$\text{m}^{-1} (\text{m}^{-3} \text{mg Chla})^{-1}$

Tab. 4.7.1 Values, units, and definitions for the parameters of the biogeochemical model.

The typical temporal evolution of the phytoplankton biomass at mid-latitudes (section 2.4), indicates: i) a typical spring bloom between April and May, which can be observed also from satellite images; ii) an oligotrophic period during summer, which prevails at the surface while a reduced concentration of biomass is localized in the sub-surface layers. In the next part of the section the seasonal evolution of the variables simulated by the biogeochemical model coupled with the LS-ROMS versions of the ROMS model will be presented. The biological module has been coupled with both the climatology (section 4.4) and the interannual (year 2006) simulations (section 4.4).

To interpret the model results, we examine the domain averaged time series over the simulation period of the biogeochemical variables. Firstly

climatology experiment is examined, successively the result achieved with the interannual version are considered, and finally we compare the two results.

During the firsts months of the year (January and February) the low production, due to low light intensity and winter mixing, dominates (figure 4.7.2b,c,e). The phytoplankton spring bloom occurs in the second half of March following the increasing light levels and stratification. The simulated timing of the bloom is consistent with previous observations, which occurs generally from mid-March to mid-April (section 2.4). The depth integrated (0-250m) phytoplankton concentration (figure 4.7.2a) during the peak of the spring bloom, reaches $0.7136 \text{ mmol N m}^{-2}$ ($1.135 \text{ mg Chla m}^{-2}$) and it develops during the firsts days of April. The coincident peak of primary production (figure 4.7.2b) reaches $19.8497 \text{ mg C m}^{-2} \text{ d}^{-1}$. The decline of the bloom at the end of April coincides with the nitrate depletion (figure 4.7.2d) in the euphotic zone and an increasing grazing pressure from zooplankton (figure 4.7.2f). Approximately, 13 days after the maximum phytoplankton biomass is reached, the model simulates a peak of zooplankton biomass (figure 4.7.2a) with a maximum of $0.5269 \text{ mmol N m}^{-2}$ (41.9 mg C m^{-2}). Following the bloom and the nutrient depletion in the upper layer, a deep maximum of the phytoplankton biomass develops in the vicinity of the nitracline near 45 m (figure 4.7.2e). Together with the phytoplankton biomass, the primary production gradually decreases during summer and fall (figure 4.7.2c). The detritus maximum is reached after the phytoplankton bloom and during the zooplankton maximum (figure 4.7.2g).

CHAPTER 4: RESULTS

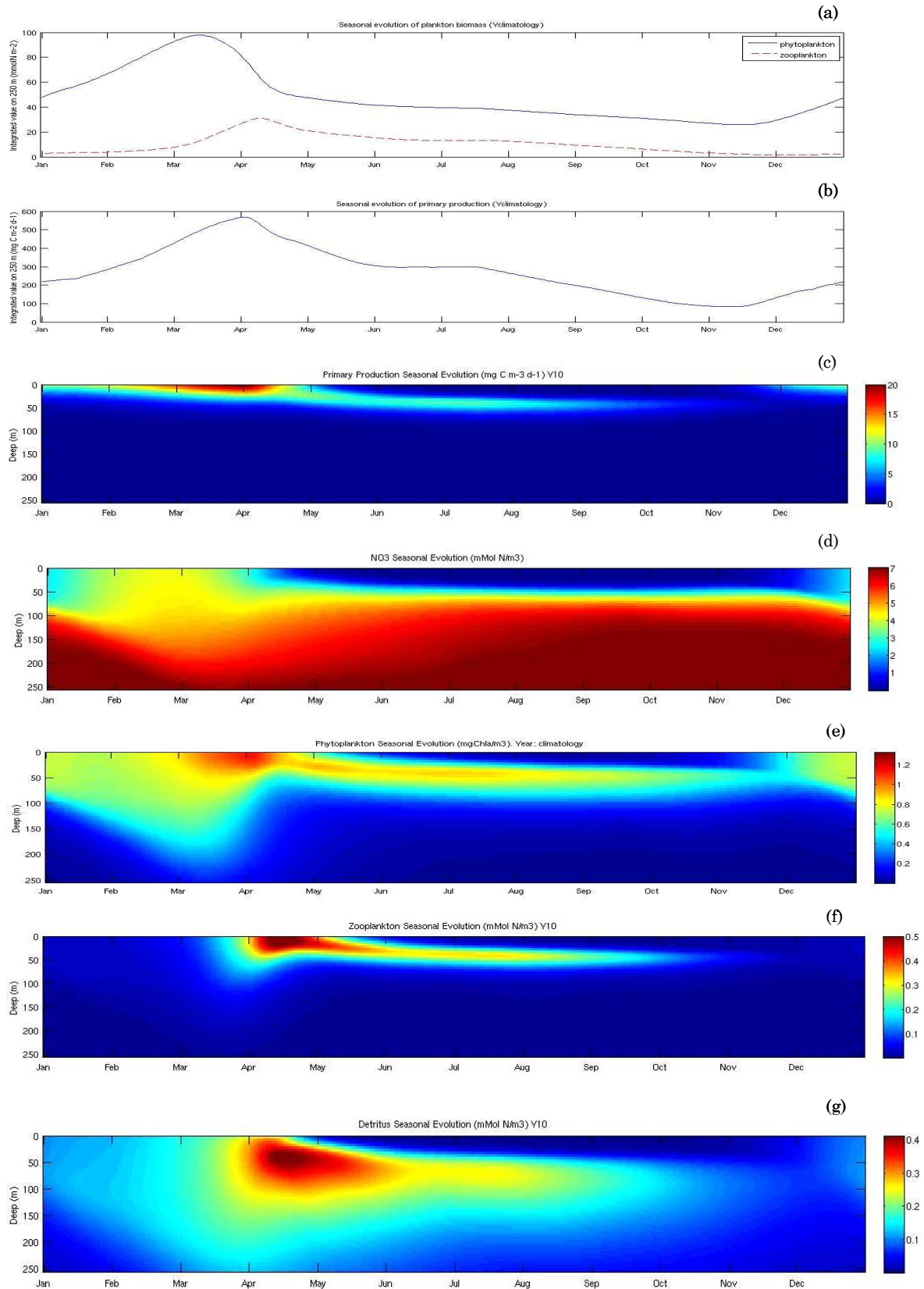


Fig. 4.7.2 Seasonal evolution in the whole domain of (a) depth integrated (0-250m) biomass of plankton components (mmolNm⁻²), (b) depth integrated (0-250m) primary production

CHAPTER 4: RESULTS

($\text{mgCm}^{-2}\text{d}^{-1}$), (c) primary production ($\text{mgCm}^{-3}\text{d}^{-1}$), (d) nitrate (mmolNm^{-3}), (e) phytoplankton (mgCham^{-3}), (f) zooplankton (mmolNm^{-3}), (g) detritus (mmolNm^{-3}). Climatology experiment.

The interannual simulation (year 2006) differs from the climatological one, essentially for the physics, and in particular for the forcing data (different marine boundary conditions and different wind stress: section 4.3). These changes affect the biological variables, while the biogeochemical model and its parameters remain unchanged. Figure 4.7.3 shows the NPZD and primary production evolution for the interannual (year 2006) simulation. The evolution of the variables is qualitatively similar to the evolution of the variables in the climatology run (figure 4.7.2), but there is a greater variability in the interannual simulation.

CHAPTER 4: RESULTS

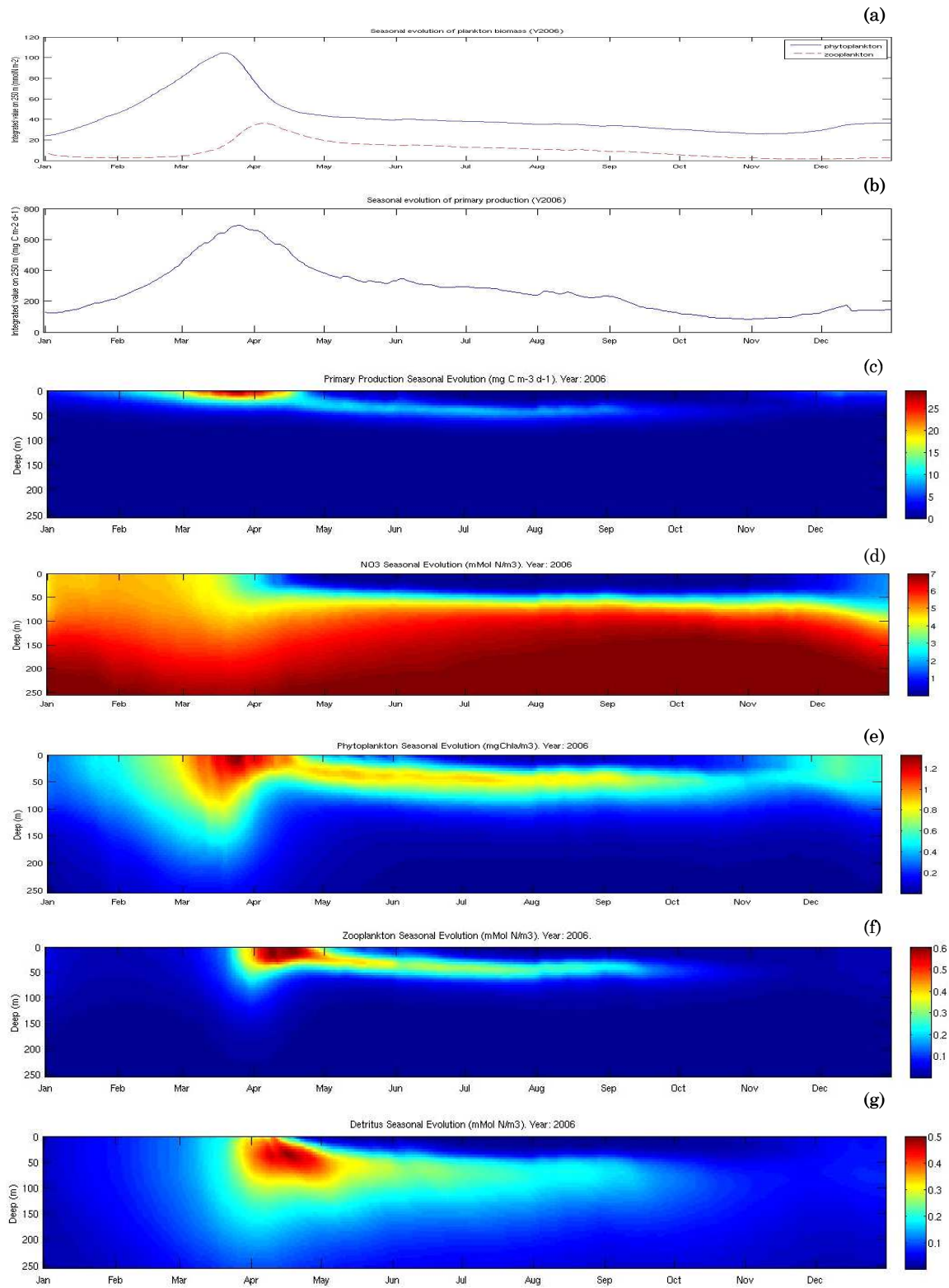


Fig. 4.7.3 Seasonal evolution in the whole domain of (a) depth integrated (0-250m) biomass of plankton components (mmolNm⁻²), (b) depth integrated (0-250m) primary production (mgCm⁻²d⁻¹), (c) primary production (mgCm⁻³d⁻¹), (d) nitrate (mMolNm⁻³), (e) phytoplankton

CHAPTER 4: RESULTS

(mgCham⁻³), (f) zooplankton (mmolNm⁻³), (g) detritus (mmolNm⁻³).. Interannual experiment.

In the interannual run, the depth integrated (0-250m) phytoplankton concentration (figure 4.7.3a) during the peak of the spring bloom, reaches 0.8349 mmol N m⁻² (1.327 mg Chla m⁻²) and it develops during the last days of March. The coincident peak of primary production (figure 4.7.3b) reaches 28.7969 mg C m⁻² d⁻¹. Both production peaks are greater than those in the climatology simulation. The decline of the bloom is at the end of April, like in the climatology run, and it coincides with: i) the nitrate depletion (figure 4.7.3d) in the euphotic zone; ii) an increasing grazing pressure from zooplankton (figure 4.7.3f). Approximately, 16 days after the maximum phytoplankton biomass is reached, the model simulates a peak of zooplankton biomass (figure 4.7.3a) with a maximum of 0.6051 mmol N m⁻² (48.1 mg C m⁻²). The peaks of phytoplankton, zooplankton, primary production and detritus are higher in the interannual simulation than in the climatology one although the input data of nutrient come from the same dataset. This is probably due to the presence of numerous mesoscale structures and to the great fields variability in the interannual simulation, which allow a larger volume of nutrient rich water to reach the euphotic layer.

Summarizing, the biological model acts in a coherent way in both cases (climatology and interannual experiments). The results provide evidence of a reasonable seasonal evolution characterized by:

- a winter mixing period with low biological production that allow nutrient to replenish the surface layer (figures 4.7.2d,e, 4.7.3d,e);
- a strong spring bloom in March-April favoured by relatively high nutrient concentrations in the surface layer and increasing light in spring (figures 4.7.2c,d, 4.7.3c,d);
- a less productive summer, the oligotrophic season, after the near total consumption of nutrients in the surface layer (0-40m), characterized

by a deep chlorophyll (or phytoplankton) maximum, called the DCM, associated with the nitracline (figures 4.7.2d,e, 4.7.3d,e). This system is stable due to the strong stratification and low winds in summer that limits the nutrient replenishment of the surface layer;

- a slightly more productive event in autumn when stronger winds and atmosphere cooling start to destroy the upper thermal stratification of the ocean, allowing then some mixing and nutrient replenishment of the surface layer (figures 4.7.2e, 4.7.3e). The decreasing light limits primary production in this period.

It is noticeable that the climatology simulation produces a stable cycle; all fields (P, Z, N, D) show the same time evolution each simulated year when the model runs for several years. The tenth year of simulation for the physical model which is the fourth for the biological model has been here presented. It is clearly visible on figure 4.7.2 that the end of December fields are similar to the early January ones. For the interannual run it is different. As the run is forced by “real” rather than climatologic wind and marine fields, each simulated year would be different from the others and naturally from a climatologic one. In the case presented, the two simulations do not start with the same initial conditions. The climatologic one is the fourth year of a stabilized multiyear run where early January NPZD fields are inherited from the preceding yet stabilized year while the interannual run starts with initial conditions from observations (DYFAMED and SeaWiFS data). This explains some differences during the winter period, mainly due to lower phytoplankton initial conditions in the interannual run, that allows a more efficient winter nutrient replenishment. This leads to a slightly more marked bloom in the interannual simulation with more phytoplankton biomass and more primary production (figure 4.7.4a and b) while the summer and autumn periods are more similar.

CHAPTER 4: RESULTS

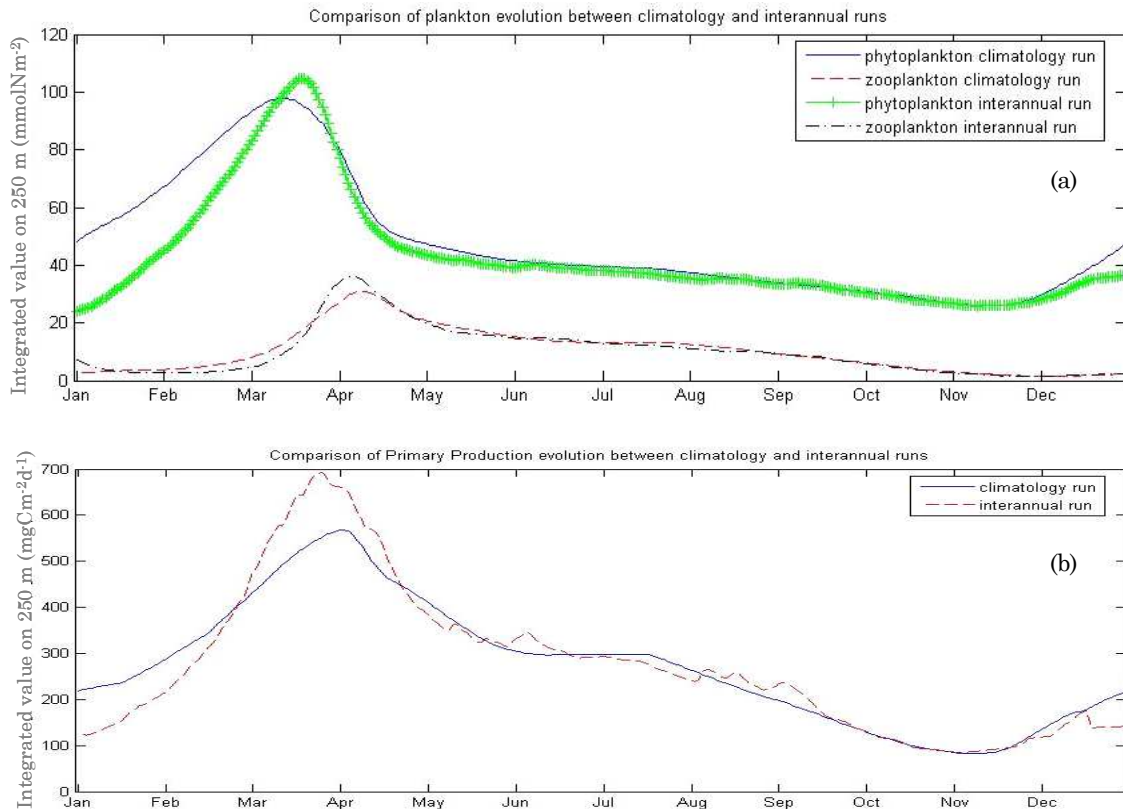


Fig. 4.7.4 Integrated value on 250 m of (a) phytoplankton, zooplankton and (b) primary production from climatology and interannual experiments.

Finally, it is also noticeable in figure 4.7.2d and 4.7.3d an higher variability in summer in the DCM in the interannual run due to the variability of the “real” wind and marine boundary forcing. In these figures, although the variability is small (as the figures are spatial averaged), it is however observable.

4.8 Primary production and impact of mesoscale structures on biological production

To detect in the whole region and in the whole simulated year the more productive area, we integrated on the year the primary production term for both simulations: the climatologic and the interannual runs.

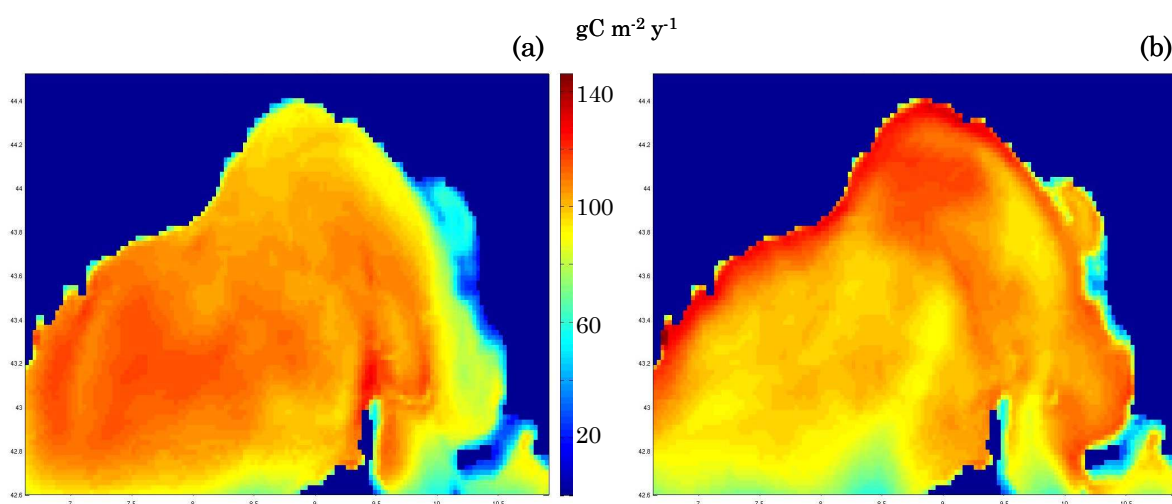


Fig. 4.8.1 Yearly integrated primary production from (a) climatology and (b) interannual experiments. Values range from 0 to 146 $\text{gCm}^{-2}\text{y}^{-1}$.

The yearly integrated primary production in the study region (figure 4.8.1a and b) shows the most productive area and the value of yearly integrated primary production for both experiments. The two runs show different results due to the impact of the different hydrodynamic on biological production. Figure 4.8.1b shows that the most productive area are located in the west ligurian-provencal coast and in the Gulf of Genoa. In the climatology simulation (figure 4.8.1a), the spatial distribution of primary production is more constant, and a less important maximum is observable in the North of Corsica. The climatology simulation is less dynamic (section 4.4) and doesn't simulate the intense eddies simulated by the interannual run.

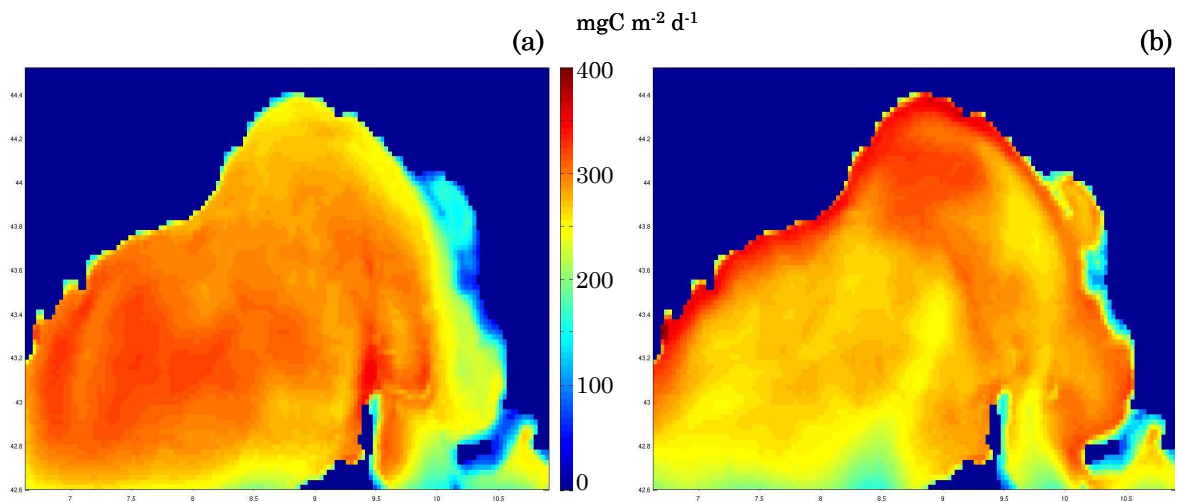


Fig. 4.8.2 Yearly mean primary production, integrated on vertical level, from (a) climatology and (b) interannual experiments. Values range from 0 to $400 \text{ mgCm}^{-2}\text{d}^{-1}$.

The yearly mean value of primary production, in the most productive area of the interannual simulation, reaches $400 \text{ mgCm}^{-2}\text{d}^{-1}$ (figure 4.8.2b) while the less productive area located in both simulations near the east coast range from 50 to $100 \text{ mgCm}^{-2}\text{d}^{-1}$ (figure 4.8.2a and b). The order of magnitude of production is globally satisfactory for both simulations since they are comparable with field observations. The field data collected at the DYFAMED station during the Tanaka and Rassoulzadegan seasonal study (Tanaka and Rassoulzadegan, 2002) indicate a range of value of primary production integrated in the upper 90 m during the different months of the year, between 65 (July) to $378 \text{ (May) mgCm}^{-2}\text{d}^{-1}$ (Marty, 2000. DYFAMED Observation Service).

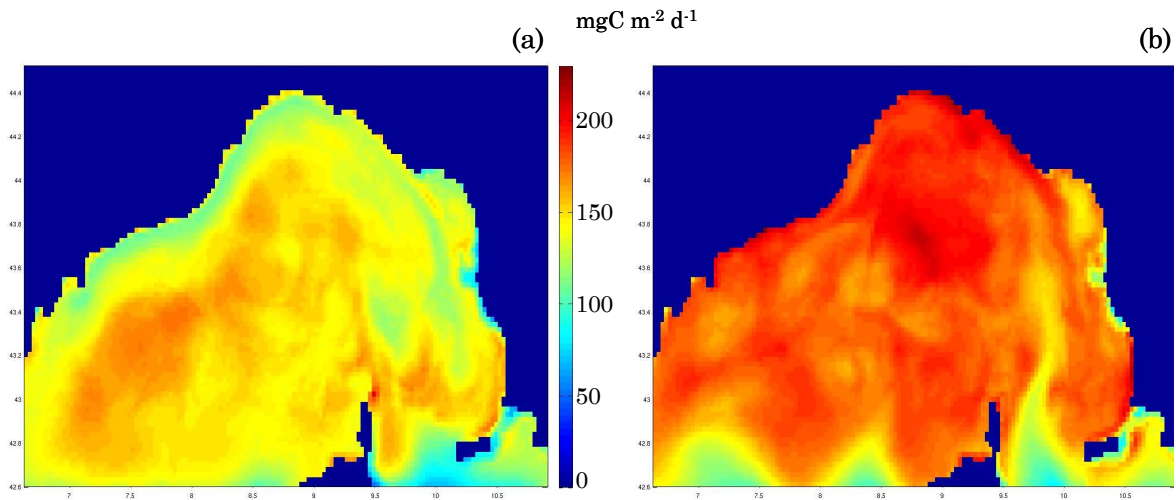


Fig. 4.8.3 Yearly standard deviation of primary production from (a) climatology and (b) interannual experiments. Values range from 0 to 240 $\text{mgCm}^{-2}\text{d}^{-1}$.

Figure 4.8.3 shows the yearly standard deviation of primary production from climatology and interannual simulations. This figure shows the local greater variability of primary production in the interannual simulation than in the climatological one.

The distribution of: i) yearly mean primary production (figure 4.8.2), ii) yearly integrated primary production (figure 4.8.1), iii) yearly standard deviation (figure 4.8.3), show a great difference and variability between the two simulations. There is a bigger production into the interannual simulation. The two results are globally satisfactory looking the order of magnitude of production, biomass and the seasonal evolution. Figure 4.8.3 shows a clear greater variability of the primary production into the interannual simulation due to a numbers of intense mesoscale structures and the great fields variability simulated by the interannual run.

The impact of eddies on biological production is observable analysing in detail peculiarly cyclonic and anti-cyclonic eddies. Hereafter a cyclonic and an anticyclonic eddy have been analyzed.

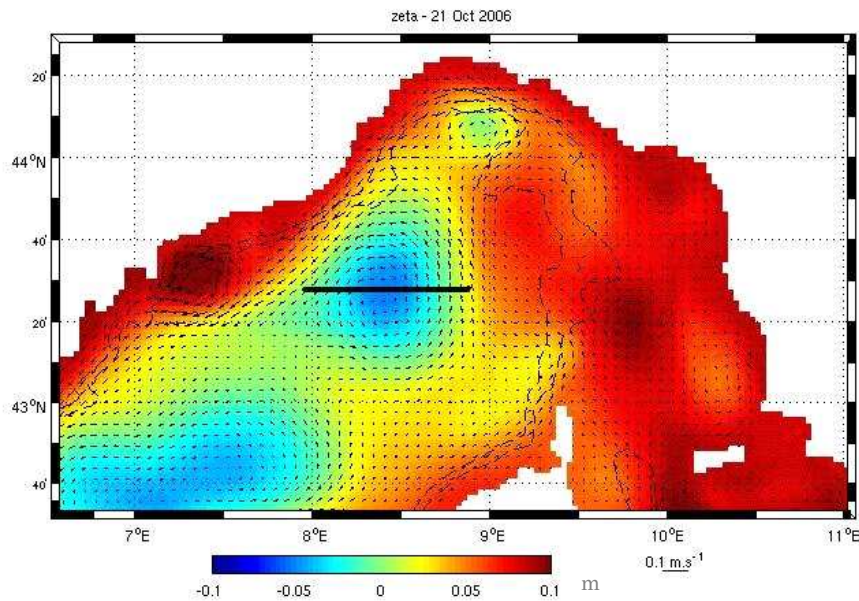


Fig. 4.8.4 SSH (colour) and current speed direction (vectors) of the 21 October 2006 of the interannual simulation.

Figure 4.8.4 shows several eddies simulated by the interannual simulation on 21 October 2006. In this figure SSH and vectors speed allow to detect eddies. In the next part of the section the analysis of the behaviour of biogeochemical variables into the central cyclonic eddy of the figure 4.8.4 have been done.

Figure 4.8.5a shows the presence of high values of primary production, integrated on 150 m, in correspondence of particular structures. Focusing the attention on the central cyclonic eddy, it is noticeable the impact of the cyclonic eddy on the biological production. Looking the whole area it is also noticeable the higher primary production concentration in correspondence of the Gulf of Genoa (cyclonic eddy), offshore Nice (anticyclonic eddy) and in the North of Corsica.

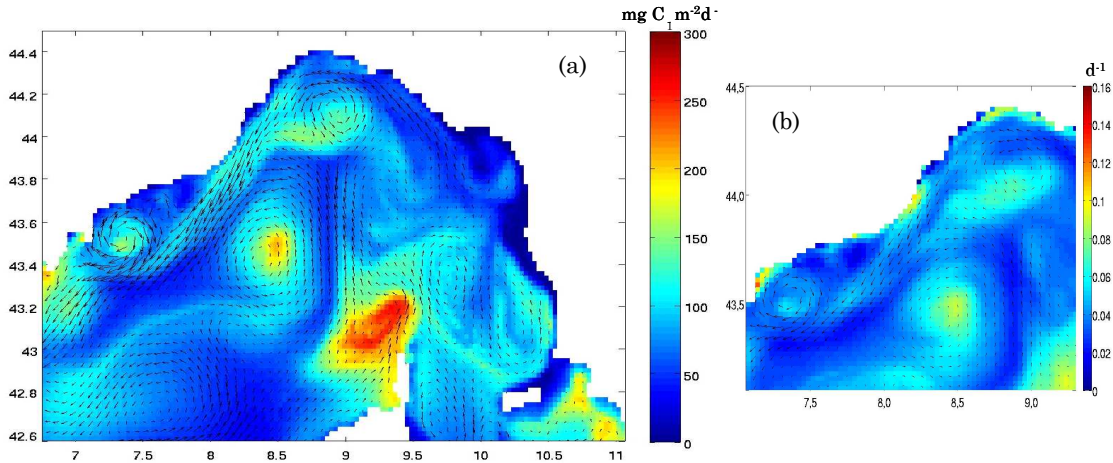


Fig. 4.8.5 (a) Integrated primary production $\text{mgCm}^{-2}\text{d}^{-1}$ (colour) and mean speed m s^{-1} (vectors), (b) ratio between integrated primary production $\text{mgChla m}^{-2}\text{d}^{-1}$ and integrated phytoplankton biomass $\text{mgChla m}^{-2}\text{d}^{-1}$ on the NW part of the domain on 150m on the 21 October 2006.

To recognize the growth area due to the presence of nutrient and light, and the accumulation area due to the transport of biomass, the ratio between integrated primary production and integrated phytoplankton biomass can be used (figure 4.8.5b). This ratio give an index of biomass growth (μ^P). Figure 4.8.5b focuses the attention on eddy structures area in the NW part of the Ligurian Sea, from 43.1° N to 44.5° N and from 7° E to 9.3° E . The figure shows a growth area in correspondence of the central and the north cyclonic eddies where the index is higher. As regard the coastal anticyclonic eddy, the index shows that its core is not a growth area but its NW boundary, close to the coast, is a small growth area probably due to the positive vertical velocity at the boundaries of the anticyclonic eddy which induce upwelling of nutrient rich water.

Focusing the attention on the central cyclonic eddy, the primary production in correspondence of its core reaches $250 \text{ mgCm}^{-2}\text{d}^{-1}$ while, in the surrounding environment, the values are about $50 \text{ mgCm}^{-2}\text{d}^{-1}$. A vertical longitudinal section, (latitude 43.483° N), along the eddy core (figure 4.8.4)

allows to detect the impact of the structure on biogeochemical variables on vertical levels.

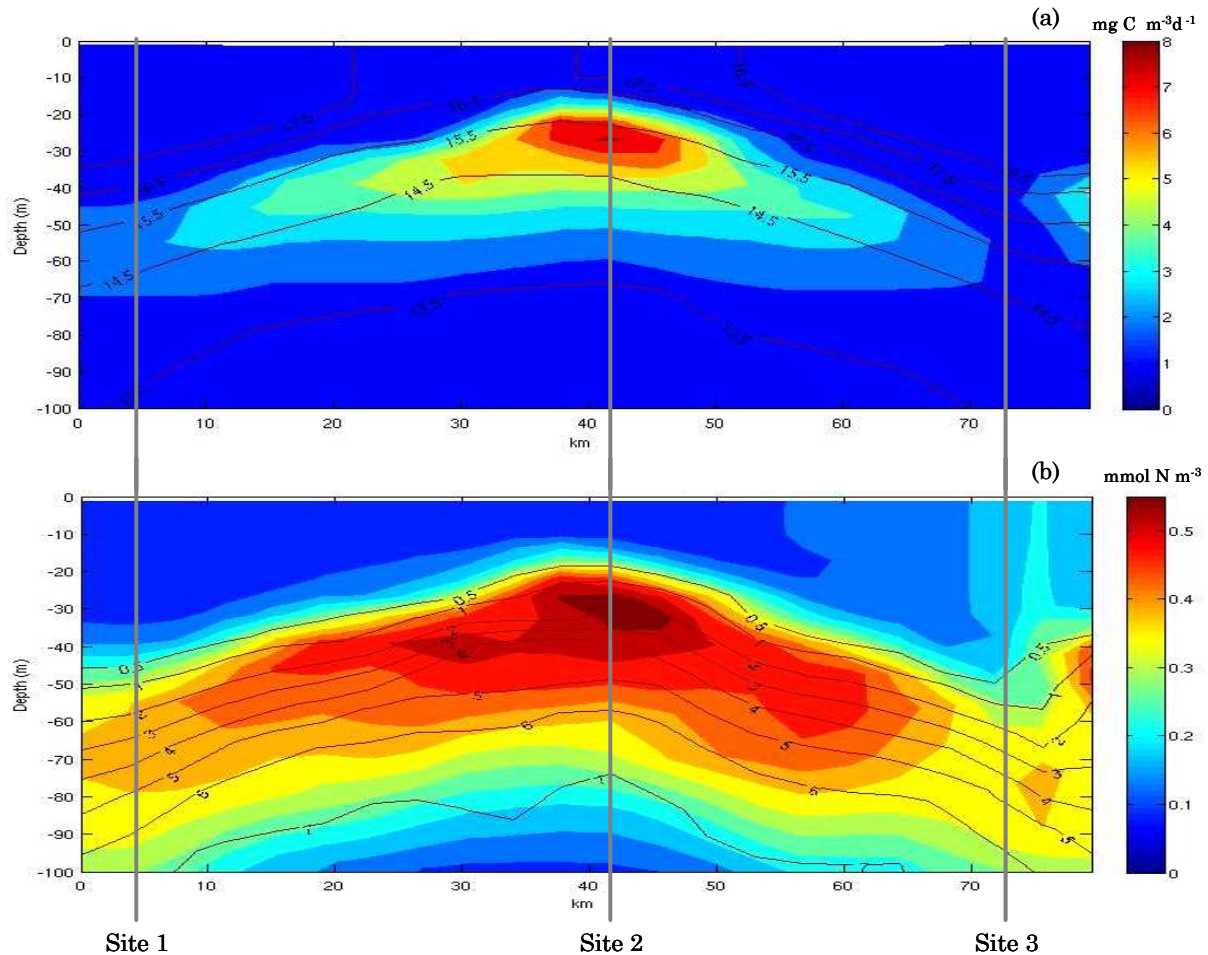


Fig. 4.8.6 Vertical longitudinal sections (latitude 43.483° N) along the eddy core of (a) primary production $\text{gCm}^{-3}\text{d}^{-1}$ (colour) and temperature $^{\circ}\text{C}$ (contour), (b) phytoplankton mmolNm^{-3} (colour) and nitrate mmolNm^{-3} (contour).

Figure 4.8.6a shows the vertical longitudinal distribution along the eddy core of primary production and temperature. The rise of the thermocline (contour line) confirms the presence of an upwelling area in correspondence of the core of the cyclonic eddy. Figure 4.8.6b shows the upwelling of nutrient rich water (contour line) in correspondence of the core of the eddy as the contour line indicates the concentration of nitrate which goes up in

correspondence of the core of the eddy. The structure described has an impact on biological production as the biomass of phytoplankton is maximum and goes up in correspondence of the core of the eddy (figure 4.8.6b, colour) and the maximum of primary production (figure 4.8.6a, colour) is located into the core of the eddy in correspondence of the upwelling area.

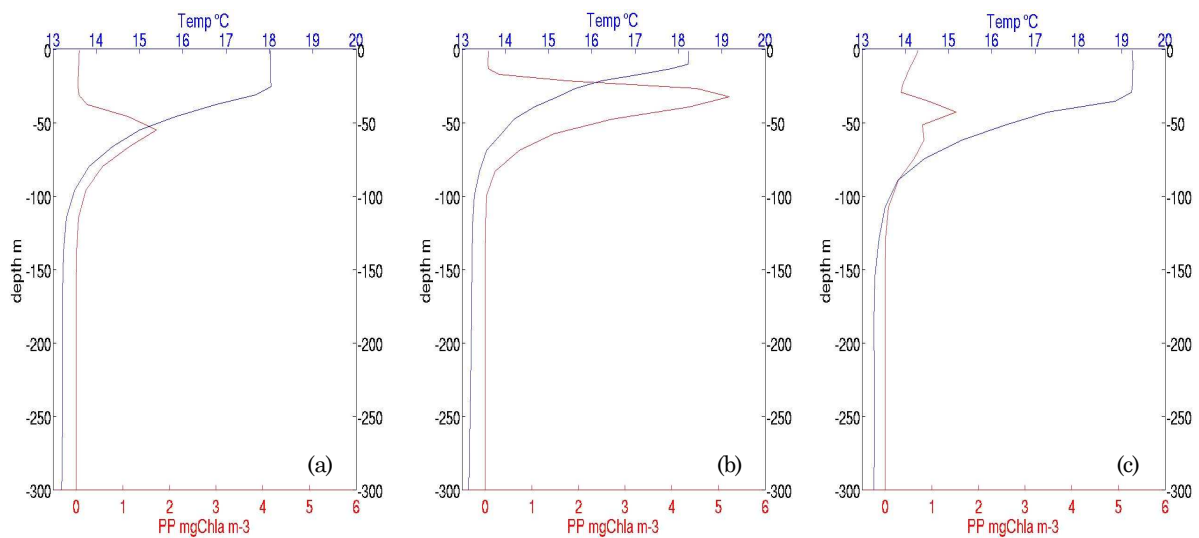


Fig. 4.8.7 Vertical profiles of temperature ($^{\circ}\text{C}$) and primary production ($\text{mgChla m}^{-3}\text{d}^{-1}$) in correspondence of (a) site 1, (b) site 2, (c) site 3 of figure 4.8.6.

To observe the effect of the eddy on vertical distribution of physical, chemical and biological distribution of properties on its boundaries and in correspondence of its core, vertical profiles of sites 1, 2 and 3 (figure 4.8.6) have been done (figure 4.8.7). Figure 4.8.7 shows the rise of the thermocline around 10-20 m in correspondence of site 2 (figure 4.8.7b), the core of the eddy, while in correspondence of its boundaries (figure 4.8.7a,c), the thermocline is around 30-40 m. Figure 4.8.7 shows higher values of primary production in correspondence of site 2 (figure 4.8.7b). The maximum of primary production is located in correspondence of the thermocline and the higher value ($5.2 \text{ mgChla m}^{-3}\text{d}^{-1}$) is reached at the depth of 30 m while at the

boundaries of the eddy it is located at the depth of 50 m with a lower value (about $2 \text{ mgChla m}^{-3}\text{d}^{-1}$).

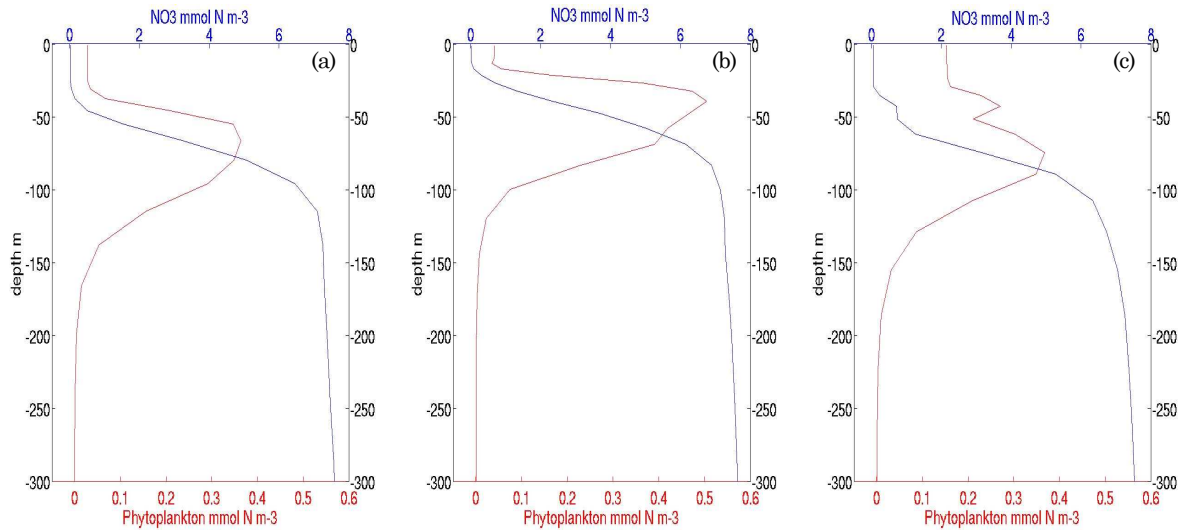


Fig. 4.8.8 Vertical profiles of nitrate (mmolNm^{-3}) and phytoplankton biomass (mmolNm^{-3}) in correspondence of (a) site 1, (b) site 2, (c) site 3 of figure 4.8.6.

The vertical profiles of nitrate and phytoplankton biomass in correspondence of sites 1, 2 and 3 are shown in figure 4.8.8. It is observable the rise of the nitracline in figure 4.8.8b which reaches 25-30 m while in figures 4.8.8a,c (at the boundaries of the eddy) it is around 50 m deep. The maximum concentration of phytoplankton biomass (0.5 mmolNm^{-3} ; $0.795 \text{ mgChla m}^{-3}$) is located in correspondence of the nitracline on site 2 (figure 4.8.8b) while at the boundaries of the eddy it is located at about 50 m with lower values.

Hereafter the analyse of an anticyclonic eddy have been done.

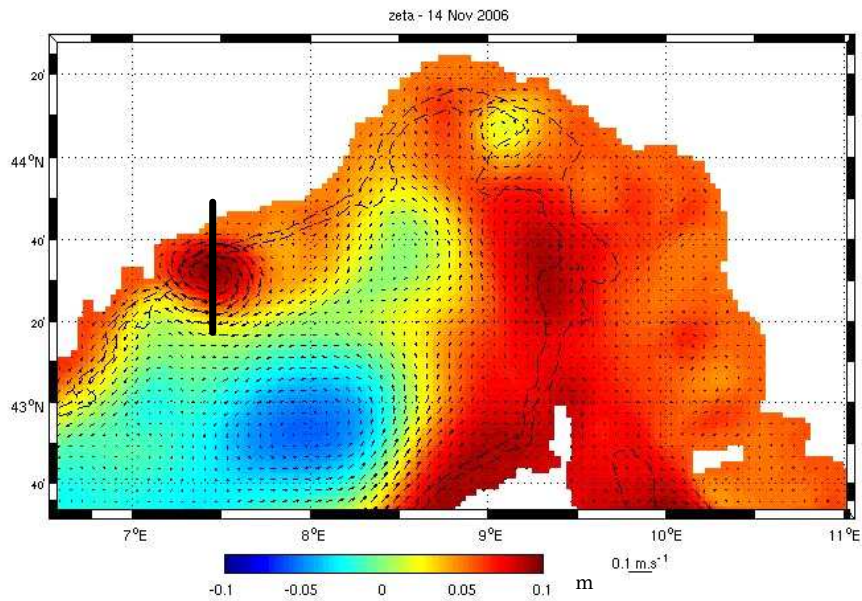


Fig. 4.8.9 SSH (colour) and current speed direction (vectors) of the 14 November 2006 of the interannual simulation.

Figure 4.8.9 shows the SSH of the 14 November of the interannual simulation which allows to detect a coastal anticyclonic eddy. The physical feature of this event have been described in section 4.5.

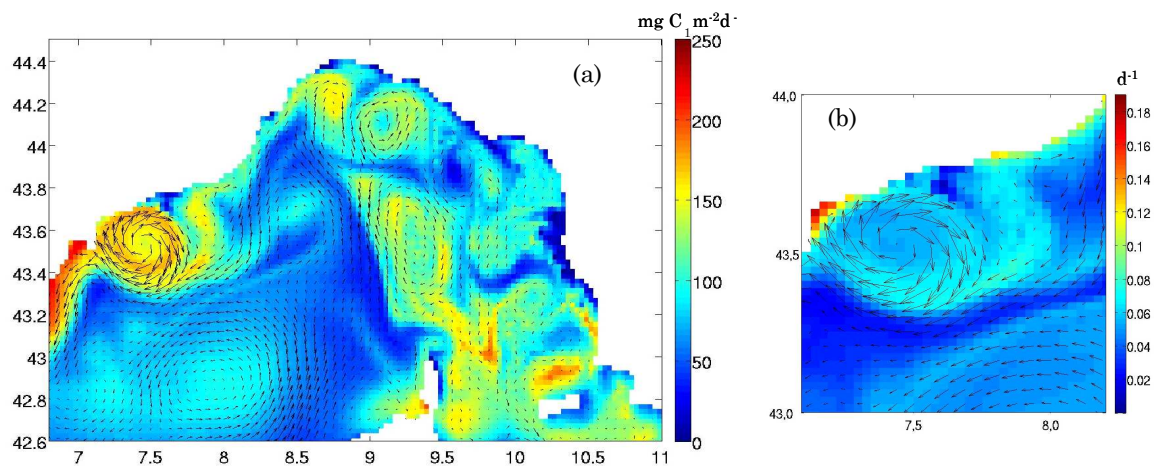


Fig. 4.8.10 (a) Integrated primary production $\text{mgCm}^{-2}\text{d}^{-1}$ (colour) and mean speed m s^{-1} (vectors), (b) ratio between integrated primary production $\text{mgChla m}^{-2}\text{d}^{-1}$ and integrated phytoplankton biomass $\text{mgChla m}^{-2}\text{d}^{-1}$ on the anticyclonic eddy on 150m on the 14 November 2006.

Figure 4.8.10a shows the integrated primary production on 150m and figure 4.8.10b shows the ratio between integrated primary production and integrated phytoplankton biomass on the anticyclonic eddy area, in the NW part of the Ligurian Sea, from 43° N to 44° N and from 7° E to 8.2° E. From these figures we can infer the anticyclonic zone is mainly an accumulation area but also, on its edges, a small production area. As described in section 4.5, on the edges of anticyclonic eddies strong positive vertical velocity have been observed in the simulation.

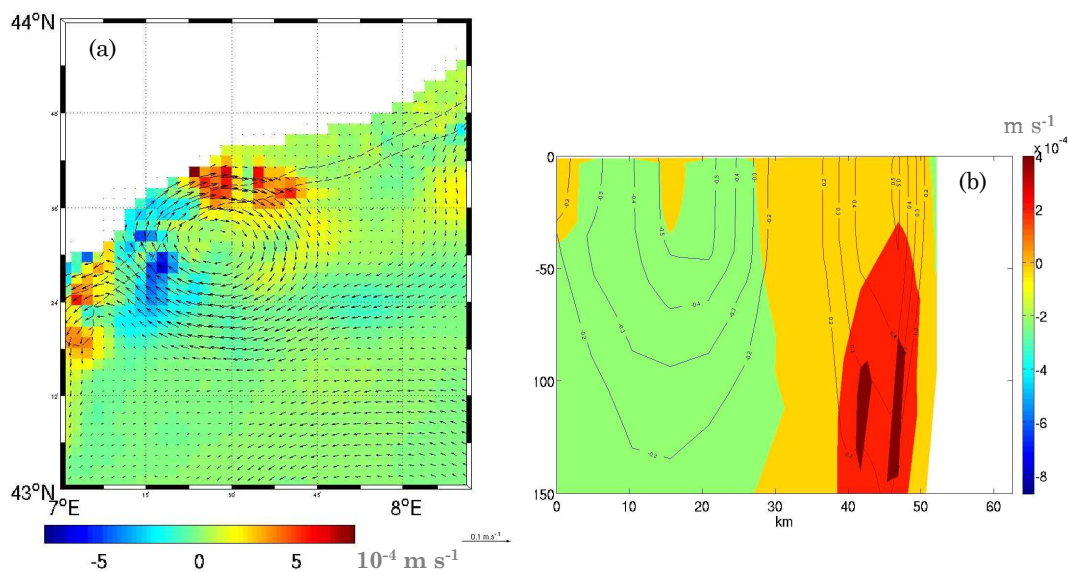


Fig. 4.8.11 (a) Horizontal section of vertical velocity m s^{-1} (colour) and horizontal speed vectors at 100 m depth on the anticyclonic eddy area. (b) Meridional section across the eddy core of vertical velocity m s^{-1} (colour) and contour line of longitudinal component of speed.

Figure 4.8.11 shows vertical velocity on (a) horizontal section at 100 m depth and (b) vertical meridional section on the eddy. From these figures it is evident the presence of positive vertical velocity ($\sim 50 \text{ m d}^{-1}$) on the coastal side of the eddy.

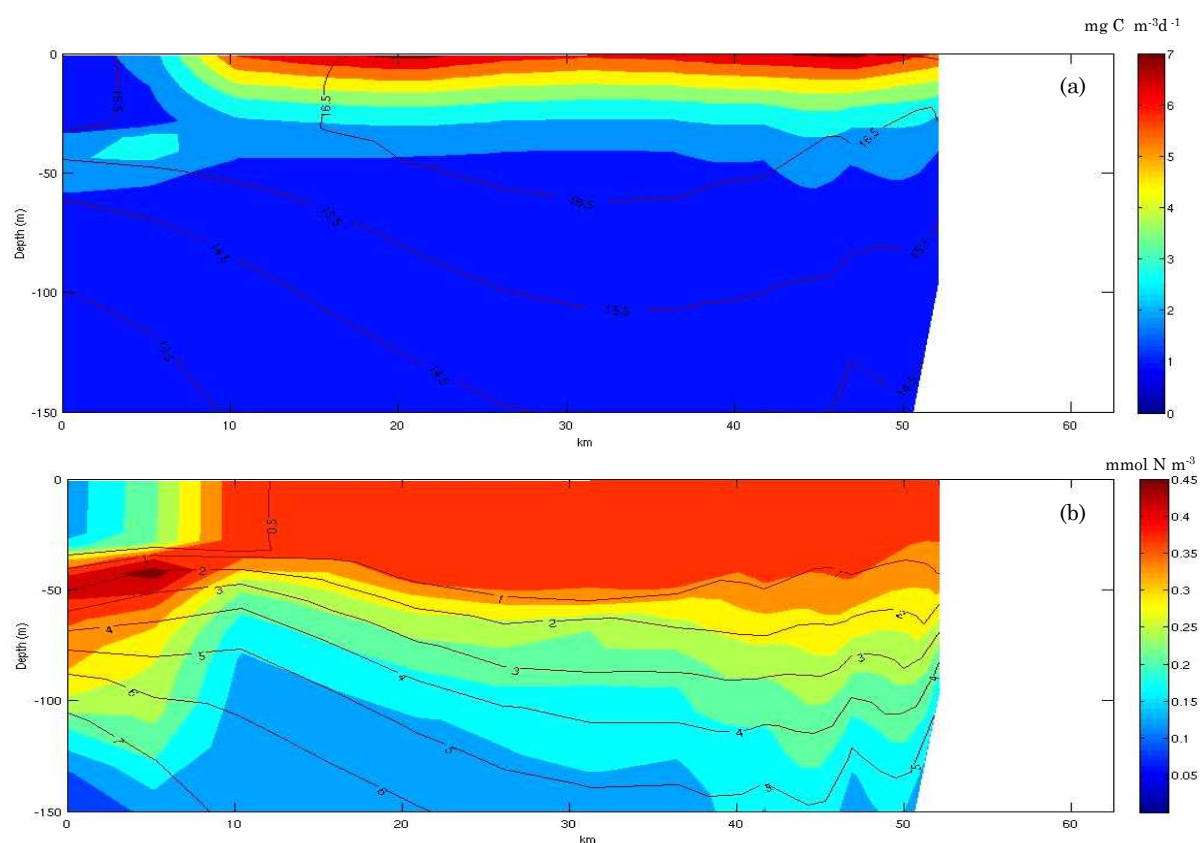


Fig. 4.8.12 Vertical meridional sections (longitude 7.44° E) along the eddy core of (a) primary production $\text{gCm}^{-3}\text{d}^{-1}$ (colour) and temperature $^{\circ}\text{C}$ (contour), (b) phytoplankton mmolNm^{-3} (colour) and nitrate mmolNm^{-3} (contour).

The behaviour of biogeochemical variables into the anticyclonic eddy, here described, is more complex than that into the cyclonic eddy analyzed before. This is due to the closeness to the coast and to the complex structure of the eddy. Figure 4.8.12 shows in the central part of the eddy a downwelling area detected through the decrease of thermocline (contour line in figure 4.8.12a) and nitracline (contour line in figure 4.8.12b). Figure 4.8.12b indicates that the anticyclonic eddy is a biomass concentration area due to the presence of a high phytoplankton biomass in the core of the eddy. Figure 4.8.12a shows a low primary production into the core of the eddy (the biomass concentration area) and a small production area on its edges where the primary production is maximum.

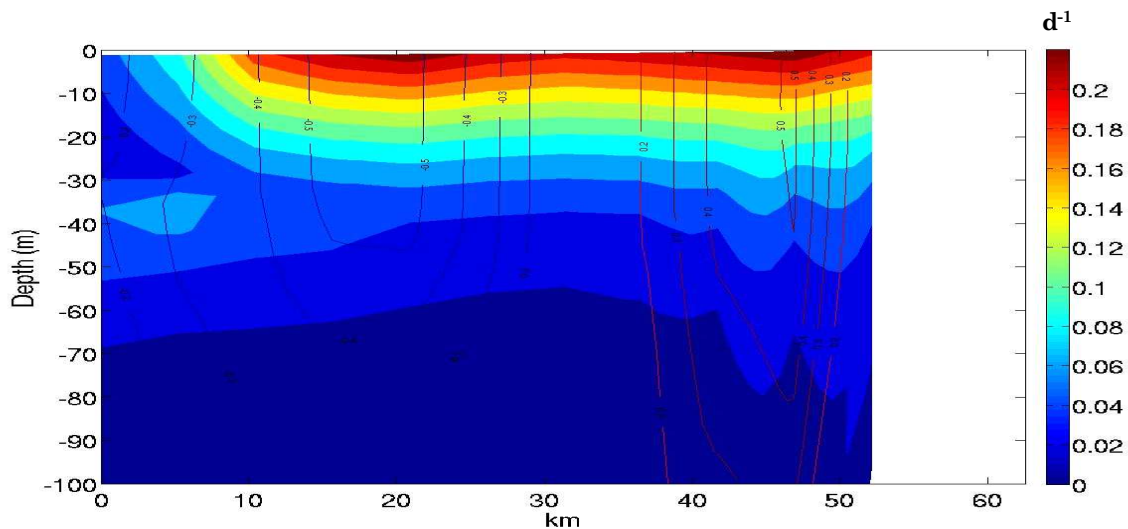


Fig. 4.8.13 Ratio between primary production $\text{mgChla m}^{-3}\text{d}^{-1}$ and phytoplankton biomass $\text{mgChla m}^{-3}\text{d}^{-1}$ on the vertical meridional section across the anticyclonic eddy.

Figure 4.8.13 shows the ratio between primary production and phytoplankton biomass along the vertical section. The index allows to recognize the growth area due to the presence of nutrient and light at the edges of the eddy, where the index is maximum.

Summarizing, the simulations have allowed to detect high primary production areas in the whole domain and biomass growth areas and biomass concentration area in correspondence of particular structures. In particular, the two runs (climatology and interannual) show satisfactory values of primary production since they are comparable with observations. The interannual simulation shows globally higher values of primary production than the one into the climatology run and a greater variability due to the different hydrodynamic. The interannual run is more dynamic and simulates more structures, which have an impact on biogeochemical variables. The behaviour of biogeochemical variables in presence of structures is complex and it depends on the particular type of structure. Both cyclonic and anticyclonic eddies have an impact on the behaviour of biogeochemical variables. The cyclonic eddies are essentially biomass growth areas since there is a marked nutrient rich water upwelling,

simulated by the model, in their core. Also anticyclonic eddies can present biomass growth areas on their edges due to the strong positive vertical velocity, which bring nutrient rich water into the euphotic layer in the boundaries of the structure.

4.9 Model evaluation

In this section an evaluation of the physical and biogeochemical models results with measured *in situ* data by ISMAR-CNR (Istituto di Scienze MARine – Consiglio Nazionale delle Ricerche) La Spezia cruises and satellite observation data, during the year 2006, is presented. To evaluate the physical model we compare the results with, firstly the transport measured during the year 2006 into the Corsica Channel and the time series of SST in the whole domain, and successively with the vertical distribution of temperature, salinity, nitrate and fluorescence along the Corsica Channel and the Nice-Calvi transect. Moreover, simulated and observed (from satellite) chlorophyll maps and time series are presented. The data have been collected during the MEDOCC06 Cruise from 8th June 2006 to 3rd July 2006. The MEDOCC 06 cruise carried out by ISMAR-CNR has several objectives. One of them is to define the principal circulation path and the physical-chemical-biological properties (temperature, salinity, oxygen, nutrients, dissolved organic carbon etc.) of the superficial, intermediate and deep water masses of the Western Mediterranean Sea through measurement along key sections located in the interior and at the boundaries of the basin. The Corsica channel represents an input of water and properties for the whole basin and is located, in the model, far enough from the sponge layer. The Nice-Calvi transect is located in the central part of the model domain and can give a complete information about the different hydrodynamic regimes and about the vertical distribution of the properties. The time series of satellite SST data (year 2006) has been collected from NOAA 17-18 satellite, AVHRR sensor, resolution 4 Km (Site:

<http://poet.jpl.nasa.gov>). The time series and maps of satellite chlorophyll data (year 2006) have been collected from AQUA satellite, MODIS OC5 sensor, resolution 1 Km (Site: www.ifremer.fr/nausicaa/medit). Finally the maps of SST distribution during autumn 2006 collected from the NOAA 17-18 satellite, sensor AVHRR, resolution 1 Km, (Site: www.ifremer.fr/nausicaa/medit) has been analysed in order to identify mesoscale structures which may be related to the simulated coastal anticyclonic eddies (sections 4.5 and 4.6).

The transport on the Corsica channel simulated by the LS-ROMS model has been compared with the transport measured *in situ* and with the transport simulated by the MFS model.

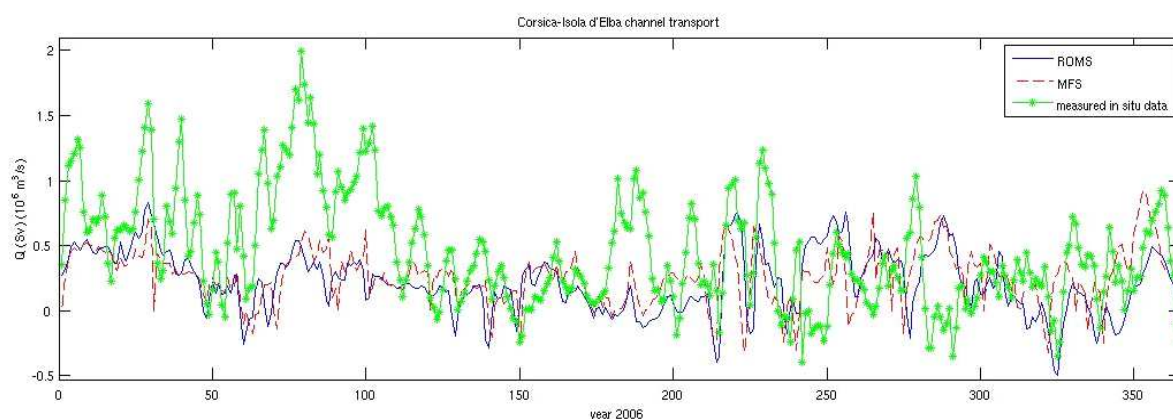


Fig. 4.9.1 Comparison between transport (Sverdrup, $10^6 \text{ m}^3 \text{ s}$) simulated by ROMS and MFS models and transport measured *in situ* into the Corsica Channel. Year 2006.

Figure 4.9.1 shows a comparison between transport simulated by ROMS and MFS models and measured *in situ* data into the Corsica Channel during the year 2006. Both simulations are different from measured data. As ROMS is forced by the MFS2006 dataset, the transport simulated by the two models is similar. The average bias, during the year 2006, between the two models is -0.004 Sv . The simulations differs mainly from measured data in the first part of the year, from January to April, and during June where it

underestimates the measured transport while in the rest of the year the differences are smaller.

Figure 4.9.2 shows the scatter plot between observed and simulated transport. The comparison indicates that the simulation underestimates the measured transport. The average bias between the transport simulated by ROMS and the one from measured data, during the year 2006, is -0.24 Sv.

As described in section 4.3 the initials and boundaries conditions for the interannual simulation (year 2006) come mainly from output of operational models but some atmospheric fluxes (e.g. heat fluxes) come from climatological dataset. Therefore, due to the model approximation and the availability of measured data, direct quantitative comparison between measured data and simulated results is not possible.

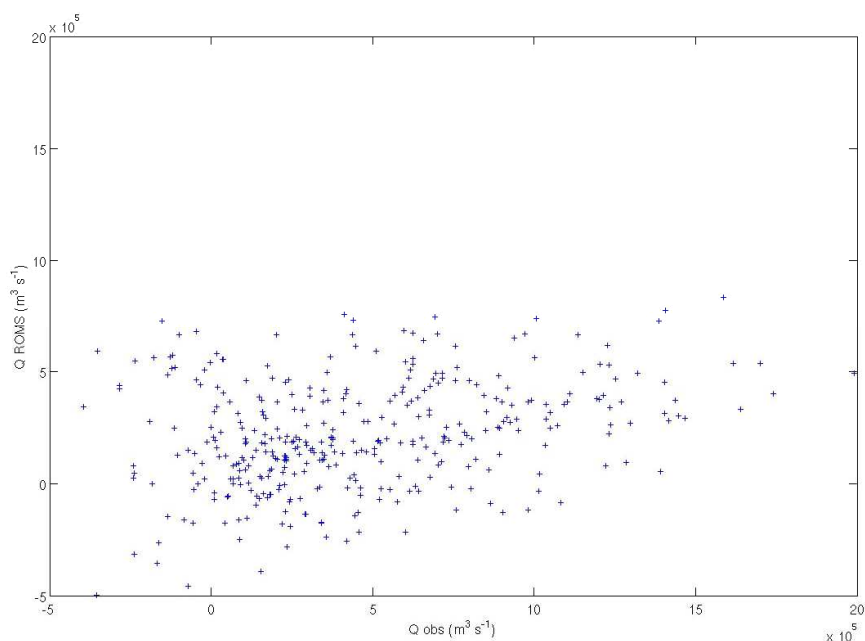


Fig. 4.9.2 Scatter plot: Comparison between transport (Sverdrup, $10^6 \text{ m}^3 \text{ s}$) simulated by ROMS model and transport measured *in situ* into the Corsica Channel. Year 2006.

Figure 4.9.3 shows a time series of the year 2006 of SST, averaged in the whole domain, simulated by LS-ROMS model and SST collected by satellite observation.

CHAPTER 4: RESULTS

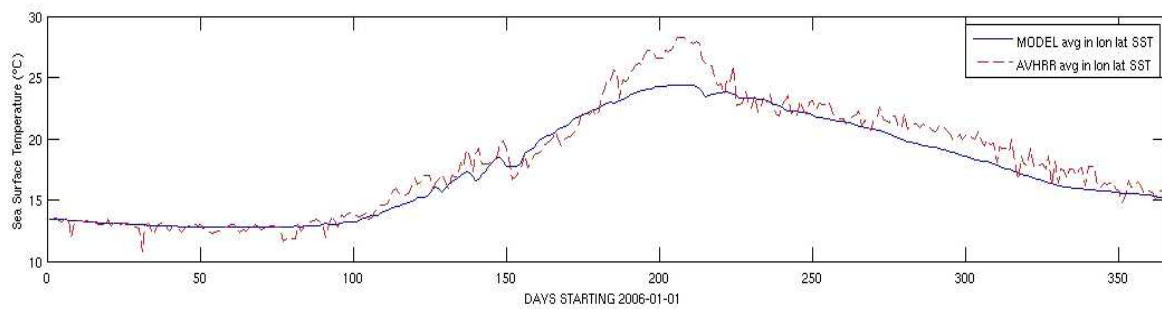


Fig. 4.9.3 Comparison between SST ($^{\circ}\text{C}$) simulated by ROMS model and collected by AVHRR-SST sensor averaged in longitude and latitude of the domain of the study area. Time series of the year 2006.

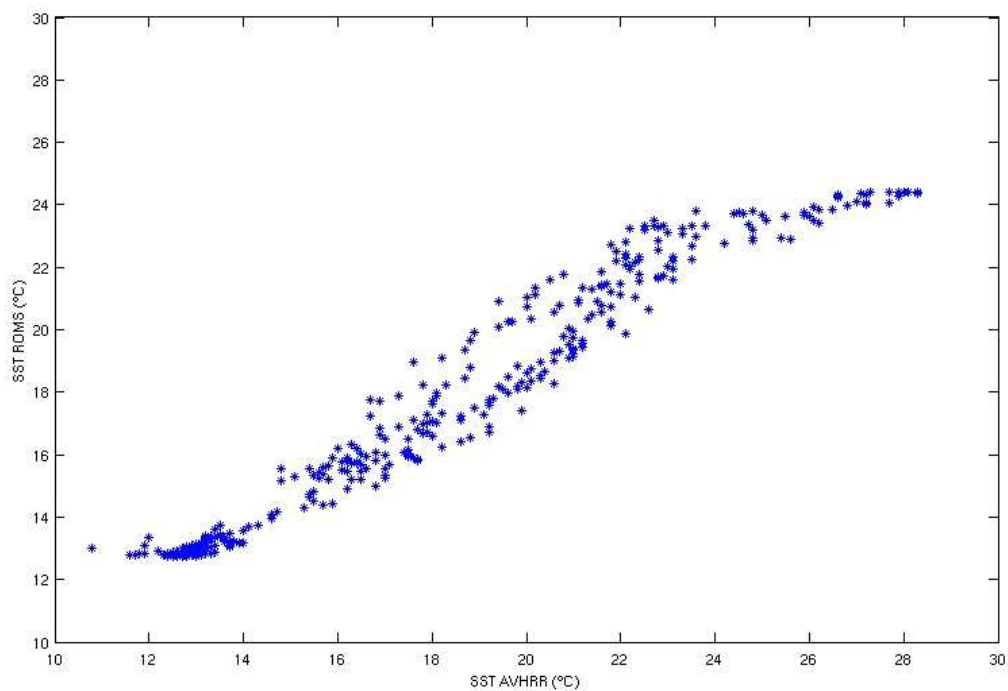


Fig. 4.9.4 Scatter plot: Comparison between SST ($^{\circ}\text{C}$) simulated by ROMS model and collected by AVHRR-SST sensor averaged in longitude and latitude of the domain of the study area. Year 2006.

Figures 4.9.3 and 4.9.4 indicate that there is a good correlation between the simulated and observed SST. In the first months of the year the correlation is very good, during July and August the model underestimates the SST and after the summer period the correlation is again good. The summer peak of SST is peculiar to the year 2006 and it mainly depend on the solar radiation.

CHAPTER 4: RESULTS

As regard solar radiation, the LS-ROMS model is forced by COADS dataset. Since a climatology dataset can't provide a peculiar situation of a particular year, the model can't simulate the peculiarity but notwithstanding it simulates the peak of SST in the same period of the observation.

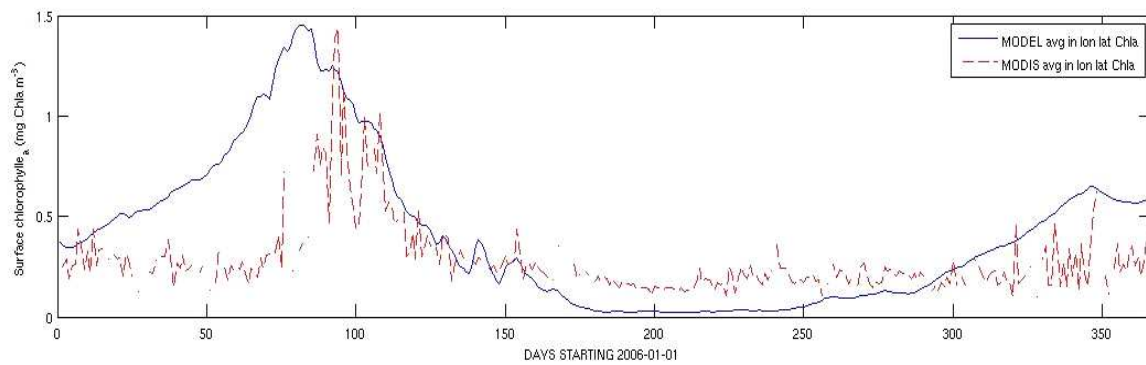


Fig. 4.9.5 Comparison between chlorophyll (mg Chla m⁻³) simulated by ROMS model and collected by MODIS sensor averaged in longitude and latitude of the domain of the study area. Time series of the year 2006.

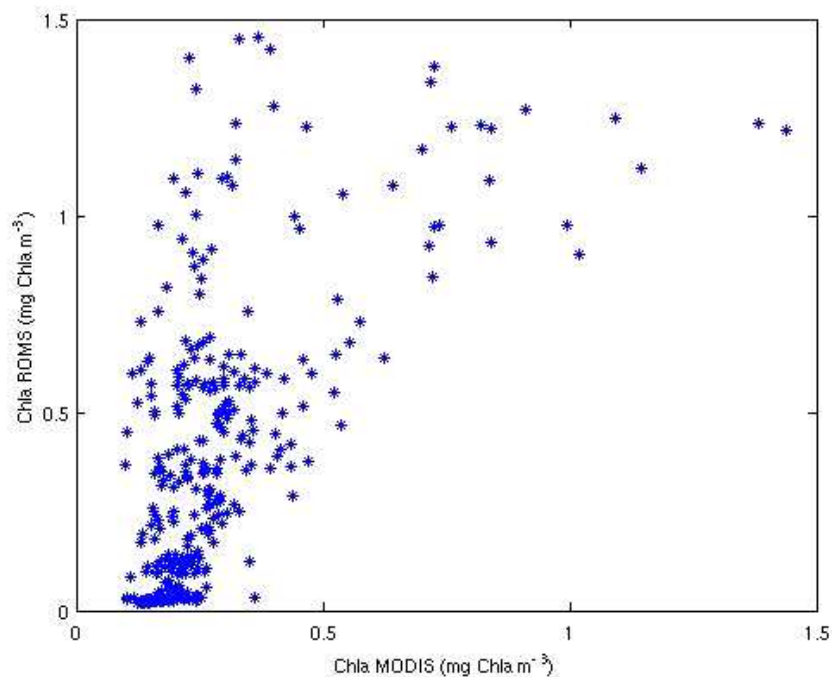


Fig. 4.9.6 Scatter plot: Comparison between chlorophyll (mg Chla m⁻³) simulated by ROMS model and collected by MODIS sensor averaged in longitude and latitude of the domain of the study area. Year 2006.

Figure 4.9.5 shows a comparison between chlorophyll simulated by LS-ROMS model and collected by MODIS sensor averaged in longitude and latitude of the domain of the study area. It is a time series of the year 2006. The observed and measured surface chlorophyll are not well correlated (figures 4.9.5 and 4.9.6) but the order of magnitude of the values and the maximum values are comparable. Besides, the peaks of chlorophyll showed in figure 4.9.5 are in the same period. The model overestimates the surface chlorophyll concentration in the first part of the year and the first simulated peak (spring bloom) anticipates the real bloom. To discuss the reason of these differences we have to consider several points.

1) The model considers a fix ration of C/Chla. In reality, the C/Chla ratio has a considerable variation, in particular in the surface layer. Moreover, it depends on the phytoplankton species, on the concentration of nutrients and on the solar radiation flux. In general, diatoms have C/Chla ratios weaker than small phytoplankton (e.g. flagellates). Diatoms are found during the spring bloom and during autumn (secondary bloom) while during the rest of the year small phytoplankton dominates.

In the model we consider a single compartment of phytoplankton (diatoms): this leads to low C/Chla ratios, and consequently to high concentration of chlorophyll.

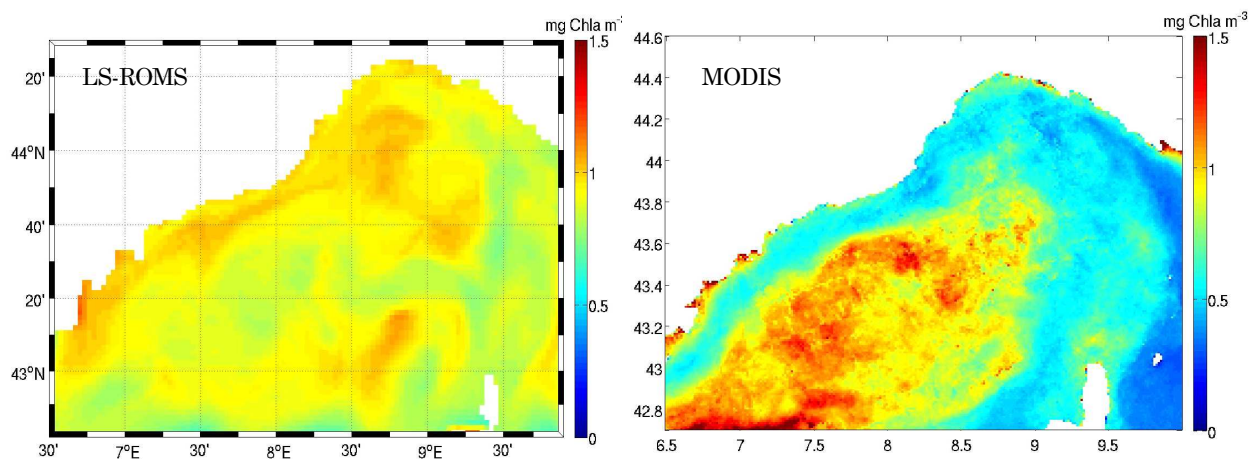


Fig. 4.9.7 Comparison between simulated (LS-ROMS) and observed (MODIS) surface chlorophyll (mg Chla m^{-3}) monthly mean of April 2006.

2) Moreover, higher solar radiation causes an increase of C/Chla, then low values of chlorophyll. The solar radiation flux contained into COADS dataset has, in general, lower values than observed values which cause high values of chlorophyll.

3) The April monthly mean surface distribution of observed chlorophyll (figure 4.9.7) shows a lower chlorophyll concentration in correspondence of the Northern Current. This is not simulated by the LS-ROMS model since the nitrate boundary condition does not take into account the real characteristics of the inflow currents.

The nitrate initial and boundary conditions for the LS-ROMS model come from the DYFAMED site, making substantially an error of positioning since the nitrate collected at the DYFAMED station have been positioned at the boundary of the LS-ROMS model.

In the following part of the section, the vertical distribution of temperature, salinity, nitrate and fluorescence along the Corsica Channel and the Nice-Calvi transect measured during the MEDOCC06 Cruise is qualitatively compared with the simulated results. The properties along the Corsica transect have been collected during the 1st July 2006. The Corsica transect is defined from 43.025°E and 9.525°N to 43.031°E and 10.437°N. Due to the model approximation we decided to qualitatively compare the measured transect data with the averaged July values simulated by the LS-ROMS model.

Figure 4.9.8 shows a comparison between measured *in situ* and simulated temperature and salinity along the Corsica transect. Figures 4.9.8a,c show the vertical distribution of temperature. In both figures the thermocline is located in the first 80m and the distribution of temperature is similar. The bottom temperature is between 13°C and 13.4 °C and the surface temperature reaches 24°C in both cases.

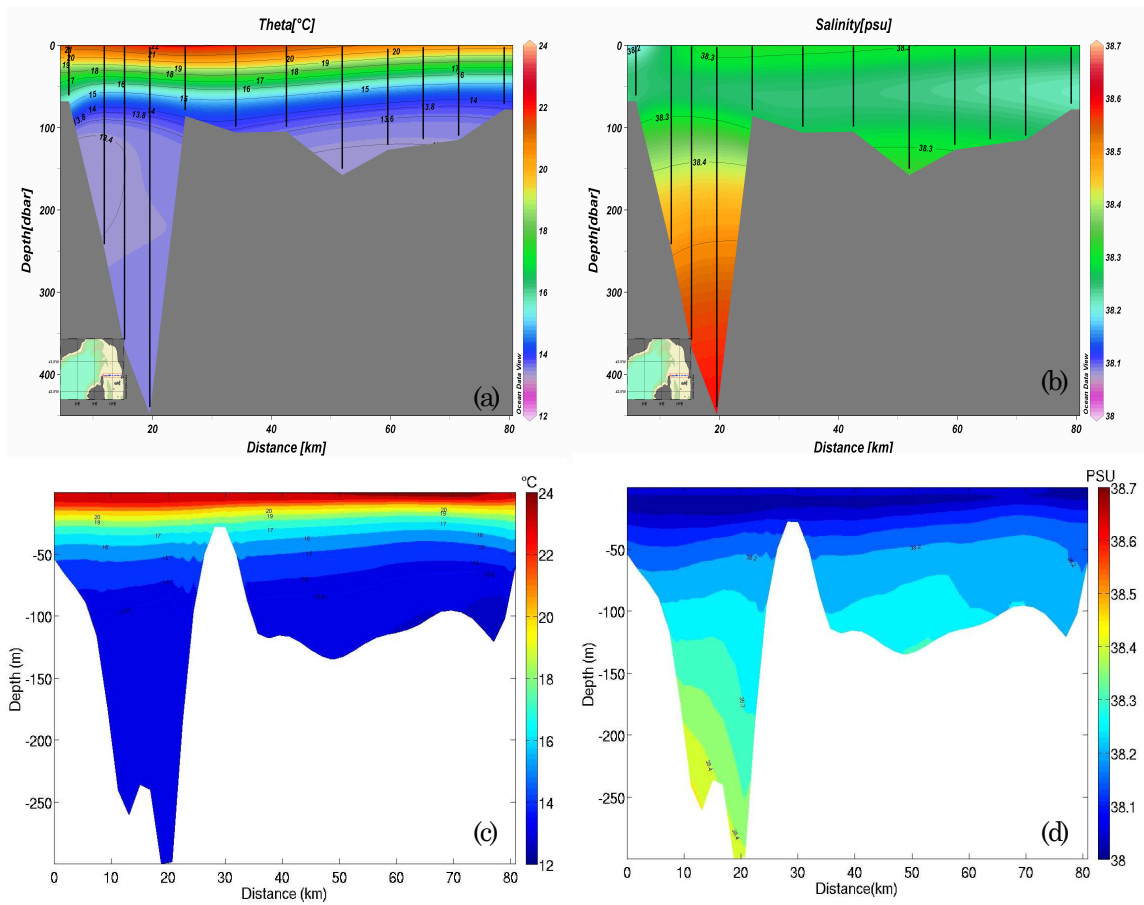


Fig. 4.9.8 Comparison between (a) (b) measured *in situ* temperature and salinity and (c) (d) simulated temperature and salinity along the Corsica transect.

Figures 4.9.8b,d show the vertical distribution of salinity. Here the simulation has lower values than measured data due to the forcing files. The bottom value of measured data is about 38.7 psu while the simulated one is about 38.4 psu. In the first layers the measured data is about 38.3 psu while the simulated one is about 38 psu.

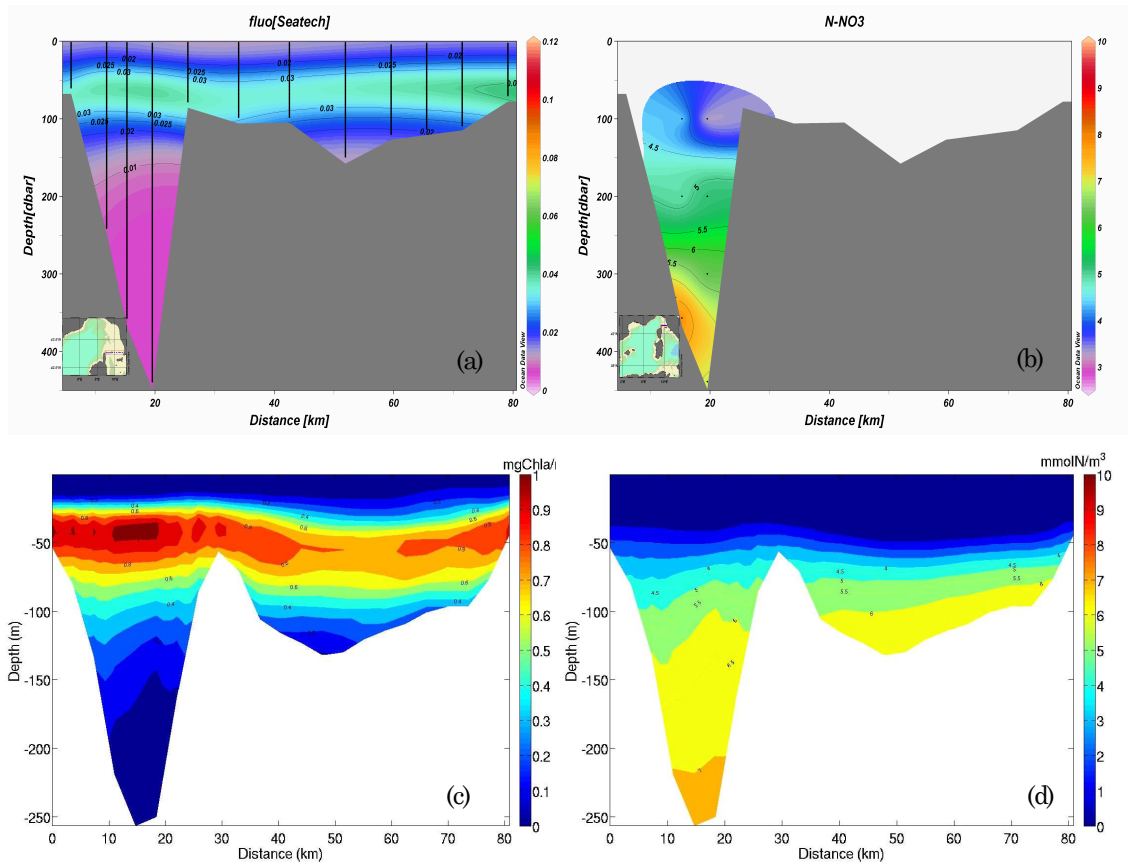


Fig. 4.9.9 Comparison between (a) (b) measured *in situ* fluorescence and nitrate and (c) (d) simulated phytoplankton biomass and nitrate along the Corsica transect.

Figure 4.9.9 shows the comparison between measured *in situ* fluorescence and nitrate and simulated phytoplankton biomass and nitrate along the Corsica transect. Fluorescence is an index of phytoplankton biomass, it is detected by the fluorescence sensor on the CTD system and analysed with the spectrophotometer in laboratory. It can give an index of the qualitative distribution of phytoplankton biomass. Figures 4.9.9a and c show a higher phytoplankton biomass concentration in the subsurface layers. The simulation shows a maximum of phytoplankton biomass between 30m and 70m of depth and the measured data shows a maximum at about the same depth (figure 4.9.9a). Figures 4.9.9b and d show the distribution of measured and simulated nitrate, respectively. We have not measured data in the first 80m. The distribution of simulated nitrate is similar to the

CHAPTER 4: RESULTS

measured one. At about 100m depth the value of nitrate is between 4 and 4.5 mmolN m⁻³, at the bottom it riches 7 mmolN m⁻³ in both cases.

The properties along the Nice-Calvi transect have been collected during the second half of June. The Nice-Calvi transect is defined from 43.753°E and 7.657°N to 42.621°E and 8.726°N. Due to the model approximation we decided to qualitatively compare the measured transect data with the averaged June value of properties simulated by the LS-ROMS model.

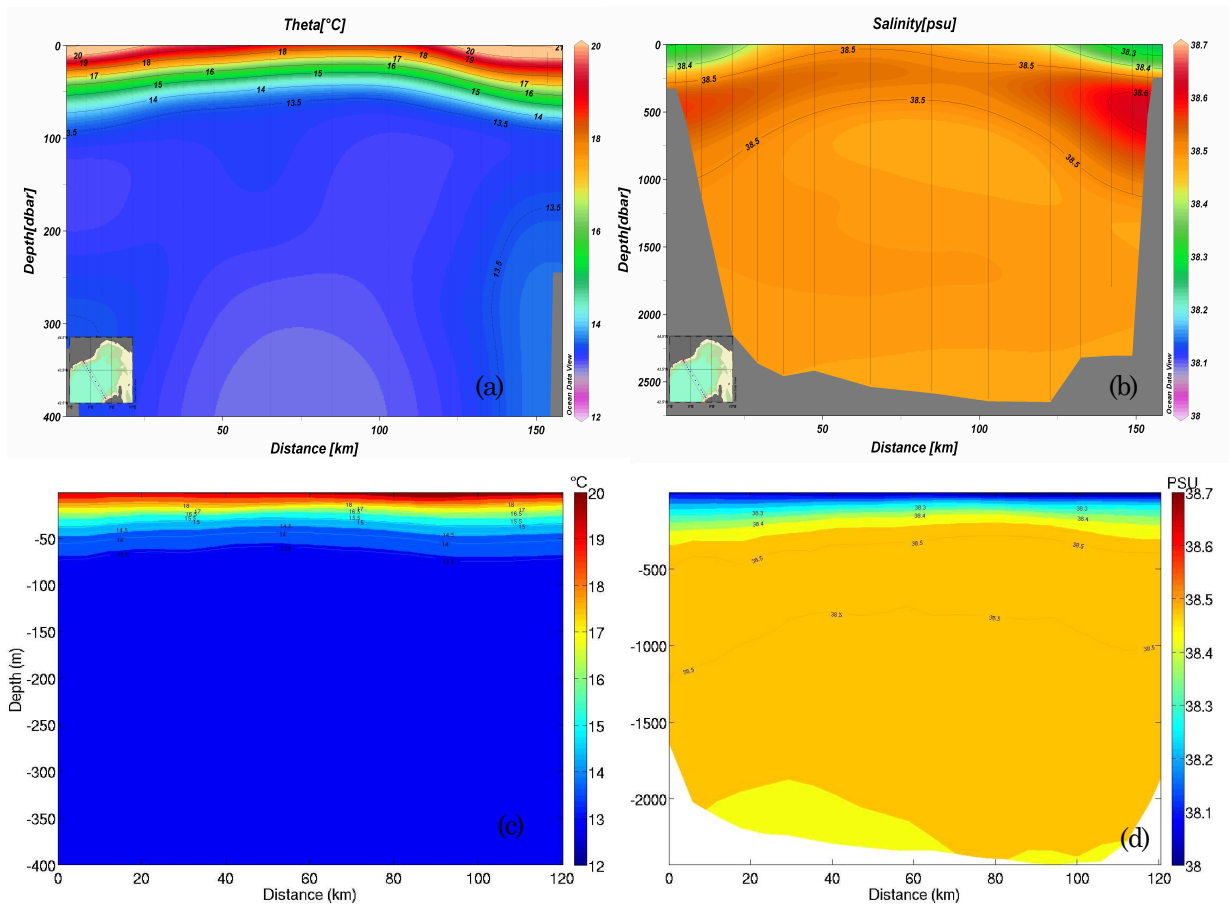


Fig. 4.9.10 Comparison between (a) (b) measured *in situ* temperature (first 400m) and salinity and (c) (d) simulated temperature (first 400m) and salinity along the Nice-Calvi transect.

Figure 4.9.10 shows a comparison between measured *in situ* and simulated temperature and salinity along the Nice-Calvi transect. Figures 4.9.10a,c show the vertical distribution of temperature. The thermocline is located, in

both figures, in the first 80m with temperature from 13.5°C to 20°C in the surface layer. Figures 4.9.10b,d show the vertical distribution of salinity. The model simulates values of salinity lower than measured data values probably due to the forcing files. Higher values of salinity are located in figure 4.9.10b in correspondence of the Levantine water layer. Measured temperature and salinity data show an upwelling area in the central part of the basin which is not simulated by the mean June values of the model. The properties of the Levantine water are observable in the simulation during the less stratified period. The distribution of temperature and salinity simulated show the presence of Levantine water between 200m and 600m.

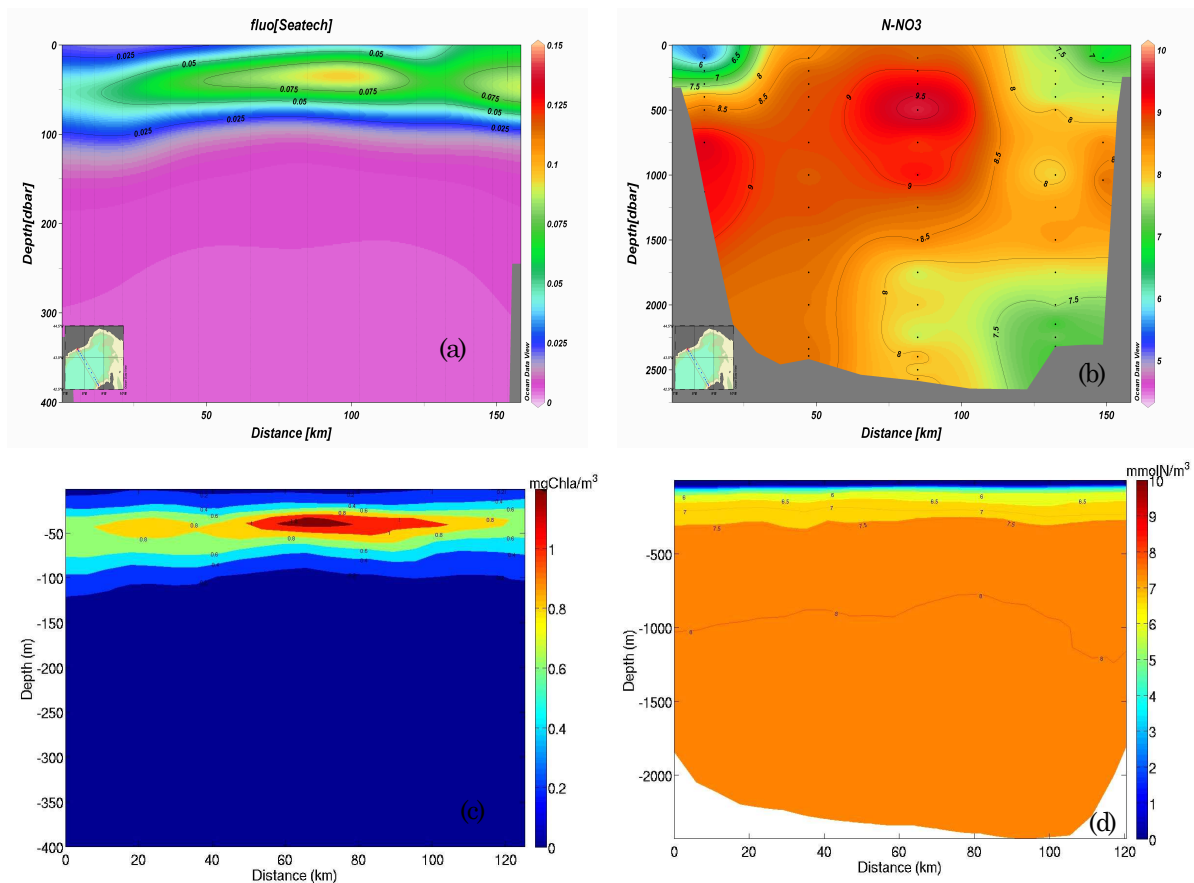


Fig. 4.9.11 Comparison between (a) (b) measured *in situ* fluorescence (first 400m) and nitrate and (c) (d) simulated phytoplankton biomass (first 400m) and nitrate along the Nice-Calvi transect.

Figure 4.9.11 shows a qualitative comparison between measured *in situ* fluorescence and nitrate and simulated phytoplankton biomass and nitrate along the Nice-Calvi slice. Figures 4.9.11c shows the vertical distribution of phytoplankton biomass simulated while figure 4.9.11a shows the vertical distribution of fluorescence (index of biomass) measured. It is observable, in both figures, that the maximum concentration of biomass is located between 20m and 100m depth. Figures 4.9.11b,d show the vertical distribution of nitrate. The simulation shows a distribution more homogeneous than the measured data probably due to the resolution of the model which doesn't simulate the small processes which cause the distribution. The homogeneity of the distribution of simulated nitrate is also due to the monthly mean data.

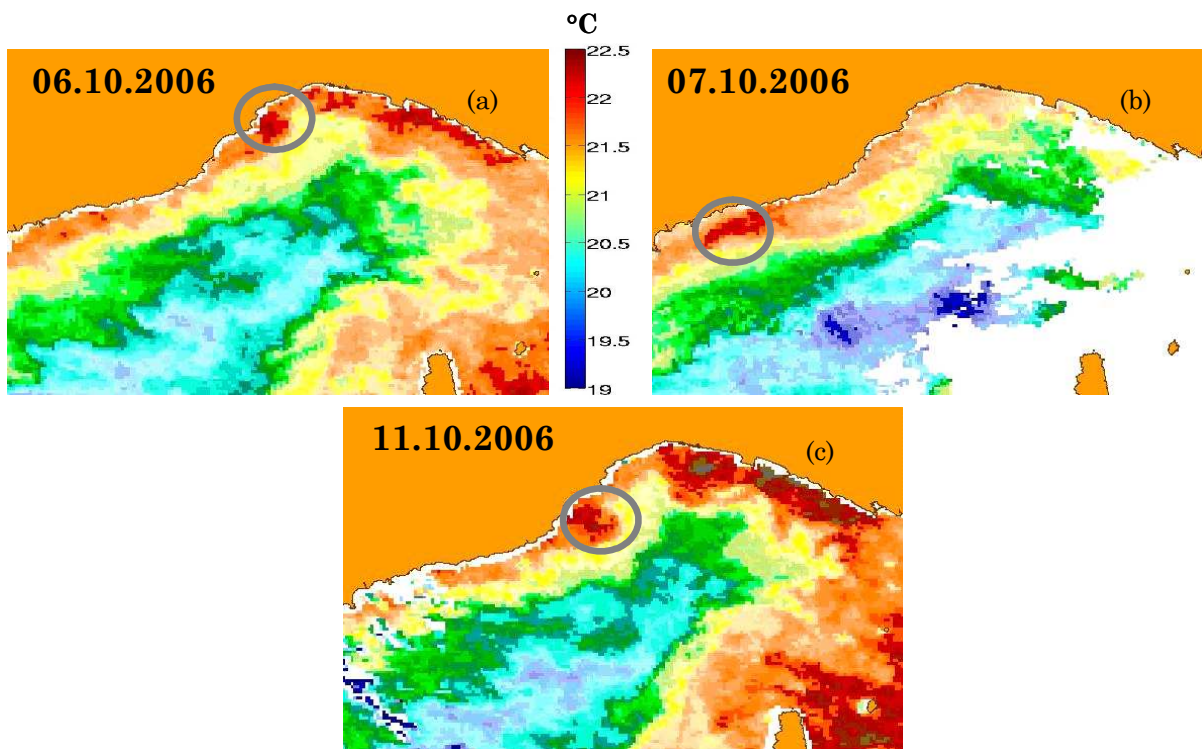


Fig. 4.9.12 SST distribution on (a) 6th (b) 7th (c) 11th October 2006. NOAA 17-18 satellite, sensor AVHRR, resolution 1 km.

In section 4.6, the simulation, by the LS-ROMS model, of intense coastal anticyclonic eddies is described. These eddies appear during the year with

an intensification in the last months of the year. As described in the section 4.6, it is possible to detect eddies thanks to the variable SST. Anticyclonic eddies have a warm core, warmer than the surround environment, due to the surface convergence. Observing the SST distribution from satellite data it is possible to detect structures with a warmer core than the surround environment (figure 4.9.12).

These structures appear during autumn 2006, in the same period of the simulation. The warm coastal cores observed in the satellite images (figure 4.9.12) may be related to the simulated coastal anticyclonic eddies, in terms of position and max temperature. However direct quantitative comparison between the satellite imagines and simulated results is not possible due to the model approximation (e.g. climatological heat fluxes).

The simple qualitative comparison presented in this section is satisfactory since the order of magnitude and the distribution of simulated variables agree with the available measured data. A perspective could be to do a new simulation completely forced with “real forcing” and to compare quantitatively the model results with observations.

5 Conclusion and perspectives

The simulation of the Liguro-Provençal-Catalan current in the Ligurian Sea with a high-resolution, primitive equation model, LS-ROMS, has revealed the presence of instabilities that lead to the formation of mesoscale and submesoscale eddies. The vortices are particularly intense when realistic winds, provided by a mesoscale meteorological model with high spatial and temporal resolution, are used to force the sea surface. By contrast, the use of climatological wind-stress forcing produces much weaker vortical structures.

With realistic wind-stress forcing, mesoscale and submesoscale eddies account for a large fraction of the mean eddy kinetic energy in the upper sea layer. In particular, one can see the formation of intense anticyclones between the current and the coast. These vortices are characterized by a long lifetime and by closed streamlines, associated with a dominance of rotation over strain. The vortices move, rather slowly, downstream with the current. By further increasing the spatial resolution of the numerical model firstly to 1 km and successively to 300m, small vorticity peaks visible also in the lower-resolution run (3 km) fully reveal their nature as a series of smaller, submesoscale cyclonic and anticyclonic vortices associated with the main vortex.

These coastal eddies are associated with a complex pattern of intense vertical velocities, as already observed in the case of open-ocean conditions (Koszalka et al., 2009), where the important role played by vortex Rossby waves and inertial waves has been addressed, and by idealized simulations of the dynamics of shallow-water eddies moving on a steep slope (Zavala Sanson and Provenzale, 2009), where the importance of vortex-generated topographic Rossby waves was discussed. In the case of the Ligurian Sea, the anticyclonic vortex induces strong upwelling at its coastal side and a

slightly less intense downwelling at the open-sea side. The vertical velocities peak at the lower edge of the vortex and at larger depths, and they can reach values of several tens of meters per day. These high values are comparable with the vertical velocities observed in proximity of frontal regions. When the spatial resolution is increased, one observes an increase in the strength of the vertical velocity field associated with the vortices.

In fact the increase of resolution allows to finely resolve the distribution of vertical velocity field which permits to observe a complex pattern of strong, alternating positive and negative vertical velocities in correspondence of the eddy structure. For horizontal velocities, the increase of resolution has not a noticeable impact on its intensity and distribution which means that the process is sufficiently solved by the low resolution model. As regard temperature, it can give information about the presence and the structure of the eddies. The SST collected by satellite can give information about the presence of warm coastal core which can be anticyclonic eddies.

The strong vertical velocities associated with the vortices can play a significant role for the dynamics of the marine ecosystem in the Ligurian Sea. Owing to the cyclonic circulation of the Liguro-Provençal-Catalan current, in the absence of vortices downwelling conditions prevail, with an associated lack of nutrient input into the euphotic layer. However, the anticyclonic eddies trapped between the current and the coastline induce localized upwelling at their coastal side, thus providing a source of nutrients to the surface layer and possibly inducing an intermittent fertilization of the Ligurian Sea. The fact that these eddies are long-lived and almost trapped further enhances the effect, as they function as localized, long-lived pumps of nutrients. A biogeochemical model coupled with the physical circulation model can help in detecting the impact of mesoscale structures on biological production.

The results provided by the biogeochemical model evidence that the behaviour of biogeochemical variables in presence of structures is complex and it depends on the particular type of structure. Both cyclonic and anticyclonic eddies have an impact on the behaviour of biogeochemical variables. The cyclonic eddies are essentially biomass growth areas since there is a marked nutrient rich water upwelling, simulated by the model, in their core. As regard coastal anticyclonic eddies, they represent a concentration site due to the transport of properties but also they can present biomass growth areas on their edges due to the strong positive vertical velocity, which bring nutrient rich water into the euphotic layer at the boundaries of the structure.

The results reported in this work indicate the importance of mesoscale and submesoscale processes, the impact of these processes on biological production and the need for adopting high spatial and temporal resolution both in the simulation model and in the surface forcing.

This work has several perspectives. One is to introduce the biogeochemical model into the high - resolution LS-ROMS model to study the impact of the large, eddy-induced vertical velocities on biological production. This procedure should be aimed at verifying whether the eddy-induced fertilization is a significant component of the overall nutrient budget in the Ligurian Sea. High-resolution simulations with a full biogeochemical model would allow for assessing what is the relative importance of vortex-induced upwelling versus local nutrient regeneration by bacteria in the euphotic layer (see, e.g., Allen et al., 2002).

A future perspective could also be the use of high-resolution coastal ROMS simulations to study contaminant and/or sediment displacement to identify,

CHAPTER 5: CONCLUSION AND PERSPECTIVES

in a particular area, vulnerable targets which can be damaged in case of release of high concentrations of contaminant or sediment.

BIBLIOGRAPHY

Abraham, E., 1998. The generation of plankton patchiness by turbulent stirring. *Nature*. 391, 577-580.

Ahumada, M. A., Cruzado, A., 2007. Modeling of the circulation in the Northwestern Mediterranean Sea with the Princeton Ocean Model. *Ocean Science*, 3, 77-89.

Allen JI, Eknes M, Evensen G, 2002. An Ensemble Kalman Filter with a complex marine ecosystem model: hindcasting phytoplankton in the Cretan Sea. *Annal Geophys* 20: 1–13.

Allen, J.I., Somerfield, P.J., Siddorn, J., 2002. Primary and bacterial production in the Mediterranean Sea: a modelling study. *J. Marine Syst.* 33-34, 473-495.

Andersen, V., Nival, P., 1988. Modèles d'écosystèmes pélagiques des eaux côtières de la mer ligure. *Oceanologica Acta* SN9, 211–217.

Astraldi, M., & Gasparini, G. P., 1992. The seasonal characteristics of the circulation in the north Mediterranean basin and their relationship with the atmospheric-climatic conditions. *Journal of Geophysical Research*, 97, 9531–9540.

Astraldi, M., Gasparini, G.P., Sparnocchia, S., 1994. The seasonal and interannual variability in the Ligurian–Provencal Basin. In: LaViolette, P.E.Ed., *Seasonal and Interannual Variability of the Western Mediterranean Sea, Coastal and Estuarine Studies*, Vol. 46. AGU, Washington, pp. 93–114.

Barlow, R.G., Mantoura, R.F.C., Cummings, D.G., Fileman, T.W., 1997. Pigment chemotaxonomic distributions of phytoplankton during summer in the western Mediterranean. *Deep-Sea Research Part II* 44, 833–850.

Beckers J. M., 1991. Application of the GHER 3D general circulation model to the western Mediterranean, *J. Mar. Syst.*, 1, 315–322.

Beckers, J. M., Rixen, M., Brasseur, P., Brankart, J. M., El moussaoui, A., Crépon, M., Herbaut, Ch., Martel, F., Van den Berghe, F., Mortier, L., Lascaratos, A., Drakopoulos, P., Korres, G., Nittis, K., Pinardi, N., Masetti, E., Castellari, S., Carini, P., Tintoré, J., Alvarez, A., Monserrat, S., Parrilla, D., Vautard, R., and Speich, S., 2002. Model intercomparison in the

Mediterranean: MEDMEX simulations of the seasonal cycle, *J. Mar. Syst.*, 33–34, 215–251.

Bergametti, G., Remoudaki, E., Losno, R., Steiner, E., Chatenet, B., Buat-Ménard, P., 1992. Source, transport and deposition of atmospheric phosphorus over the northwestern Mediterranean. *Journal of Atmospheric Chemistry* 14, 501–513.

Béthoux, J. P., & Copin-Montegut, G., 1988. Phosphorus and nitrogen in the Mediterranean sea: specificities and forecasting. *Oceanologica Acta* 5, 75–78.

Béthoux, J.P., Morin, P., Chaumery, C., Connan, O., Gentili, B., Ruiz-Pino, D., 1998. Nutrients in the Mediterranean Sea, mass balance and statistical analysis of concentrations with respect to environmental changes. *Marine Chemistry* 63, 155–169.

Béthoux, J.P., Gentili, B., Morin, P., Nicolas, E., Pierre, C., Ruiz-Pino, D., 1999. The Mediterranean Sea: a miniature ocean for climatic and environmental studies and a key for climatic functioning of the North Atlantic. *Progress in Oceanography*, 44, 131-146.

Blanke, B., Roy, C., Penven, P., Speich, S., McWilliams, J.C., Nelson, G., 2002. Linking wind and upwelling interannual variability in a regional model of the southern Benguela, *Geophysical Research Letters* 29, 2188-2191.

Boucher, J., Ibanez, F., Prieur, L., 1987. Daily and seasonal variations in the spatial distribution of zooplankton population in relation to the physical structure in the Ligurian Sea *Front. J. mar. Res.* 45: 133-173.

Bracco, A., LaCasce, J., and Provenzale, A., 2000. Velocity probability density functions for oceanic floats. *Journal of Physical Oceanography*. 30, 461.

Bracco, A., Chassignet, E.P., Garraffo, Z.D., and Provenzale, A., 2003. Lagrangian velocity distribution in a high-resolution numerical simulation of the North Atlantic, *Journal of Atmospheric and Oceanic Technology*. 20, 1212-1220.

Brankart, J. M. and Brasseur, P., 1998. The general circulation in the Mediterranean Sea: a climatological approach, *J. Mar. Syst.*, 18, 41–70.

Bustillos-Guzman, J., Claustre, H., Marty, J.C., 1995. Specific phytoplankton signatures and their relationship to hydrographic conditions in the coastal northwestern Mediterranean Sea. *Marine Ecology Progress Series* 124, 247–258.

Claustre, H., Kerhervé, P., Marty, J.C., Prieur, L., 1994a. Phytoplankton photoadaptation in relation to some frontal physical processes. *Journal of Marine Systems* 5, 251–265.

Coste, B., Le Corre, P., Minas, H.J., 1988. Re-evaluation of the nutrient exchanges in the Strait of Gibraltar. *Deep-Sea Research* 35, 767–775.

Da Silva, A.M., Young, C.C., Levitus, S., 1994. Atlas of surface marine data 1994. Volume 1: algorithms and procedures. Technical Report NOAA Atlas NESDIS 6, National Oceanic and Atmospheric Administration, Washington, DC.

Debreu, L., Blayo, E., 2003. AGRIF: Adaptive Grid Refinement In Fortran. Submitted to *ACM Transactions on Mathematical Software—TOMS*.

Debreu, L., Vouland, C., 2003. AGRIF: Adaptive Grid Refinement in Fortran. [Available online <http://wwwlmc.imag.fr/IDOPT/AGRIF/index.html>].

Demirov, E. and Pinardi, N., 2002. Simulation of the Mediterranean Sea circulation from 1979 to 1993: Part I. The interannual variability, *J. Mar. Syst.*, 33, 23–50.

Di Lorenzo, E., Miller, A.J., Neilson, D.J., Cornuelle, B.D., Moisan, J.R., 2004. Modeling observed California Current mesoscale eddies and the ecosystem response. *International Journal of Remote Sensing*.

Dugdale, R. C., 1957. Nutrient limitation in the sea: dynamics, identification and significance. *Lirnnol. Oceanogr.* 12: 685.

DYFAMED-JGOFS France. 1995. Recueil de données (Janvier 1991–Decembre 1993).

Echevin V., Crépon, M., and Mortier, L., 2002. Simulation and analysis of the mesoscale circulation in the northwestern Mediterranean Sea, *Ann. Geophys.*, 21, 281–297.

- Fairall, C. W., E. F. Bradley, D. P. Rogers, J. B. Edson, and G. S. Young, 1996a. Bulk parameterization of air–sea fluxes in TOGA COARE. *J. Geophys. Res.*, 101, 3747–3767.
- Falkowski, P., Ziemann, D., Kolber, Z., Bienfang, P., 1991. Role of eddy pumping in enhancing primary production in the ocean. *Nature*. 352, 55–58.
- Fasham, M.J.R., Ducklow, H.W., McKelvie, S.M., 1990. A nitrogen-based model of plankton dynamics in the oceanic mixed layer. *Journal of Marine Research* 48, 591–639.
- Fasham, M.J.R., Sarmiento, J.L., Slater, R.D., Ducklow, H.W., Williams, R., 1993. Ecosystem behavior at Bermuda station “S” and ocean weather station “India”: a general circulation model and observational analysis. *Global Biogeochemical Cycles* 7, 379–415.
- Fernández, V., Dietrich, D. E., Haney, R. L., and Tintoré, J., 2005. Mesoscale, seasonal and interannual variability in the Mediterranean Sea using a numerical ocean model, *Progress in Oceanography*, 1–20.
- Fogg, G.E., 1991. The phytoplanktonic ways of life. *New Phytologist* 118, 191–232.
- Franks, P. J. S., 2002. NPZ Models of Plankton Dynamics: Their Construction, Coupling to Physics, and Application. *Journal of Oceanography*, Vol. 58, pp. 379 to 387.
- Franks, P.J.S., Wroblewski, J.S. & G.R. Fried, 1986. Behaviour of a simple plankton model with food level acclimation.--*Mar. Biol.* 91; 121-129.
- Gasparini, G. P., Zodiatis, G., Astraldi, M., Galli, C., & Sparnocchia, S., 1999. Winter intermediate water lenses in the Ligurian Sea. *Journal of Marine Systems*, 20, 319–332.
- Goldman, J.C., 1993. Potential role of large oceanic diatoms in new primary production. *Deep-Sea Research* 40, 159–168.
- Grilli, F., and N. Pinardi, 1998. The computation of Rossby radii of deformation for the Mediterranean Sea. *MTP News*, 6, 4.
- Gruber N, Frenzel H, Doney SC, Marchesiello P, McWilliams JC, Mooisan JR, Oram JJ, Plattner G-K, Solzenbach KD, 2006. Eddy-resolving

simulation of plankton ecosystem dynamics in the California Current System. *Deep-sea Res 1, Oceanogr Res Pap* 53:1483–1516.

Haidvogel, D.B., Arango, H.G., Hedstrom, K., Beckmann, A., Malanotte-Rizzoli, P., Shchepetkin, A.F., 2000. Model Evaluation Experiments in the North Atlantic Basin: Simulations in Nonlinear Terrain-Following Coordinates. *Dynamics of Atmospheres and Oceans* 32, 239-281.

Haines, K. and Wu, P., 1995. A modelling study of the thermohaline circulation of the Mediterranean Sea: water formation and dispersal, *Oceanologica Acta*, 18(4), 401–417.

Herbaut, C., Martel, F., and Crépon, M., 1997. A sensitivity study of the General Circulation of the Western Mediterranean Sea. Part II: The Response to Atmospheric Forcing, *J. Phys. Oceanogr.*, 26, 65–84.

Herbaut, C., Mortier, L., and Crépon, M., 1996. A sensitivity study of the General Circulation of the Western Mediterranean Sea. Part I: The Response to Density Forcing through the Straits, *J. Phys. Oceanogr.*, 26, 65–84.

Jenkins, W., 1988. Nitrate flux into the euphotic zone near Bermuda. *Nature*. 331, 521–523.

Jones, H., and J. Marshall, 1993. Convection with rotation in a neutral ocean: A study of open-ocean deep convection. *J. Phys. Oceanogr.*, 23, 1009–1039.

Kantha, L.H., Clayson, C.A., 2000. Numerical Models of Oceans and Oceanic Processes. In: *International Geophysics Series*, vol. 66. Academic Press, San Diego. 940 pp.

Kone, V., Machu, E., Penven, P., Andersen, V., Garçon, V., Freon, P., Demarcq, H., 2005. Modeling the primary and secondary productions of the southern Benguela upwelling system: A comparative study through two biogeochemical models. *Global Biogeochemical Cycles*, 19.

Koszalka, I., Bracco, A., McWilliams, J.C., and Provenzale, A., 2009. Dynamics of wind-forced coherent anticyclones in the open ocean. *J. Geophys. Res.* 114, C08011, doi:10.1029/2009JC005388

Krahmann, G., Schott, F., Send, U., 2000. Seasonal heat content changes in the western Mediterranean Sea as a means for evaluating surface heat flux formulations. *J. Geophys. Res.* 105 (C7), 16941–16950.

Large, W.G., McWilliams, J.C., Doney, S.C., 1994. A review and model with a nonlocal boundary layer parameterization. *Rev. Geophys.* 32, 363–403.

Lascazatos, A., Roether, W., Nittis, K. & Klein, B., 1999. Recent changes in deep water formation and spreading in the eastern Mediterranean Sea. *Prog. Oceanogr.* 44, 5–36.

Lascazatos, A., Williams, R., & Tragou, E., 1993. A mixed layer study of the formation of Levantine intermediate water. *Journal of Geophysical Research*, 98, 739–749.

Le Fouest, V., Zakardjian, B., Saucier, F.J., Starr, M., 2005. Seasonal versus synoptic variability in planktonic production in a high-latitude marginal sea: the Gulf of St. Lawrence (Canada). *J. Geophys. Res. Oceans* 110, C09012.

Lévy, M., Mémery, L., André, J.-M., 1998a. Simulation of primary production and export fluxes in the Northwestern Mediterranean Sea. *J. Mar. Res.* 56, 197–238.

Lévy, M., Klein, P., 2004. Does the low frequency variability of mesoscale dynamics explain a part of the phytoplankton and zooplankton spectral variability? *Proc. R. Soc. London. Ser. A.* 460, 1673–1687.

MacCready, P. M., R. D. Hetland, W. R. Geyer. 2002. Long-Term Isohaline Salt Balance in an Estuary. *Continental Shelf Research*, 22, 1591-1601.

Madec G., Delecluse, P., Imbard, M., Levy, C., 1998. OPA8.1 Ocean general Circulation Model reference manual. Note du Pole de modelisazion, Institut Pierre-Simon Laplace (IPSL), France, 11.

Malanotte-Rizzoli, P., & Hecht, A., 1988. Large scale properties of the Eastern Mediterranean: a review. *Oceanologica Acta*, 11, 323–335.

Marchesiello, P., McWilliams, J.C., Shchepetkin, A., 2001. Open boundary condition for long-term integration of regional oceanic models. *Ocean Modelling* 3,1-21.

Marchesiello, P., McWilliams, J.C., Shchepetkin, A., 2003. Equilibrium structure and dynamics of the California Current System. *Journal of Physical Oceanography* 33, 753-783.

Margaleff, R., 1985. Environmental control of the mesoscale distribution of primary producers and its bearing to primary production in the western Mediterranean Sea. In: Moraitou-Apostolopoulou, M., Kiortsis, V. (Eds.), *Mediterranean marine ecosystems*. Plenum Press, New York, pp. 213–229.

Marshall, J., A. Adcroft, C. Hill, L. Perelman, and C. Heisey, 1997b. A finite-volume, incompressible Navier–Stokes model for studies of the ocean on parallel computers. *J. Geophys. Res.*, 102 (C3), 5753–5766.

Marshall, J., C. Hill, L. Perelman, and A. Adcroft, 1997a. Hydrostatic, quasi-hydrostatic and non-hydrostatic ocean modelling. *J. Geophys. Res.*, 102 (C3), 5733–5752.

Martin, A.P., Richards, K.J., Bracco, A., Provenzale, A., 2002. Patchy productivity in the open ocean. *Global Biogeochemical Cycles*. 16, 1025.

Marty, J.-C., Chiave' rini, J., Pizay, M.-D., Avril, B., 2002. Seasonal and interannual dynamics of nutrients and phytoplankton pigments in the western Mediterranean Sea at the DYFAMED time-series station (1991–1999). *Deep-Sea Research II* 49, 1965–1985.

Marty, J.C., 2000. DYFAMED Observation Service. [http://www.obs-
vlfr.fr/jgofs2/sodyf/home.htm](http://www.obs-vlfr.fr/jgofs2/sodyf/home.htm).

Marullo, S., Salusti, E., Viola, A., 1985. Observations of a small-scale baroclinic eddy in the Ligurian Sea. *Deep Sea Research. Part A*. 32, 215-222.

McGillicuddy, D. J., Robinson, A., 1997. Eddy-induced nutrient supply and new production in the Sargasso Sea, *Deep Sea Res. Part I*. 44, 1427– 1450.

MEDOCC 2006 Cruise Report 8th June 2006 – 3rd July 2006 ISMAR-CNR La Spezia.

Mellor, G. L. and T. Yamada, 1982. Development of a turbulence closure models for geophysical fluid problems. *Rev. Geophys. Space Phys.*, 20,851-875.

- Millot, C., 1991. Mesoscale and seasonal variabilities of the circulation in the Western Mediterranean. *Dyn. Atm. Oceans*. 15, 179–214.
- Millot, C., 1999. Circulation in the Western Mediterranean sea. *Journal of Marine Systems* 20 (14), 423-442.
- Millot, C. and Taupier-Letage, I., 2005a. Circulation in the Mediterranean Sea. The handbook of environmental chemistry, Vol. K (The Natural Environment and the Biological Cycles), Springer-Verlag Editor, 29–66.
- Miquel, J.C., Fowler, S.W., La Rosa, J., Buat-Ménard, P., 1994. Dynamics of the downward flux of particles and carbon in the open NW Mediterranean Sea. *Deep-Sea Research Part I* 41, 242–261.
- Molcard, A., Pinardi, N., Iskandarani, M., and Haidvogel, D. B., 2002. Wind driven general circulation of the Mediterranean Sea simulated with a Spectral Element Ocean Model, *Dyn. Atmos. Oceans*, 35, 97–130.
- Morel, A. 1988. Optical modelling of the upper ocean in relation to its biogenous matter content (case I waters), *J. Geophys. Res.*, 93, 10,749-10,768.
- Migon, C., Sandroni, V., 1999. Phosphorus in rainwater: partitioning, inputs and impact on the surface coastal ocean. *Limnology and Oceanography* 44, 1160–1165.
- Minas, H., Minas, M., Coste, B., Gostan, J., Nival, P., Bonin, M.C., 1988. Production de base et de recyclage; une revue de la problématique en méditerranée. *Oceanologica Acta* 9, 155–162.
- Morel, A. and J.-M. André. 1991. Pigment distribution and primary production in the western Mediterranean, as derived and modeled from coastal zone color scanner observations. *J. Geophys. Res.*, 96, 12685–12698.
- Morel, A. and Berthon. 1989. Surface pigments, algal biomass profiles, and potential production of the euphotic layer: Relationship reinvestigated in view of remote-sensing applications. *Oceanogr.*, 34, 1545-1562.
- Mounier, F., Echevin, V., Mortier, L., Crepon, M., 2005. Analysis of the mesoscale circulation in the occidental Mediterranean Sea during winter 1999-2000 given by a regional circulation model. 66, 251-269.

Murray, A. G. and J. S. Parslow, 1999. the analysis of alternative formulations in a simple model of a coastal ecosystem. *Ecol. Modelling*, 119, 149-166.

Ohman, M. D. and H. J. Hirche, 2001. Density-dependent mortality in an oceanic copepod population. *Nature*, 412, 638-641.

Ovchinnikov, I. M., 1984. The formation of Intermediate Water in the Mediterranean. *Oceanology*, 24, 168–173.

Owens, N.J.P., Rees, A.P., Woodward, E.M.S., Mantoura, R.F.C., 1989. Size-fractionated primary production and nitrogen assimilation in the northwest Mediterranean Sea during January 1989. *Water Pollution Research Bulletin* 13, 126–135.

Pasquero, C., Provenzale, A., Babiano, A., 2001. Parameterization of dispersion in two-dimensional turbulence. *J. Fluid Mechanics*. 439, 279-303.

Pasquero, C., Bracco, A., Provenzale, A., 2005. Impact of the spatiotemporal variability of the nutrient flux on primary productivity in the ocean. *J. Geophysical Research*. 110, C07005.

Penven P. 2003. ROMSTOOLS user's guide. Available at www.brest.ird.fr/Roms_tools.

Penven, P., Roy C., Lutjeharms, J.R.E., Colin de Verdière, A., Johnson, A., Shillington, F., Fréon, P., Brundrit, G., 2001. A regional hydrodynamic model of the Southern Benguela. *South African Journal of Science* 97, 472-476.

Penven P, Debreu L, Marchesiello P, McWilliams JC, 2006a. Evaluation and application of the ROMS 1-way embedding procedure to the central California upwelling system. *Ocean Model* 12:157–187

Pinardi, N. and Masetti, E., 2000. Variability of the large-scale general circulation of the Mediterranean Sea from observations and modelling: a review, *Palaeogeography, Palaeoclimatology, Palaeoecology*, 158, 153–173.

Pinardi, N. and Navarra, A., 1993. Baroclinic wind adjustment processes in the Mediterranean Sea, *Deep-Sea Res.*, 40, 1299–1326.

Pinardi, N., Allen, J. I., Demirov, E., De Mey, P., Korres, G., Lascaratos, A., Le Traon, P. Y., Maillard, C., Manzella, G., and Tziavos, C., 2003. The

Mediterranean ocean Forecasting System: First phase of implementation (1998–2001), *Ann. Geophysicae*, this issue.

Provenzale, A., 1999. Transport by coherent barotropic vortices. *Annual Rev. Fluid Mech.* 31, 55-93

Raick, C., Delhez, E.J.M., Soetaert, K., Grégoire, M., 2005. Study of the seasonal cycle of the biogeochemical processes in the Ligurian Sea using a 1D interdisciplinary model. *Journal of Marine Systems* 55, 177–203.

Raimbault, P., Coste, B., 1990. Very high values of the nitratephosphate ratio (>30) in the subsurface layers of the western Mediterranean Sea. *Rapp. P.V., Réunion Comm. Internationale Mer Méditerranée* 32, 18.

Robinson, A., Leslie, W.G., Theocharis, A., Lascaratos, A., 2001. *Mediterranean Sea Circulation*. Encyclopedia of Ocean Sciences. Academic Press.

Roussenov, V., Stanev, E., Artale, V., and Pinardi, N., 1995. A seasonal model of the Mediterranean Sea general circulation, *J. Geophys. Res.*, 100, 13 515–13 538.

Sammari, C., Millot, C., & Prieur, L., 1995. Aspects of the seasonal and mesoscale variabilities of the Northern Current in the Western Mediterranean Sea inferred from the prolig-2 and pros-6 experiments. *Deep-Sea Research I*, 42(6), 893–917.

Santoleri, R., Salusti, E., Stocchino, C., 1983. Hydrological currents in the Ligurian Sea. *Il Nuovo Cimento C.* 6, 353-370.

Sarmiento, J.L., Slater, R.D., Fasham, M.J.R., Ducklow, H.W., Toggweiler, J.R., Evans, G.T., 1993. A seasonal three-dimensional ecosystem model of nitrogen cycling in the North Atlantic euphotic zone. *Global Biogeochemical Cycles* 7, 417–450.

Shchepetkin, A.F., McWilliams, J.C., 2003. A method for computing horizontal pressure-gradient force in an oceanic model with a non-aligned vertical coordinate. *J. Geophys. Res.* 108 (C3), 3090.

Shchepetkin, A.F., McWilliams, J.C., 2005. Regional Ocean Model System: a split-explicit ocean model with a free-surface and topography-following vertical coordinate. *Ocean Modelling* 9, 347- 404.

Shchepetkin, A.F., McWilliams, J.C., 2008. Computational kernel algorithms for fine- 1056 scale, multi-process, long-term oceanic simulations. In: Teman, R., Tribbia, J. 1057 (Eds.), Handbook of Numerical analysis on Computational Methods for the 1058 Oceans and Atmosphere, pp. 56–79.

Smith, W.H.F., Sandwell, D.T., 1997. Global seafloor topography from satellite altimetry and ship depth soundings. *Science*. 277, 1957-1962.

Song, Y.T., Haidvogel, D., 1994. A semi-implicit ocean circulation model using a generalized topography following coordinate system. *J. Comp. Phys.* 115, 228–248.

Sparnocchia, S., P. Picco, G.M.R. Manzella, A. Ribotti, S. Copello and P. Brasey., 1995. Intermediate water formation in the Ligurian sea. *Oceanol. Acta*, 18: 151-162.

Steppler, J., Doms, G., Schättler, U., Bitzer, H. W., Gassmann, A., Damrath, U., Gregoric, G., 2003. Mesogamma scale forecast using the nonhydrostatic model LM. *Meteor. Atmos. Phys.* 82, 75-96.

Styles R., S.M. Glenn, 2002. Modeling bottom roughness in the presence of wave-generated ripples, *Journal of Geophysical Research* 107 C8.

Tanaka T, Rassoulzadegan F., 2002. Full-depth profile (0–2000 m) of bacteria, heterotrophic nanoflagellates and ciliates in the NW Mediterranean Sea: vertical partitioning of microbial trophic structures. *Deep-Sea Res II* 49:2093–2107.

Tian, R.C., 2006. Toward standard parameterizations in marine biological modeling. *Ecol. Model.* 193, 363-386.

Turley CM., 1999. The changing Mediterranean Sea – a sensitive ecosystem? *Prog Oceanogr* 44:387–400.

Tziperman, E. and Malanotte-Rizzoli, P., 1991. The climatological seasonal circulation of the Mediterranean Sea, *J. Mar. Res.*, 49, 411–434.

Umlauf, L., Burchard, H., 2003. A generic length-scale equation for geophysical turbulence models. *J. Marine Res.* 61, 235–265.

Vichi, M., Oddo, P., Zavatarelli, M., Coluccelli, A., Coppini, G., Celio, M., Umani, S. F., and Pinardi, N., 2003b. Calibration and validation of a one-

dimensional complex marine biogeochemical fluxes model in different areas of the northern Adriatic shelf, *Ann. Geophys.*, 21, 413–436.

Warner JC, Sherwood CR, Arango HG, Signell RP, 2005. Performance of four turbulence closure models implemented using a generic length scalar method. *Ocean Model* 8:81–113.

Weiss, J., 1991. The dynamics of enstrophy transfer in two-dimensional hydrodynamics. *Physica D.* 48, 273-294.

White AA, Bromley, RA, 1995. Dynamically consistent, quasihydrostatic equations for global models with a complete representation of the Coriolis force. *Q J R Meteorol Soc* 121:399-418.

Wust, G., 1961. On the vertical circulation of the Mediterranean Sea. *J. Geophys. Res.* 66, 3261–3271.

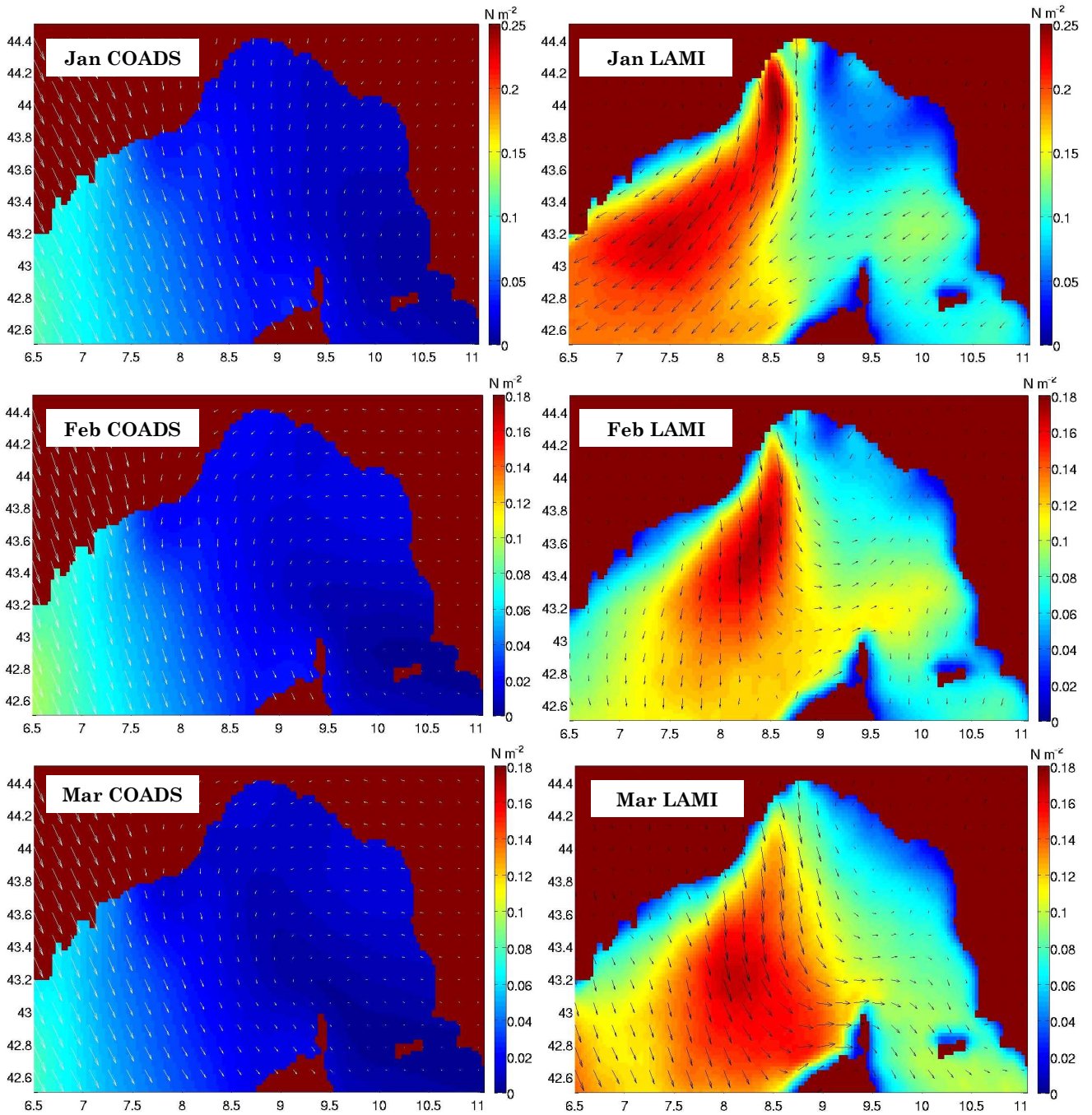
Zakardjian, B., and Prieur, L., 1998. Biological and chemical signs of upward motions in permanent geostrophic fronts of the Western Mediterranean. *J. Geophys. Res.* 103, 27,849–27,866.

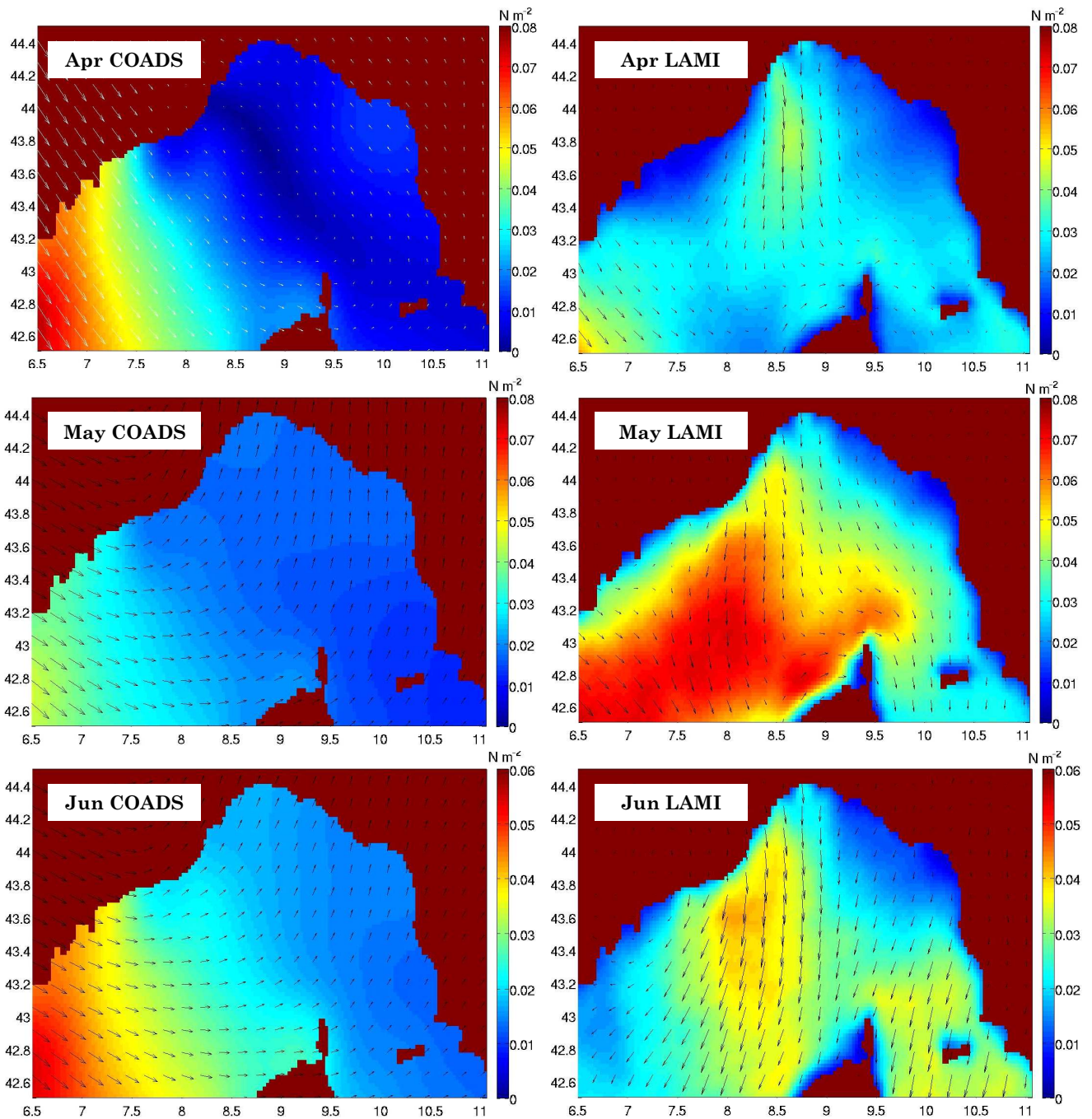
Zavala Sanson, L., Provenzale, A., 2009. The effects of abrupt topography on plankton dynamics. *Theoretical Population Biology*, in press.

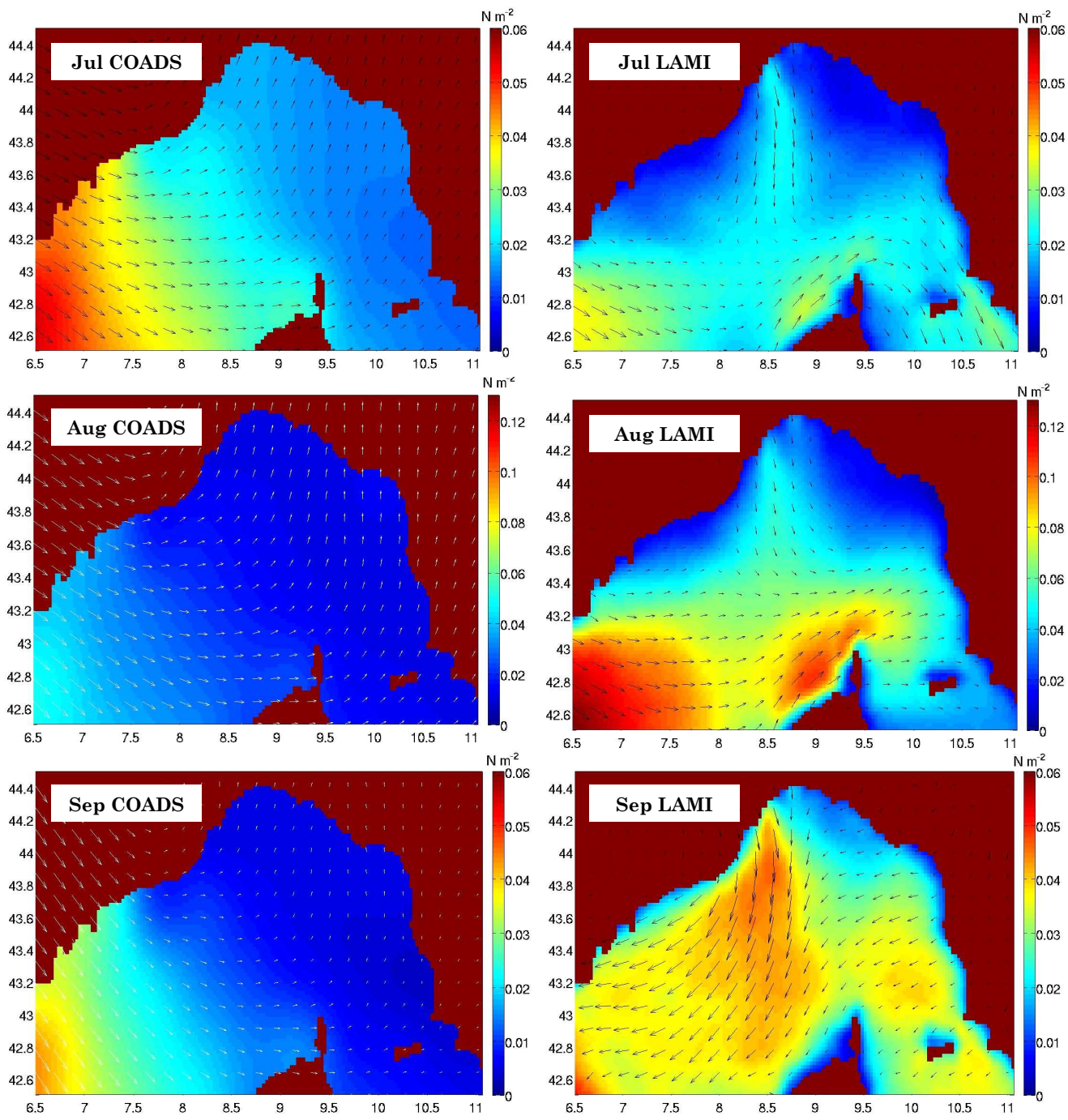
Zavatarelli, M. and Mellor, G., 1995. A numerical study of the Mediterranean Sea Circulation, *J. Phys. Oceanogr.*, 25, 1384–1414.

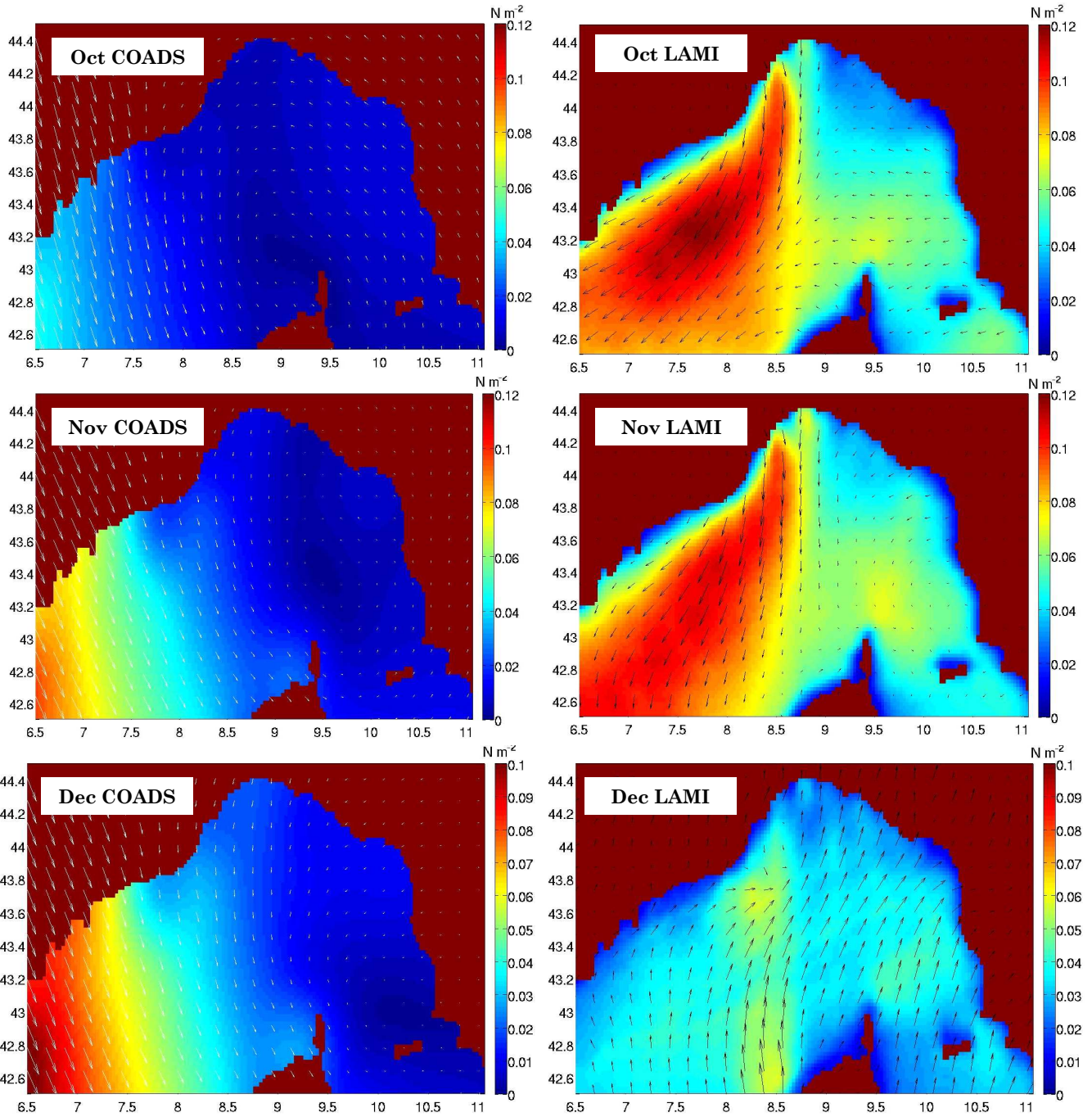
ANNEX 1

Comparison between the wind stress intensity and direction from COADS and COSMO-I7(LAMI) datasets interpolated on the ROMS grid.



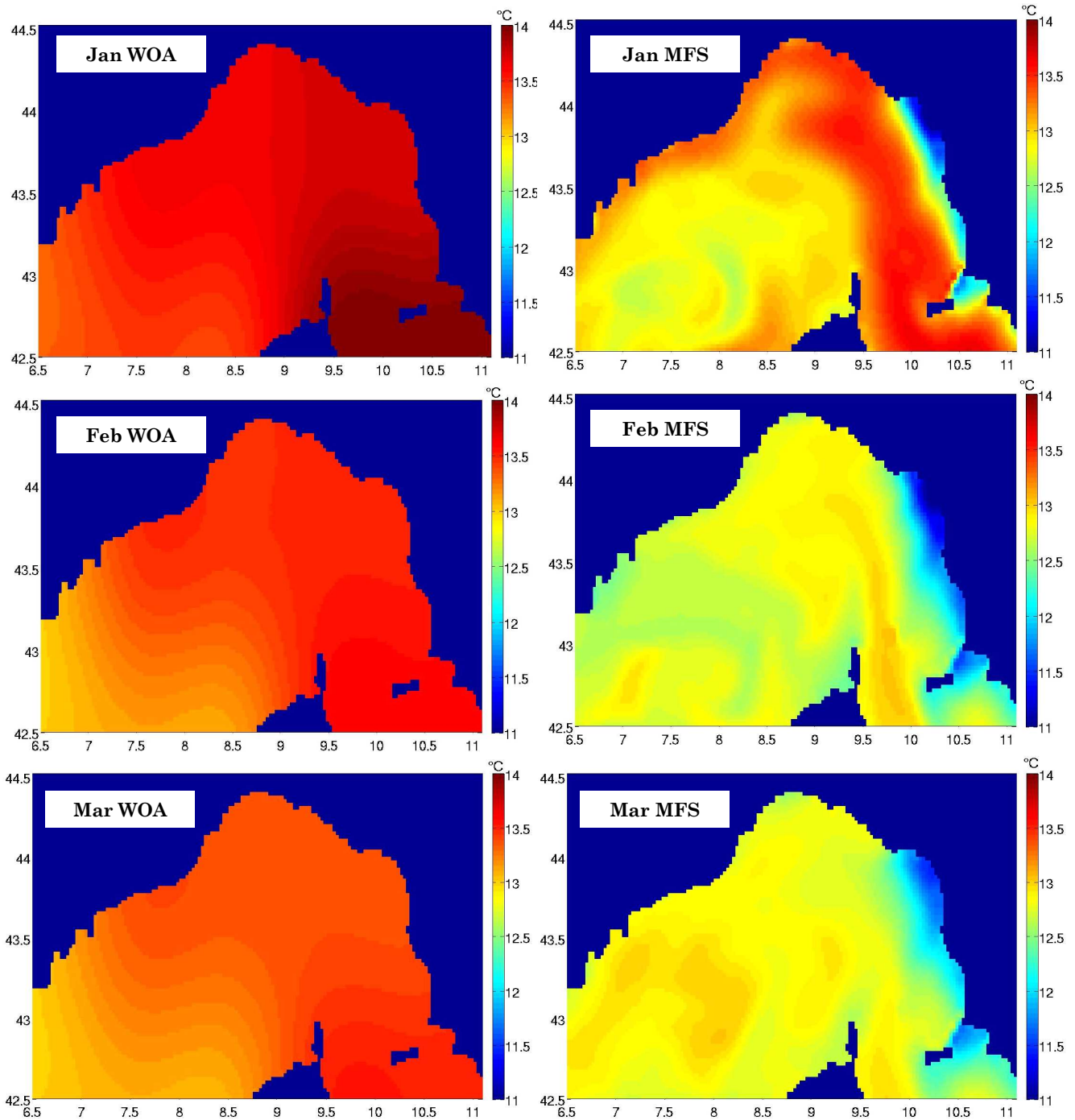


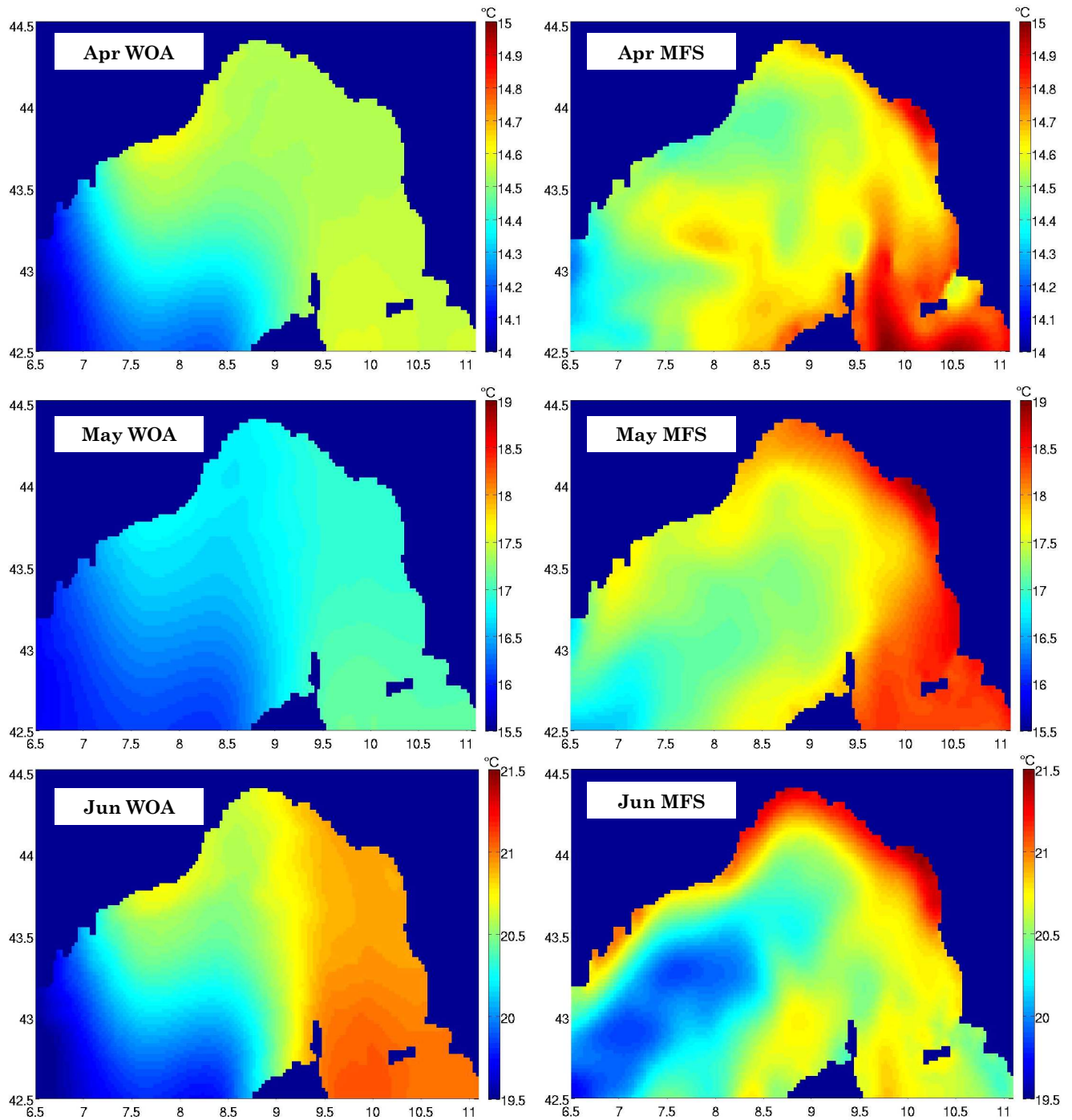


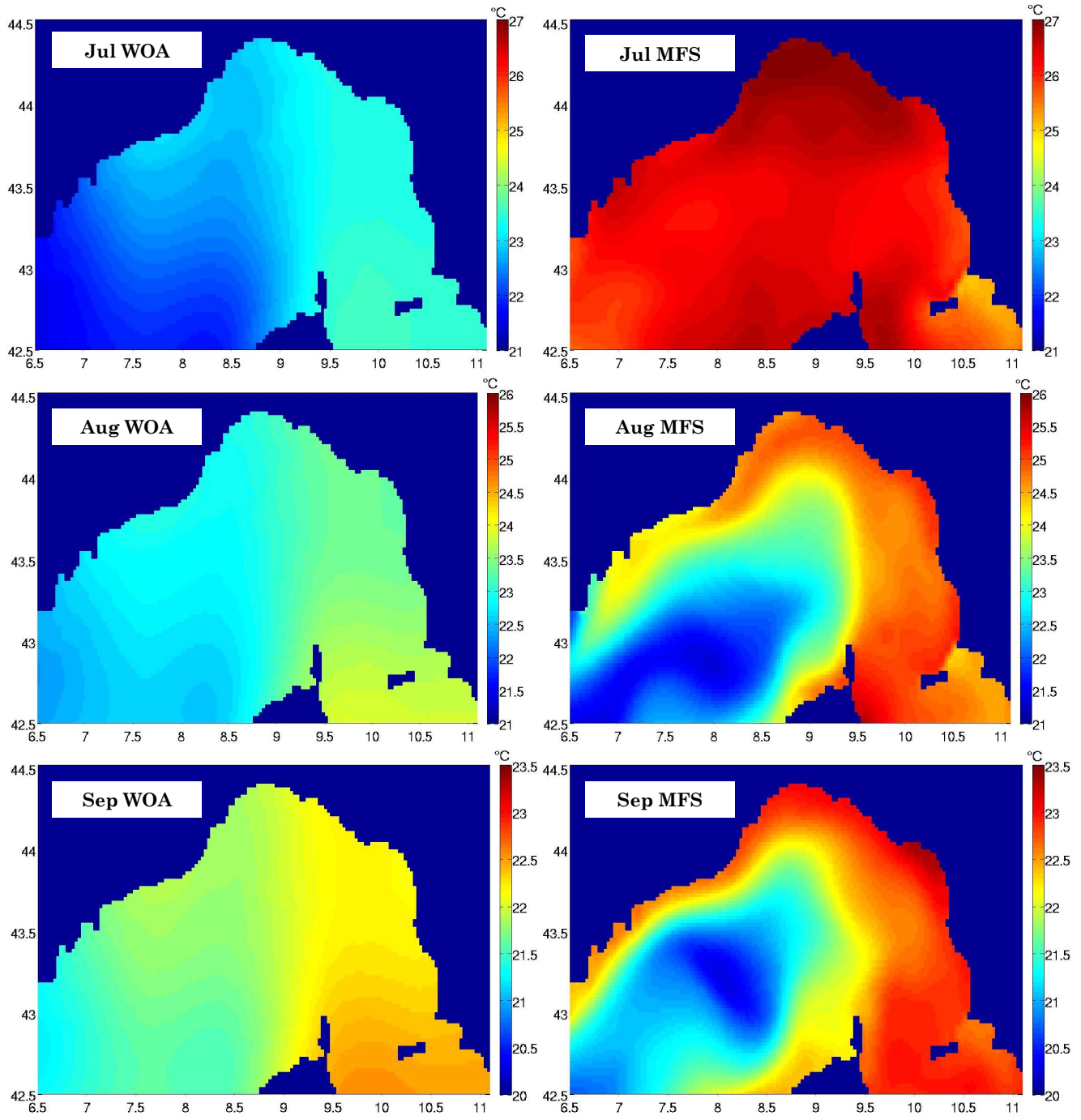


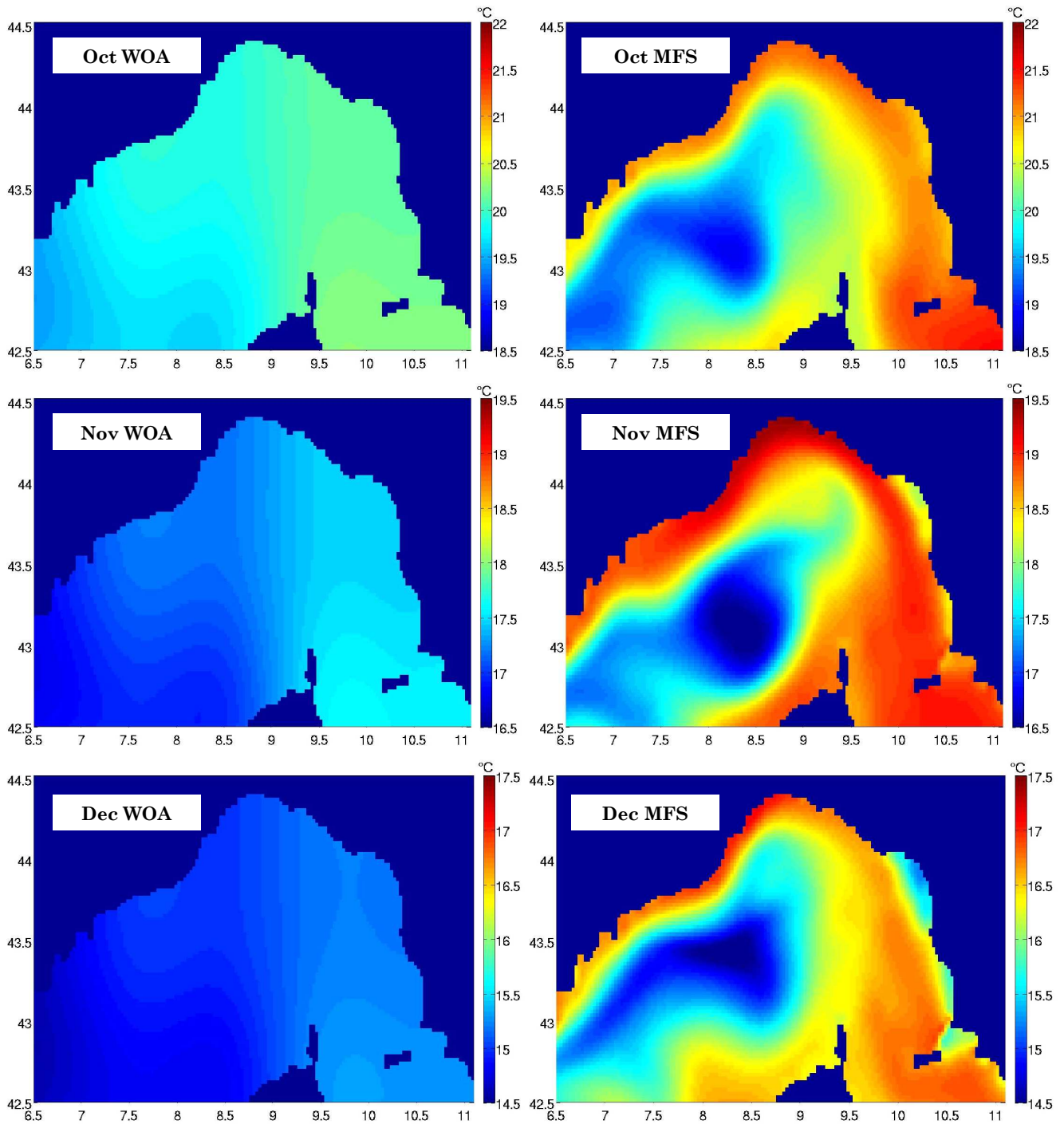
ANNEX 2

Comparison between surface temperature field from WOA and MFS datasets interpolated on the ROMS grid.









Acknowledgments

I would like to acknowledge my supervisors Anne Molcard (LSEET-University of Toulon), Antonello Provenzale (ISAC-CNR, Torino) and Luca Ferraris (DIST-University of Genova) for their help, trust, encouragement and support during the realisation of this work, and for accepting the co-direction of the PhD thesis between the two Universities (University of Basilicata and University of Toulon).

I'm deeply grateful to Bruno Zakardjian (LSEET-University of Toulon) for his help, comments, patience, time, reading and re-reading, and jet again re-reading.

I would also like to thank the LSEET laboratory staff for hosting me several months during the realisation of the thesis.

I would like to thank the CIMA laboratory staff for the help during the realisation of the thesis.

I wish to thank Sabrina Speich (LPO-University of Brest) and Enrico Zambianchi (DISAM-University of Napoli) for their advices and for the critical revision of the final draft of the thesis.

Anna Vetrano (ISMAR-CNR Spezia) and Annalisa Griffa (ISMAR-CNR Spezia) provided data for the model evaluation: I wish to thank them for the collaboration and help.

I wish to thank Luis Zavala Sanson (CICESE Ensenada, Messico) for his advices and help in the first part of the thesis.

I would like to express my gratitude to Franco Siccardi (CIMA Research Foundation) for his advice, support and interest in my thesis.

I would like to thank my colleagues Paola, Massimiliano and Aurelie for help, comments and scientific discussion during the elaboration of this thesis. Moreover I wish to thank my colleagues Federica, Elisabetta and Giorgia for the support during difficulties and for their friendship.

I want to thank my parents for their support and encouragement during the last years and Laura and Marco for their lightheartedness. This thank is extensive to Alessio for his love, understanding, scientific support and motivation.

Curriculum vitae

Born: Finale Ligure, SV, Italy, 22 Jan 1981

Nationality: Italian

Ph.D.

“Methods and Technologies for Environmental Monitoring” University of Basilicata (Italy) in “Co-tutelle” with the University of Toulon (France) at CIMA (Research Foundation, International Centre of Environmental Monitoring), Savona, Italy.

Thesis: Numerical simulation of mesoscale processes in the Ligurian Sea.

Tutors: Luca Ferraris (University of Genoa), Anne Molcard (University of Toulon).

Supervisors: Antonello Provenzale (ISAC-CNR Torino), Anne Molcard (University of Toulon).

University of Genova.

Graduate Studies (Degree) Environmental Engineering; Management of natural and industrial hazard.

Degree theses: A process-oriented numerical model (POM, Princeton Ocean Model) of the Ligurian Sea. Prof. Antonello Provenzale, Prof. Anne Molcard.

Grade: 110 out of 110 cum laude. Degree thesis on 29 Sept 2006.

ERASMUS project at University of Montpellier II “Ecole Polytechnique Universitaire” department “Science et Technologies de l’Eau ” France. Feb – Jun 2004.

Bachelor of Science in Environmental Engineering.

Grade: 110 out of 110 cum laude. Degree thesis on 29 Nov 2004.

Ph.D. activities:

Publications

Casella E., Molcard A., Provenzale A. Mesoscale vortices in the Ligurian Sea and their effect on coastal upwelling processes. Submitted to Journal of Marine Systems.

Meetings

Casella E., Molcard A., Zakardjian B., Provenzale A. Simulation of mesoscale processes in the Ligurian Sea. Geoitalia: GEOITALIA 2009 VII Forum Italiano di Scienze della Terra. Rimini, 9-11 September 2009 (Oral).

Casella E., Molcard A., Provenzale A. Mesoscale vortices in the Ligurian Sea and their effect on coastal upwelling processes. 41st International Liège Colloquium on Ocean Dynamics Science-based management of the coastal waters. 4-8 May 2009 (Oral).

Teaching activity

Assistant lecturer. Course: “Elementi di Oceanografia”. Environmental Engineering, University of Genoa. March 2009;

Assistant lecturer. Course: “Elementi di Oceanografia”. Environmental Engineering, University of Genoa. March 2008.

Operative activity

Operative activity at the Operational Room of the CIMA Research Foundation. The aim of the operational room is to provide technical support to civil protection decision-makers in order to issue meteo-hydrological and wild fire risk warnings, through a conform surveillance.

Academics (summer schools and courses)

Summer School: Modern methods for ecosystem modelling. Scottish Association for Marine Science (SAMS), Oban, Scotland. 29 June 11 July 2008.

Summer School: “Ecole professionnalisant Innov@Doc Collège des études doctorales”, Frejus, France. 20-24 November 2007

Alpine Summer School: Atmosphere-Ocean Convection in Climate Dynamics. Aosta, Italy. 23-28 June 2007

Course: “Meteorologia Operativa” prof. Barbara Turato. University of Genoa. May 2008.

Course: “Traitement de données géophysiques”, prof. Anne Molcard. University of Toulon. November, December 2007.

Course: “Dinamica degli ecosistemi”, prof. Jost von Hardenberg. University of Genoa. March, April, May 2007.

Course: “Elementi di Oceanografia”, prof. Antonello Provenzale. University of Genoa. March, April, May 2007.